Heat Exchange in a Conifer Canopy

A Deep Look using Fiber Optic Sensors

Schilperoort, B.

DOI
10.4233/uuid:6d18abba-a418-4870-ab19-c195364b654b

Publication date
2022

Document Version
Final published version

Citation (APA)
Schilperoort, B. (2022). *Heat Exchange in a Conifer Canopy: A Deep Look using Fiber Optic Sensors*. [Dissertation (TU Delft), Delft University of Technology]. https://doi.org/10.4233/uuid:6d18abba-a418-4870-ab19-c195364b654b

Heat Exchange in a Conifer Canopy

A Deep Look using Fiber Optic Sensors

Heat Exchange in a Conifer Canopy

A Deep Look using Fiber Optic Sensors

Proefschrift

ter verkrijging van de graad van doctor
aan de Technische Universiteit Delft,
op gezag van de Rector Magnificus Prof.dr.ir. T.H.J.J. van der Hagen,
voorzitter van het College voor Promoties,
in het openbaar te verdedigen
op woensdag 13 april 2022 om 15.00 uur

door

Bart SCHILPEROORT

Ingenieur in Civiele Techniek, Technische Universiteit Delft, Nederland,
geboren te Leidschendam, Nederland

Dit proefschrift is goedgekeurd door de

promotor: Prof.dr.ir. H.H.G. Savenije,
copromotor: Dr.ir. A.M.J. Coenders-Gerrits

Samenstelling promotiecommissie:

Rector Magnificus,	voorzitter
Prof.dr.ir. H.H.G. Savenije,	Technische Universiteit Delft, promotor
Dr.ir. A.M.J. Coenders-Gerrits,	Technische Universiteit Delft, copromotor
Onafhankelijke leden:	
Prof. dr. ir. N.C. van de Giesen	Technische Universiteit Delft
Prof. dr. J. Vilà-Guerau de Arellano	Wageningen University & Research
Prof. dr. J.S. Selker	Oregon State University
Prof. dr. S.W. Tyler	University of Reno, Nevada
Prof. dr. ir. R. Uijlenhoet	Technische Universiteit Delft, reservelid
Overig lid:	
Prof. dr. ir. B.J.H. van de Wiel,	Technische Universiteit Delft

NWO
Nederlandse Organisatie voor Wetenschappelijk Onderzoek

Keywords:	distributed temperature sensing, evaporation, forest, heat flux, boundary layer, temperature inversion, soil temperature
Printed by:	Ipskamp Printing
Style:	TU Delft House Style, with modifications by Moritz Beller `https://github.com/Inventitech/phd-thesis-template`

The author set this thesis in LaTeX using the Libertinus and Inconsolata fonts.

ISBN …

An electronic version of this dissertation is available at `http://repository.tudelft.nl/`.

No one ever measures the same forest twice, for it is not the same forest
and they are not the same person

adapted from Heraclitus

Contents

Summary

Forests cover a large part of the globe, and are responsible for a large amount of evaporation and the fixation of carbon. To be able to better understand this atmospheric exchange of forests, and how the forests will behave under future climate change, both accurate measurements as well as models are required. However, due to their height and heterogeneity they are difficult to model and measure. Standard theories do not apply well to forests, and as such more effort is required to understand the exchange between the forests and the atmosphere. However, precise measurements are made difficult due to a number of issues. The most prominent are the non-closure of the energy balance, and so-called 'decoupling' of the canopy. Non-closure of the energy balance is where all the measured inflows and outflows of energy do not add up to the measured change in energy storage in the forest system. The size and heterogeneity of forests makes this difficult to assess. Second is 'decoupling', where the vertical mixing of air within the canopy is hampered, and measurements performed above the canopy are not representative of what happens in the entire canopy down to the forest floor.

In this thesis these issues are studied using 'Distributed Temperature Sensing' (DTS), where the temperature of a fiber optic cable is measured along its entire length, like a long string of thermometers. The temperature of the fiber optic cable can be measured multiple times per meter, for cables up to thousands of meters long. This allows measurements of temperature and other variables at a resolution and scale which was previously not feasible. This thesis revolves around studying the heat exchange in a coniferous forest, with the aim to validate temperature and humidity profiles as measured with DTS, and to then use these profiles to estimate evaporation of the forest and heat storage within the canopy. Next the aim is to use the temperature profiles to characterize decoupling at the measurement site and to study this at a higher detail than previously possible. The last goal is to use DTS to get a higher resolution view on the soil temperature and thermal properties.

At the Cabauw Experimental Site for Atmospheric Research of the KNMI (Royal Netherlands Meteorological Institute) the temperature profiles as measured by the DTS were validated against highly accurate air temperature sensors. This showed that both solar radiation during the day and radiative cooling at night can cause large errors in the air temperature estimation: up to 1.0 K. However, under the conditions within the studied forest canopy the errors are generally within acceptable bounds for the processes studied in this thesis.

The measurements in a coniferous forest were performed at the 'Speulderbos' measurement site on the heavily forested 'Veluwe' ridge of hills in Gelderland, the Netherlands. The trees have a height of around 34 m, and a 48 m tall measurement tower is present at the site. Fiber optic cables were placed vertically along the tower. The cables measured the air temperature, and, by wetting them, the humidity. Using these profiles of temperature and humidity, it was determined that the energy storage in the air column of the forest represents a very significant part (20 – 40%) of the net radiation at a sub-hourly timescale.

The profiles of air temperature and humidity also allowed the calculation of the Bowen ratio above the canopy, and thus the evaporation rate. The evaporation rate determined with the DTS-Bowen ratio corresponds well to the standard Eddy Covariance method. Besides the energy storage and fluxes, the air temperature profiles also allow studying decoupling at the Speulderbos site over multiple seasons. The air in the lower understory was nearly always colder, and thus denser, than the air above the forest, which suppresses turbulent mixing. While some convection occurred near the forest floor, the understory of the forest was very regularly (~50% of the time) decoupled from the air above.

The decoupling is further studied with thinner fiber optic cables, which allow measuring the air temperature at a much finer timescale due to its low thermal inertia. These measurements show that a sharp inversion layer was present in the forest very regularly. The inversion was highly dynamic; moving with amplitudes up to 10 m, at timescales of 50 – 100 seconds. Due to these motions and the height of the canopy, this inversion can only be detected using a very dense network of fast response temperature sensors. Thus, these inversions could be very common at other sites but generally elude detection.

To improve the measurement of soil temperature, a DTS-based temperature probe was designed and manufactured. The probe was able to measure the soil temperature at a very high vertical resolution, which aids in estimation soil thermal properties, and can thus improve measurements of heat storage in the soil.

The results demonstrate that with DTS it is possible to study the forest canopy in more detail. It enables quantification of the energy storage in the air column and soil at a higher resolution, and can be used to characterize decoupling at a measurement site. However, the measurements often lacked sufficient wind data. In future research DTS can be used to measure profiles of the wind speed by actively warming the fiber optic cables. While the vertical profiles of temperature provided a lot of useful information, more temperature data collected with horizontal profiles would be useful to describe the observed phenomena in more detail. With DTS slowly reaching maturity within geosciences, more standardization will make performing these types of measurements easier, and will allow to make full use of the possibilities.

1 Introduction

Nicolas Poussin - Paysage avec Orion aveugle cherchant le soleil (1658)

1

1.1 Background & Context

For millennia people have tried to explain and predict weather and the seasons. The term 'meteorology' itself was first coined by Aristotle, as the title of a text in which he describes weather phenomena such as evaporation, dew and frost. However, in its early days meteorology was limited to broad descriptions of phenomena, as accurate instrumentation beyond, e.g., manual rain gauges, was not available. It was not until the 18th century that Daniel Gabriel Fahrenheit developed the first reliable and *reproducible* thermometer in Amsterdam to measure temperature. Besides just temperature, this also allowed a more reliable determination of humidity, by making use of the wet bulb temperature. This was an improvement on earlier methods where the tension of hair was used to estimate humidity. The development of reliable and reproducible instrumentation allowed the accurate measurement of local weather. Stations measuring the weather were established all around to globe, by various scientific institutes and governmental bodies. The collection of this weather data generated a global dataset, and analysis of local and global trends in this data lead to the birth of climatology. With this came an understanding of the hydrological cycle, where evaporated water provides the vapor for the formation of clouds, which rain out and feed into the vegetation, soil, groundwater, and rivers, which flow down into lakes and the ocean. The importance of evaporation extends beyond just the hydrological cycle. It enables a huge transfer of heat from the earth's surface to the upper atmosphere, accounting for more energy than the other fluxes, namely sensible heat and (net) longwave radiation, combined (Trenberth et al., 2009; Loeb et al., 2009). In the form of transpiration by vegetation, evaporation plays a central role in the carbon cycle as well, as terrestrial plants need to transpire water to absorb carbon dioxide from the atmosphere.

Nowadays satellite observations and detailed numerical models cover the entire planet, measuring and modeling the weather, water cycle, and the carbon cycle at a global scale. However, these observations and models are limited. Satellites can only see so much, and require continuous ground truth data to ensure their accuracy. While climate models are able to forecast what will happen to the planet on a large scale over longer time periods (Hausfather et al., 2020), this is not the case for weather. Despite increasing computational power it is not possible to perfectly model the entire earth surface and atmosphere in detail, as small errors will rapidly amplify into huge differences (Lorenz, 1969). These limitations mean that assumptions and simplifications have to be made, and that the models and satellite observations have to be verified with local field-scale measurements. It is unfeasible to measure and model every leaf on every tree on the planet, and while every forest is unique, common features like tree height of canopy density can be extracted to describe and parameterize small scale, complex processes. This parameterization of small scale complex processes is reliant on detailed measurements.

Inaccuracies in satellite observations and global models can have serious consequences. A recent study found that satellite derived data is potentially severely underestimating either current global warming or the amount of water vapor in the lower atmosphere (Santer et al., 2021). For this reason sufficient and globally distributed ground-truth data is essential. While some parts of the world have observations of atmospheric fluxes such as evaporation and CO_2 going back decades, these observations are concentrated in North America, Europe, and Japan, covering just 5% of the total land surface area (Fluxnet, 2017). To make matters worse, the number of observation sites is decreasing, for a large part in

Europe, and nearly all observation sites in Africa are not maintained anymore. While this is a trend which is difficult to reverse, efforts can be made to understand current measurement sites better and in more detail. While this will never be a perfect replacement, improving our understanding of the current sites could make them more generally applicable.

Many processes such as water, heat, and CO_2 exchange between the land and atmosphere are quantified at scales around 100 m to 1 km (Burba et al., 2010). A lot of work has already been done in this field, especially concerning more 'simple' surfaces such as open water or short vegetation. However, forests remain an issue due to their large height, which complicates measuring their fluxes, and invalidates theories and approximations used for other land surfaces (Barr et al., 1994; Katul et al., 1995). While the interaction between forests and the atmosphere is less well understood, they cover a large part of the land surface, and are very important components of the water and carbon cycles. Some of the complications relate to the large storage space for heat and water vapor in the air column; with a 30 meter tall canopy the air volume itself takes a lot of energy to heat up, as compared to, for example, a 3 meter tall field of corn (Jiménez-Rodríguez et al., 2020b; Coenders-Gerrits et al., 2020). The distribution of branches and leaves can also differ a lot in forests, while many canopies are very open, with gaps letting in light and wind, others can have a very enclosed roof. An enclosed canopy will prevent sunlight and wind from penetrating through the canopy and reaching the forest floor, reducing the vertical mixing, and restricting the water vapor and heat fluxes to the canopy top (Jiménez-Rodríguez et al., 2020c).

1.1.1 Measuring atmospheric fluxes over forests

To quantify the amount of water that forests are evaporating, and to study the CO_2 exchange between forests and the atmosphere, measurement sites use a set of equipment. Most commonly, the main atmospheric fluxes are determined using the 'eddy covariance' technique (Burba et al., 2010), where both the wind speed and concentrations of, e.g., water vapor and CO_2 in the air are measured at high frequency (Aubinet et al., 2012b; Burba, 2013). As turbulent eddies are transporting water vapor upwards, the concentration of water in upgoing air will be slightly higher than downgoing air. By studying the covariance between the concentration and vertical wind speed, the flux can be determined. This is generally applied to fluxes of heat, water vapor and CO_2. To get a representative measurement, the measurements have to be made sufficiently high above the treetops, on top of a (usually) metal frame tower. Therefore, sites where the atmospheric fluxes are measured are often referred to as 'flux towers'. As the sensors measure parameters in the moving air, the information comes from an upwind area; the 'flux footprint', and not directly from the forest below.

Often, other sensors are placed at the site to support the atmospheric flux measurements. These sensors measure parameters such as rainfall, incoming and outgoing radiation, traditional sensors measuring air temperature and humidity, and soil heat flux sensors. This equipment allows for verifying and improving the flux estimates, and to do more in-depth studies to, for example, study patterns in the evaporation or CO_2 fluxes.

However, the flux measurements are not perfect. First is the lack of closure in the energy balance. If measurements were perfect, it would be expected that the amount of energy stored in a system is in balance with the energy entering and leaving the system,

1

as energy cannot be created or destroyed. The energy balance of a forest canopy can be described with the following elements (Oliphant et al., 2004):

$$\frac{\mathrm{d}Q}{\mathrm{d}t} = R_N - H - \rho\lambda E - G_S + A \tag{1.1}$$

where the storage change over time ($\frac{\mathrm{d}Q}{\mathrm{d}t}$) should be equal to the sum of the inflows and outflows; the net radiation (R_N), sensible heat flux (H), latent heat flux ($\rho\lambda E$), photosynthesis (P), and any horizontally advected energy (A). The canopy storage term consists of (McCaughey and Saxton, 1988):

$$\frac{\mathrm{d}Q}{\mathrm{d}t} = \frac{\mathrm{d}Q_H}{\mathrm{d}t} + \frac{\mathrm{d}Q_E}{\mathrm{d}t} + \frac{\mathrm{d}Q_B}{\mathrm{d}t} + \frac{\mathrm{d}Q_P}{\mathrm{d}t} \tag{1.2}$$

where Q_H is the energy stored as heat in the air column, Q_E the energy stored in the air as vapor, Q_B the biomass heat storage, and Q_P the energy stored through photosynthesis.

Despite great effort, achieving energy balance closure still remains very difficult. The lack of closure, and the lack of certain knowledge where the closure issue is originating from makes it more difficult to asses the accuracy of the flux measurements. Most important to get correct is instrument accuracy. Not only is it required to verify the manufacturer's specifications, properly maintaining the sensors over longer time periods is also required, as just scratches, dirt, or even cobwebs can cause inaccuracies in some equipment (Culf et al., 2004). But even with properly working equipment, energy balance closure remains problematic. Due to sensors disturbing the soil, incorrect estimations of energy storage in the top layer of the soil can be part of the reason at sites with low vegetation (Foken, 2008). However, in forests with dense canopies the soil heat flux is quite minimal, but in that case, the heat storage in the entire air column becomes an issue that has to be correctly determined.

Another issue with flux measurements is the stability state of the atmosphere. For example, during the day the sun warms up the land surface, which in turn will warm up the air. When the air closer to the surface is warm, and the air higher up is cool, the density differences will cause natural convection where the ('lighter') warm air will rise and the ('heavier') cool air sinks down, as this stratification is 'unstable'. This convection will generate turbulence and strongly mix the atmosphere. At night, when the sky is clear, the land surface can cool down strongly, which in turn will cool down the air. However, this cold air will be more dense than the air above, and will work to reduce mixing in the atmosphere, as this stratification is 'stable'. The stability of the atmosphere can impact flux measurements in multiple ways. When the atmosphere is more stable, the flux footprint will be much larger than during unstable conditions, due to the reduced turbulent mixing. This causes the flux measurements to be less representative of the area of interest. Besides a larger footprint, the stable stratification can also cause part of the canopy to not be turbulently connected to the atmosphere anymore. The combination of the air density differences and the structure of the vegetation can reduce the turbulent mixing to a point where it is negligible. In this so-called 'decoupled' state, any water evaporated or CO_2 emitted by the soil or vegetation, will build up within the canopy, and either flow out of the forest laterally (not passing the sensors above), or be emitted in a concentrated plume which is likely to be missed by the instrumentation (Raupach et al., 1996; Finnigan, 2000).

This leads to a heterogeneity of fluxes, even in seemingly 'homogeneous' terrain, and the different scales at which each device measures complicates things even more.

Recent research has also shown that, when studying the net ecosystem exchange (NEE) of CO_2, measurements above the forest floor are essential (Jocher et al., 2017). Due to decoupling, measurements above the tree tops are not able to properly represent what goes on in the entire forest, leading to incorrect characterizations of the carbon storage or release by forests (Aubinet et al., 2012b; Alekseychik et al., 2013). Chi et al. (2021) showed that what happens on the forest floor determines the differences in CO_2 fluxes between (boreal) forests.

At the base of these issues lies the problem that traditional point sensors, while they can be very accurate, are limited in their spatial scope. An air temperature sensor is only able to measure the local air temperature, and not how the air temperature changes, e.g., over height. Eddy covariance measurements do measure an area in space, but the exact area depends on the wind direction, wind speed, and stability state of the atmosphere. Proper characterizations of forest sites, while possible (e.g., Dupont and Patton (2012)), requires many sensors, which complicates measurement setups and increases its cost, both upfront and in maintenance. Just as satellites see the bigger picture on a global scale, with point measurements for verification, field-sites can be improved with a high density of local distributed measurement at a scale of 1 – 1000 m. To aid in this, the novel measurement technology Distributed Temperature Sensing can be of help, as it allows measurement of temperature along a fiber optic cable, like having a long string of thermometers. This allows a much higher density of temperature measurements at field-sites, without the required effort and infrastructure discrete traditional sensors would require.

1.1.2 Distributed Temperature Sensing

A large part of this thesis revolves around measurements performed with the Distributed Temperature Sensing (DTS) technique. This technique has seen increasing use in earth sciences over the last 15 years, and has been used in a range of applications such as measuring water temperature (Selker et al., 2006; Westhoff et al., 2007; Hilgersom et al., 2016), soil temperature (Jansen et al., 2011) and air temperature (Thomas et al., 2012; De Jong et al., 2015; Zeeman et al., 2015), but also soil moisture (Steele-Dunne et al., 2010), ground heat flux (Jansen et al., 2011; Bense et al., 2016), groundwater flow (Bakker et al., 2015; Selker and Selker, 2018; des Tombe et al., 2019), and wind speed (Sayde et al., 2015; van Ramshorst et al., 2019).

DTS measurements are performed using a machine to which one or more fiber optic (FO) cables are attached. Contained in these FO cables are one or more optical fibers which can transmit light along their length through total internal refraction. The machine pulses laser light into the optical fibers and analyzes the light scattered back to the machine. This backscatter forms as optical fibers do not transmit light perfectly. This is not necessarily due to imperfections or impurities in the glass, but along the way some light will interact with the silica and germanium oxide molecules and is scattered in a random direction. Most of this scattering is elastic, as the light 'bounces off' the molecule, while retaining its original energy (Bolognini and Hartog, 2013). However, not all optical scattering is elastic. Occasionally photons interact with a molecule through the Raman effect. This can cause a photon to either absorb some vibrational energy of a molecule, thus decreasing

its wavelength; so-called 'Stokes' scattering, or to lose some energy to the molecule and increasing the wavelength; 'anti-Stokes' scattering (Raman, 1928). As the vibrational energy of a molecule is dependent on temperature, Raman scattering is as well. The warmer a molecule is, the likelier it becomes that the scattered photon gains energy (Hartog, 2017), therefore causing the ratio of Stokes to anti-Stokes scattered light to be strongly related to temperature. Apart from this temperature dependence, Raman scattering intensity is determined by the molecular makeup of the medium, which does not change appreciatively over time with fiber optic cables. This makes the use of Raman scattering well suited for fiber optic temperature measurements (Dakin et al., 1985).

To perform temperature measurements using the Raman effect, a laser light is pulsed into an optical fiber. The light scattered back through the fiber is analyzed by detectors, where the focus lies on the Raman scattered light. The intensities of the Stokes and anti-Stokes backscatter is measured, where the time-of-flight is used to determine the distance along the optic fiber where the scattering took place (Hartog, 2017).

To be able to convert these Raman Stokes and anti-Stokes measurements to temperature, the values of three parameters need to be known (Hausner et al., 2011; van de Giesen et al., 2012; Hartog, 2017; des Tombe et al., 2020). First is the sensitivity of the Stokes and anti-Stokes scattering to the fiber temperature (Bolognini and Hartog, 2013), which is a material property of the fiber. Second, as the Stokes and anti-Stokes backscatter are of different wavelengths, they do not experience the same attenuation while traveling from the point of scattering to the detectors. This 'differential attenuation' has to be corrected for (Bolognini and Hartog, 2013). Lastly, a lumped parameter, often referred to as C, corrects for any differences in signal gain caused by, e.g., detector sensitivity and losses over connectors (des Tombe et al., 2020). By use of reference sections, where the temperature of sections of fiber is accurately measured, these parameters can be calibrated, and the temperature along the entire fiber optic cable can be calculated.

One downside of using Raman scattering for temperature measurements results from Raman scattering being much more rare than, e.g., Raleigh scattering. This causes the Stokes and anti-Stokes signals to be extremely weak, and very sensitive detectors are required to properly measure the signals (Bolognini and Hartog, 2013). The weak signals result in a high uncertainty in the measurements, unless the measurements are integrated either over a longer time period or over a larger stretch of fiber. This high uncertainty in the Stokes and anti-Stokes signals will translate to high uncertainty in the temperature measurements when using DTS at high measurement frequencies and fine spatial resolutions (des Tombe et al., 2020).

1.1.3 The aim and structure of this thesis

This thesis revolves around studying the heat exchange in coniferous forests, with a focus on the current knowledge gaps; the non-closure of the energy balance and the issue of decoupling of the canopy. To this end, the aim of this thesis is to:

1. Evaluate the accuracy of DTS measurements of air temperature and humidity.

2. Use the profiles of the air temperature and humidity to estimate both evaporation and the storage of energy in the forest air column.

3. Asses decoupling at our measurement site, and increase our understanding of the interaction between forests and the atmosphere with the higher resolution data.

4. Use DTS for a higher resolution of soil temperature data for a better view on the soil thermal properties.

To put the rest of the chapters in context, chapter 2 contains descriptions of the measurement sites featured in this thesis, characterizing them by their land cover, surrounding terrain, and the structure of the vegetation.

In chapter 3 the possible errors due to short- and longwave radiation on DTS air temperature measurements are studied and characterized, as the following chapters make extensive use of air temperature measurements made with DTS.

DTS measurements of air temperature and wet bulb temperature are used in chapter 4 to measure the Bowen-ratio above a Douglas fir forest, which is used to calculate the latent and sensible heat fluxes. Additionally, the profiles are used to estimate the storage of energy within the canopy air column.

The thermal stratification within the Douglas fir canopy for data covering multiple years and seasons is analyzed in chapter 5, with the aim to characterize how common and dominant decoupling is at this site, and how high it reaches up into the canopy. From these measurements it can be concluded that some 'blocking layer'-like feature was present within the canopy, but the measurements were not of sufficient quality yet to determine the nature of this feature. To investigate this, more measurements were performed, and in chapter 6 these measurements were analyzed, and showed the regular presence of a sharp inversion layer within the canopy.

Chapter 7 contains the design and trial of a DTS-based soil temperature profile sensor, able to measure soil temperature gradients at centimeter resolution, with the aim to be able to provide a better estimate of heat storage within the top layers of the soil.

Finally, chapter 8 reflects on the main findings and provides an outlook to further research.

2

Site descriptions

Jacob van Ruisdael - De molen bij Wijk bij Duurstede (1670)

Parts of this chapter are based on:

Bart Schilperoort, Miriam Coenders-Gerrits, Willem Luxemburg, César Jiménez-Rodríguez, César Cisneros Vaca, Hubert Savenije, *Technical note: Using distributed temperature sensing for Bowen ratio evaporation measurements*, Hydrology and Earth System Sciences **22**, 819–830 (2018).

Bart Schilperoort, Miriam Coenders-Gerrits, César Jiménez-Rodríguez, Christiaan van der Tol, Bas van de Wiel, Hubert Savenije, *Decoupling of a Douglas fir canopy: a look into the subcanopy with continuous vertical temperature profiles*, Biogeosciences **17**, 6426–6439 (2020).

Bart Schilperoort, Miriam Coenders-Gerrits, César Jiménez-Rodríguez, Antoon van Hooft, Bas van de Wiel, Hubert Savenije, *Detecting nighttime inversions in the interior of a Douglas fir canopy*, Agriculture and Forest Meteorology, *under review* (2021).

The measurements presented in this study were performed at two locations, the Cabauw measurement site of the Royal Netherlands Meteorological Institute (KNMI), and the Speulderbos forest site owned by the Faculty of Geo-Information Science and Earth Observation (ITC) of the University of Twente. The Cabauw site was chosen due to its world-class instrumentation, to have highly accurate measurements to compare the DTS measured temperatures and relative humidities to. In turn, the Speulderbos site was used to study the heat exchange in a conifer canopy.

2.1 Cabauw

Located near the town of Cabauw, Utrecht, the Netherlands (51.971 ° N, 4.927 ° E) is a very well equipped meteorological measurement site maintained by the KNMI. The main feature of the 'Cabauw Experimental Site for Atmospheric Research' (CESAR) is a 213 meter tall measurement tower, where the lower layer of the atmosphere is measured in detail. Most of the surface near the tower (<500 m) is well maintained grass interspersed with small water-filled drainage ditches (Bosveld et al., 2020). To the east of the site is the town of Cabauw, and located to its south is the Lek river. Even in very dry summers, the vegetation at the site experiences very little water stress due to the high groundwater and proximity to the river. Data collected at the Cabauw site was used to verify the accuracy of DTS air temperature measurements (Chapter 3).

Figure 2.2: The location of the Cabauw Experimental Site for Atmospheric Research, along with a photo of the landscape at the site.

2.2 Speulderbos site

All measurements from Chapter 4 onwards were carried out at the 'Speulderbos' research site in Garderen, The Netherlands (52°15'N, 5°41'E, Fig. 2.3). A 48 m tall measurement tower is located within a patch of Douglas fir trees (*Pseudotsuga menziesii (Mirb.) Franco*), surrounded by a mixed forest consisting of patches of coniferous and broadleaved trees. The study site has a Oceanic Climate (Cfb) under the Köpen classification system, with a yearly average temperature of 9.8 °C and an average precipitation of 910 mm yr^{-1} (Sluijter,

2011).

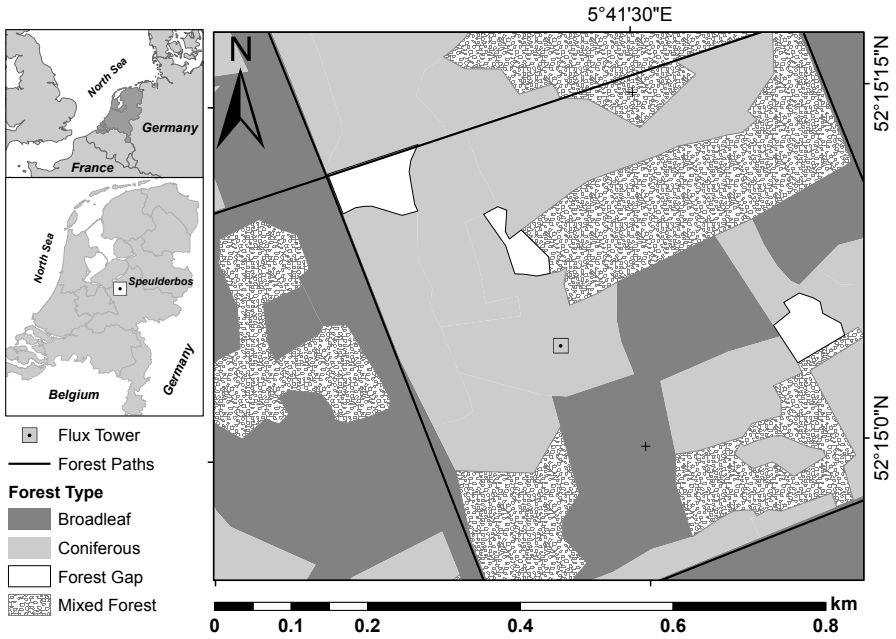

Figure 2.3: Forest type distribution around the tower site at the Speulderbos forest, the Netherlands.

Douglas fir trees were planted on the site in 1962, and they have since grown to be ~34 m tall (Cisneros Vaca et al., 2018a). Actual tree density is 571 trees per hectare, with a mean trunk diameter at breast height of 35 cm (Cisneros Vaca et al., 2018b). At the site only some sparse undergrowth is present (mosses, ferns), and most of the forest floor is covered by litter (Fig. 2.4a). A profile of the plant area index is shown in Figure 2.5. The canopy structure, uniformity of tree heights, and lack of sparse undergrowth is typical for Douglas fir plantations across Western Europe, Canada and the Western United States (Schmid et al., 2014; Winter et al., 2015; Douglas et al., 2013). The surrounding forest varies in age and height, and is intersected by access roads, which creates gaps in the canopy. As such, the overall area is heterogeneous on a scale of one kilometer (Fig. 2.3).

The canopy at the Speulderbos site is tall with a distinct vertical structure. For further consistency, we adhere to the following definitions of vertical sections, based on Parker (1995) and Nadkarni et al. (2004)). The sections are illustrated in Fig. 5.2:

- Above-canopy: includes the air mass located above the canopy layer, up to 48 m where the vertical fluxes were determined using eddy covariance measurements.

- Overstory: consists of virtually all the branches with photosynthetically active needles, located between 34 m and 20 m. This layer is fully illuminated from above and all branches receive direct sunlight. From 20 m downwards live branches are

Figure 2.4: The forest floor, showing the open understory (a) and a sky view from below (b), showing the more dense canopy top. Photos taken in July 2018.

almost absent, and the present branches are dead remnants of earlier growth stages. For further analysis we define three parts of the overstory:

  - Tree tops: top of the overstory, from 30 to 34 m, occupied by the tops of the tallest trees, but otherwise absent of vegetation.
  - Central overstory: between 25 and 30 m, starting at the most dense part of the canopy where most of the solar radiation is absorbed, to 30 m. Nearly all branches are fully illuminated.
  - Lower overstory: from 20 to 25 m, dominated by dense branches which are partially shaded by the leaves/needles above.

- Subcanopy: the section between the ground and overstory, consists of three parts:

  - Upper-understory: is composed by a region dominated by dead branches between 10 m to 20 m height.
  - Lower-understory: comprises the region between 1 m to 10 m of the forest stand. It includes the section dominated by bare tree stems, without branches or bushes.
  - Forest floor: the lower region along the forest canopy from 0 m to 1 m. At the Speulderbos site, it is dominated by the presence of organic debris (litter), mosses attached to the debris, and ferns scattered around the plot.

Speulderbos plant area index profile

To determine the vertical profile of the plant area index (PAI) at the research site, we took 10 images distributed over the height of the canopy, for 3 sides of the tower. The images

were processed using Gap Light Analyser (Frazer et al., 1999). PAI differs from the more common Leaf Area Index (LAI) by taking into account all parts of the plant, instead of only the green leaf area. The results show that the bottom 20 m of the forest are bare, while the bulk of the branches and leaves are concentrated around 20 - 30 m height (Fig. 2.5). The PAI as determined here is ~2.0, lower than the 4.5 LAI what Cisneros Vaca et al. (2018b) found in 2018. However the site experienced storms in 2018 and 2019, which removed a lot of branches, reducing the PAI.

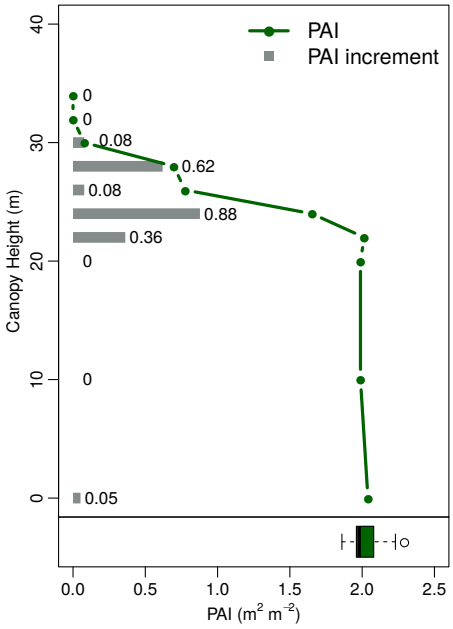

Figure 2.5: Profile of the plant area index (PAI) at the Speulderbos site.

Elevation map

The site is located on a ridge on the eastern side of a hillslope (Fig. 2.6). The local terrain varies in height from 40 – 56 meters above sea level. Within the Douglas Fir plot the surface elevation varies between 48 and 53 meters, with a local grade of ~2.5%.

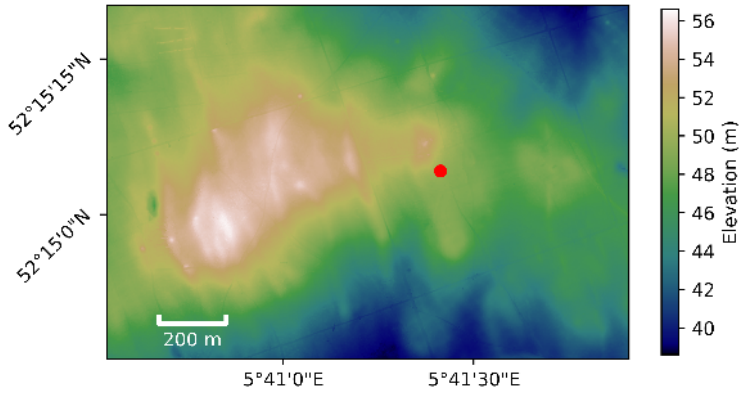

Figure 2.6: Height map of the area surrounding the measurement site. Based on the open data of 'Actueel Hoogtebestand Nederland 3' (AHN3). The red marker shows the location of the measurement tower.

3

Radiative errors in aerial DTS

Parts of this chapter are based on:

Bart Schilperoort, Miriam Coenders-Gerrits, César Jiménez-Rodríguez, Christiaan van der Tol, Bas van de Wiel, Hubert Savenije, *Decoupling of a Douglas fir canopy: a look into the subcanopy with continuous vertical temperature profiles*, Biogeosciences **17**, 6426–6439 (2020).

3.1 Introduction

In this thesis extensive use is made of distributed temperature sensing to measure air temperature. The measurements are performed by vertically suspending fiber optic cables in the air. While the temperature of the fiber optic cable can be determined with high accuracy, this temperature does not perfectly represent the air temperature and can deviate. As the DTS cables are not always shielded and not actively ventilated, (direct) sunlight shining on the fiber optic cables can cause radiative errors. Part of this shortwave radiation is absorbed by the cable, which will heat up. Darker colored cables will heat up more, but even white cables can heat up significantly. A second source of radiative error is errors due to the emission of longwave radiation. All matter continually emits energy in the form of longwave radiation, proportional to its temperature (to the fourth power). However, the emission of longwave radiation is generally compensated by the absorption of longwave radiation emitted by other objects. Outdoors, during nighttime clear sky conditions, this is not the case; due to its low temperature the clear nighttime sky emits much less longwave radiation than the land surface. This causes strong cooling of all surfaces exposed to the clear sky, and thus causes cooling of fiber optic cables suspended in the air.

As sunlight or radiative cooling affects the fiber optic cables, this causes a deviation in the measured temperature. However, if this short- or longwave radiation error would be constant in space, any spatial patterns in the measurements would not be affected. Especially in land-atmosphere interactions we are interested in vertical gradients of temperature. While the radiative heating or cooling rates are often constant over height, the cable is warmed up or cooled down by the surrounding air. This rate of heat exchange is dependent on the wind speed. As the wind speed varies over height, it will have a different effect at different heights, and thus create an error in the measured gradient.

To investigate the exact magnitude of the errors that short- and longwave radiation cause, both in absolute terms and as errors in vertical temperature gradients, we compare distributed temperature measurements to high quality reference sensors.

3.2 Method

To estimate the radiation error on the DTS-measured vertical temperature gradients, data from previous studies at the Royal Netherlands Meteorological Institute's (KNMI) Cabauw Experimental Site for Atmospheric Research (CESAR) was used (Izett et al., 2019; Monna and Bosveld, 2013; Bosveld, 2020).

The measurements were set up in a grass field, maintained at 0.1 m height at the time of the experiment. Water-filled drainage ditches were at least 50 m from the setup. In the measurement field the fiber optic cable was attached vertically to a hydraulic tower (Fig. 3.1). The DTS cable had a diameter of 6 mm with a white PVC outer coating. Measurements were performed using a Silixa Ultima-S device. The DTS data was calibrated using a single-ended setup, with a fixed differential attenuation and temperature scaling parameter. A water bath located in a climate controlled room contained two loops of fiber optic cable (outgoing and returning), and was used to determine the differential attenuation. The temperature scaling parameter was based on previous measurements with the same cable.

At approximately 25 m from the hydraulic tower, a ventilated and shielded psychrometer setup was located, measuring the air temperature at 1, 2, and 4 m height (Bosveld, 2020).

The DTS temperatures at 1, 2, and 4 m height were calculated from the mean of the 3 data points near each height, e.g., the 3 data points within the range 0.8 to 1.2 m, to reduce the measurement uncertainty.

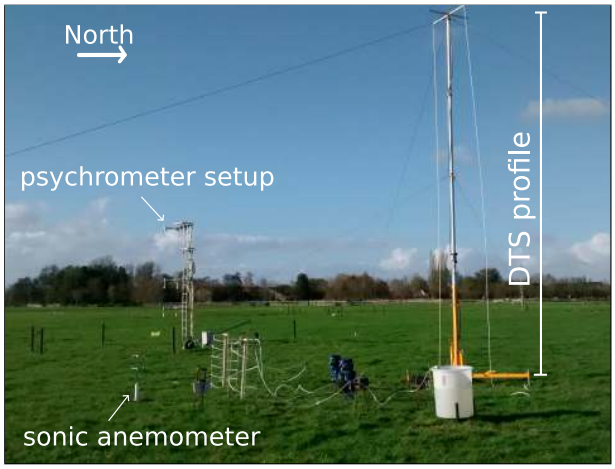

Figure 3.1: Overview of the measurement setup at CESAR, during the November 2017 experiment

Data from two separate periods were used to study the effects of radiation on the aerial fiber temperature. Data from 1 – 14 June 2017 was used to determine the effect of shortwave radiation, due to the long days with high solar intensity providing ample data for this purpose. For studying the effect of longwave radiation data from 3 – 23 November 2017 was used, which was a period characterized by low-wind clear nights.

For both the DTS and the psychrometer measurements the 10 minute mean values were calculated and used in the comparisons. For analysis all data during and 30 minutes after rainfall were discarded. When humidity exceeded 98%, the data was also discarded, to account for condensation during fog events. To calculate the gradients, the lower temperature is subtracted from the upper temperature. The DTS measurement error is calculated by subtracting the DTS-measured gradient from the psychrometer measured gradient.

For the longwave radiation analysis only nighttime data was used (when the incoming shortwave radiation was below 5 W/m^2). In November 2017 a WindMaster Pro 1352 sonic anemometer was located 6 m south from the hydraulic tower, with a measurement height of 0.6 m. The data was binned based on this wind speed.

During the June 2017 experiment the data was binned based on the KNMI measured wind speed at 0.6 m, which was measured locally but further away from the DTS measured temperature profile than the local sonic anemometer. The fiber optic cable is placed vertically and the measured radiation components are usually expressed in power per horizontal square meter. This means that sunlight coming from a high angle, e.g., at solar noon, has a different effect compared to solar radiation near sunset. For a stronger correlation between incoming shortwave radiation and the radiative error, the solar radiation has to be corrected for this fact. To this end we made use of measurements of diffuse and direct solar radiation

at Cabauw (Knap, 2017), to make an estimation of the shortwave radiation striking the vertically oriented cable ($R_{s,\rightarrow}$, W m^{-2}):

$$R_{s,\rightarrow} = R_{s,\text{diffuse}} + \cos(\alpha) \bullet R_{s,\text{direct}} \tag{3.1}$$

Where $R_{s,\text{diffuse}}$ is the diffuse solar radiation (W m^{-2}), α the solar altitude (°), and $R_{s,\text{direct}}$ is the direct solar radiation (W m^{-2}). Any reflection of solar radiation by the grass, as well as the absorption spectrum of the cable coating, has not been taken into account.

3

3.3 Shortwave radiation error estimation

3.3.1 Absolute error

To study the absolute error due to shortwave radiation we compare the difference between the 10-minute mean DTS and psychrometer temperatures to the incoming shortwave radiation. The measurement error due to shortwave radiation is approximately linear to the incoming radiation (Fig. 3.2), and weakly related to the wind speed. At the highest solar intensities the error is around 1.0 K, but up to 1.5 K in case of low wind speeds.

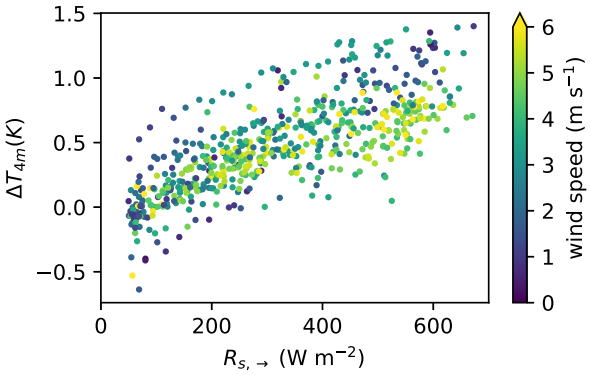

Figure 3.2: Difference between the psychrometer and DTS measured temperatures (ΔT) at 4 m (positive numbers indicate a colder fiber optic cable), compared to horizontal component of the incoming shortwave radiation and 0.6 m wind speed.

3.3.2 Gradient error

While the absolute errors are very large, the picture is much better when looking at the measured temperature gradients (Fig. 3.3). Mean errors are in the order of -0.02 K m^{-1}, and there is a weak correlation between the errors and wind speed (r = −0.10) or incoming radiation (r = 0.24). The measurement error is mostly negative; this is consistent with the expected error. As the wind speed closer to the ground is lower, the deviation in the cable temperature from the air temperature is higher there. This causes a negative error in the gradient.

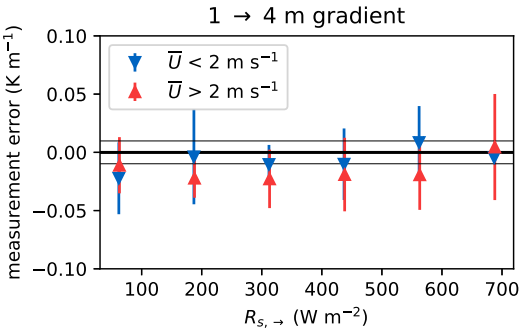

Figure 3.3: Error in the DTS-measured gradient between 1 and 4 m. Data are binned by the horizontal component of the incoming shortwave radiation. Split into 0.6 m wind speeds under 2 m/s (blue, n=114) and over 2 m/s (red, n=490). Grey lines indicate +/- 0.01 K. Error bars show +/- 1 standard deviation.

3.4 Longwave radiation error estimation

3.4.1 Absolute temperature error

To start we compare the absolute temperature of the fiber optic cable to the psychrometer measured temperature (Fig. 3.4). The error is strongly dependent on the net longwave radiation and wind speed, with an error of up to 1.0 K during strong cooling and a lack of wind. The results are much more clear and conclusive than in the shortwave radiation case. Closer to the surface the error is larger (up to 1.5 K at 1 m), as the wind speed is lower there.

The strongest cooling rate at the surface was observed during higher wind speeds, while with extremely low wind speeds cooling rates did not exceed 50 W m^{-2}. This is to be expected, as the surface will be able to cool down much more during low wind conditions, and as it is colder it will emit less longwave radiation. During higher wind speed conditions the air is able to resupply heat to the surface, keeping it at a higher temperature which lets it emit more longwave radiation.

3.4.2 Gradient error

For the gradient between 2 and 4 m, the error for higher wind speeds was below 0.01 K m^{-1} across nearly the entire range of longwave radiation (Fig. 3.5). For low wind speeds, the error varied stronger with longwave radiation, and the error had a much higher variation. A reason for this high variation could be heterogeneity at the site, which has a stronger influence during extremely stable atmospheric conditions.

The gradient between 1 and 4 m has a larger error compared to the 2 to 4 m gradient (Fig. 3.6), as the difference in wind speed between 1 and 4 m is much greater. For the lower range of cooling rate and with higher wind speeds, the error is not much greater than the lapse rate correction. However, with strong cooling rates ($R_{L,net}$ > 20 W m^{-2}) and a low wind speed, the error becomes very large.

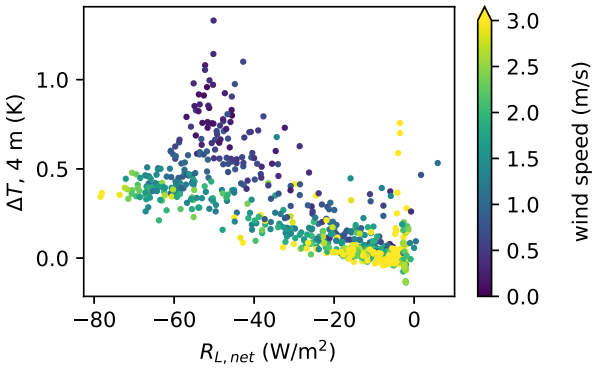

Figure 3.4: Difference between the psychrometer and DTS measured temperatures (ΔT) at 4 m (positive numbers indicate a colder fiber optic cable), compared to net longwave radiation and 0.6 m wind speed.

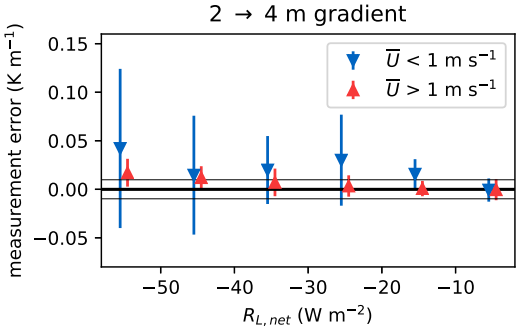

Figure 3.5: Error in the DTS-measured gradient between 2 and 4 m. Data are binned by the net longwave radiation. Split into 0.6 m wind speeds under 1 m/s (blue, n=207) and over 1 m/s (red, n=544). Grey lines indicate +/- 0.01 K. Error bars show +/- 1 standard deviation.

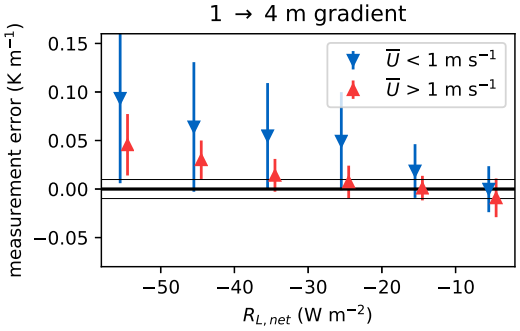

Figure 3.6: Error in the DTS-measured gradient between 1 and 4 m. Data are binned by the net longwave radiation. Split into 0.6 m wind speeds under 1 m/s (blue, n=207) and over 1 m/s (red, n=544). Grey lines indicate +/- 0.01 K. Error bars show +/- 1 standard deviation.

3.5 Conclusion

Both sunlight and radiative cooling strongly influence the accuracy of aerial DTS measurements. Strong direct sunlight can cause errors of up to 1.5 K, and measuring under these conditions will require shielding the cable from sunlight. However, when measuring vertical gradients the errors are less significant, and depending on the accuracy required no shielding would be necessary. Radiative cooling can also cause absolute errors of up to 1.5 K and gradient errors of up to 0.05 K m^{-1}, but this is only in extreme conditions (strong cooling and low wind speeds). Measurements performed under more modest cooling rates (<25 W m^{-2}) or with high wind speeds do not suffer from significant errors.

4

Using DTS for Bowen ratio evaporation measurements

View of the treetops at the Speulderbos measurement site

This chapter is based on:

Bart Schilperoort, Miriam Coenders-Gerrits, Willem Luxemburg, César Jiménez-Rodríguez, César Cisneros Vaca, Hubert Savenije, *Technical note: Using distributed temperature sensing for Bowen ratio evaporation measurements*, Hydrology and Earth System Sciences **22**, 819–830 (2018).

4.1 Introduction

In recent years distributed temperature sensing (DTS) technology has quickly improved (Bao and Chen, 2012). The precision and spatial resolution now allow its widespread use in hydrological and atmospheric sciences (Selker et al., 2006; Thomas et al., 2012), from measuring groundwater flow (Blume et al., 2013) and seepage into streams (Westhoff et al., 2007), to soil moisture (Steele-Dunne et al., 2010), soil heat flux (Bense et al., 2016), and wind speed (Sayde et al., 2015). First introduced by Euser et al. (2014), DTS can also be used for measuring the Bowen ratio, to estimate the evaporation flux. A dry and wet stretch of the same fiber optic cable are installed vertically to obtain the so-called dry and web bulb temperature gradient, respectively. This method mitigates some problems of the conventional Bowen ratio, since usually at least two different sensors are used to measure the temperature and vapor pressure gradients, of which each has its own independent error (Angus and Watts, 1984; Fuchs and Tanner, 1970). The DTS based Bowen ratio does not suffer from this drawback, by having a large amount of data points over the height (up to 8 per meter) with only a single sensor. It can have a resolution of 0.06 K for 1 minute averages, and will be more accurate when measuring over a longer time period, allowing for very small temperature gradients to be measured.

In addition to estimating the latent and sensible heat flux, the measurements can also be used to get a better understanding of the processes taking place in complex ecosystems, such as forests. A vertical temperature and humidity profile is available in high resolution and precision, both above, inside, and under the canopy. DTS can also estimate different components of the energy balance, such as the heat storage in the air column, and the soil heat flux (Jansen et al., 2011). Finally, it can be used to increase our understanding of the energy exchange between the canopy and undergrowth layers by looking at the air temperature gradient under the canopy.

Here we elaborate on the method of Euser et al. (2014), by considering more energy balance components like the latent and sensible heat storage in the air column, including a data-quality system, and using the potential air temperature. The performance of the method is tested in a mixed forest in the Netherlands by looking at the accuracy of the DTS measured air temperature and wet-bulb temperature, compared to reference temperature and humidity sensors. It appears that solar radiation can have a significant influence on the cable temperature, which can be mitigated by providing artificial shadow. Lastly the fluxes resulting from the method are compared to an eddy covariance (EC) system, and the sources of differences between the methods are shown.

4.2 Materials and Methods

4.2.1 Theory

The Bowen ratio energy balance method (BREB) combines the energy balance with the Bowen ratio (Oliphant et al., 2004). The energy balance can be described by:

$$R_N + A = \rho\lambda E + H + G_S + \frac{\mathrm{d}Q}{\mathrm{d}t} \tag{4.1}$$

where R_N is the net radiation (W m^{-2}), $\rho\lambda E$ the latent heat flux (W m^{-2}), H the sensible heat flux (W m^{-2}), G_S the soil heat flux (W m^{-2}), and $\frac{\mathrm{d}Q}{\mathrm{d}t}$ is the change of energy storage in

the system (W m^{-2}). A represents a net advection of energy into the system (W m^{-2}), but is assumed to be 0. The energy flux associated with photosynthesis (G_P) was not measured, and is therefore not included in the equation. The Bowen ratio (β) is the ratio of the sensible heat flux to the latent heat flux and can be approximated using the air temperature gradient and the vapor pressure difference over the height (Bowen, 1926):

$$\beta = \frac{H}{\rho\lambda E} \approx \gamma \frac{\Delta T_a}{\Delta e_a} \tag{4.2}$$

where γ is the psychrometric constant (kPa K^{-1}) (see Eq. 4.10), ΔT_a the difference in air temperature between two heights (K) and Δe_a the difference in actual vapor pressure between the two heights (kPa). However, when gradients are very small, the adiabatic lapse rate can not be neglected (Barr et al., 1994). Therefore the potential temperature should be used instead:

$$\beta = \frac{H}{\rho\lambda E} = \frac{c_p}{\lambda} \frac{\partial\theta/\partial z}{\partial q/\partial z} = \gamma \frac{\partial\theta/\partial z}{\partial e_a/\partial z} \tag{4.3}$$

where c_p is the specific heat of air (MJ kg^{-1}) (See Eq. 4.6), λ the latent heat of vaporization (2.45 MJ kg^{-1} K^{-1}), θ the potential temperature (K), q the specific humidity (kg kg^{-1}) (See Eq. 4.7) and z the height above the ground (m). The potential temperature gradient can be approximated by the right-hand side of Eq. 4.4, as the ratio $\frac{\theta}{T_a}$ is nearly 1 (Pal Arya, 1988).

$$\frac{\partial\theta}{\partial z} = \frac{\theta}{T_a}\left(\frac{\partial T_a}{\partial z} + \Gamma\right) \approx \frac{\partial T_a}{\partial z} + \Gamma \tag{4.4}$$

where T_a is the air temperature (K), and Γ is the adiabatic lapse rate (typically around 0.01 K m^{-1}). The numerical implementations of Eq. 4.3 & 4.4 are explained in section 4.2.3 Data Processing. Under dry and unsaturated conditions the lapse rate is equal to (Pal Arya, 1988):

$$\Gamma = \frac{g}{c_p} \tag{4.5}$$

where g is the gravitational acceleration (9.81 m s^{-2}). The specific heat capacity of air is determined by (Stull, 2015):

$$c_p = 1.004 + 1.84q \tag{4.6}$$

And the specific humidity by (Pal Arya, 1988):

$$q = \varepsilon \frac{e_a}{P} \tag{4.7}$$

where ε is the ratio of molecular mass of water vapor to dry air (0.622), and P the atmospheric pressure (kPa). The actual vapor pressure is determined by (Allen et al., 1998):

$$e_a(T_a) = e_s(T_w) - \gamma(T_a - T_w) \tag{4.8}$$

where T_w is the wet-bulb temperature (K), and e_s the saturation vapor pressure (kPa) given by (Koutsoyiannis, 2012):

$$e_s(T_w) = 0.61 \cdot \exp\left(\frac{19.9 \cdot T_w}{273 + T_w}\right) \tag{4.9}$$

The psychrometer constant is related to the air pressure and ventilation of the psychrometer (Harrison and Wood, 2012; Allen et al., 1998). If sufficiently ventilated, the psychrometric constant is defined by (Allen et al., 1998):

$$\gamma = \frac{c_p P}{\varepsilon \lambda} = 0.665 \times 10^{-3} \cdot P \tag{4.10}$$

As the air pressure also varies over height, the measurements have to be corrected for elevation using the following approximation (Stull, 2015, p. 8):

$$P(z) = P_0 \cdot \exp(-z/7290) \tag{4.11}$$

with P_0 being the pressure at sea-level (kPa). By combining the Bowen ratio (Eq. 4.3) with the energy balance (Eq. 4.1), the latent heat flux and sensible heat flux can be determined:

$$H = \frac{R_N - G_S - \frac{\mathrm{d}Q}{\mathrm{d}t}}{1 + \frac{1}{\beta}} \tag{4.12}$$

$$\rho\lambda E = \frac{R_N - G_S - \frac{\mathrm{d}Q}{\mathrm{d}t}}{1 + \beta} \tag{4.13}$$

The storage component in the energy balance has multiple parts, ranging from the storage of heat in the soil, to the storage of heat in the form of water vapor in the air column:

$$\frac{\mathrm{d}Q}{\mathrm{d}t} = \frac{\mathrm{d}Q_H}{\mathrm{d}t} + \frac{\mathrm{d}Q_E}{\mathrm{d}t} \tag{4.14}$$

The changes in storage of heat and water vapor in the air column below the height at which the energy fluxes (R_N, H and $\rho\lambda E$) are measured, are represented by $\frac{\mathrm{d}Q_H}{\mathrm{d}t}$ and $\frac{\mathrm{d}Q_E}{\mathrm{d}t}$ respectively (W m^{-2}). The change in biomass heat storage ($\frac{\mathrm{d}Q_B}{\mathrm{d}t}$) was not measured, and is therefore not included in this equation. $\frac{\mathrm{d}Q_H}{\mathrm{d}t}$ and $\frac{\mathrm{d}Q_E}{\mathrm{d}t}$ are defined as (Barr et al., 1994):

$$\frac{\mathrm{d}Q_H}{\mathrm{d}t} = \int_0^z \rho_a c_p \frac{\mathrm{d}T_a}{\mathrm{d}t} \mathrm{d}z \tag{4.15}$$

$$\frac{\mathrm{d}Q_E}{\mathrm{d}t} = \int_0^z \rho_a \lambda \frac{\mathrm{d}q}{\mathrm{d}t} \mathrm{d}z \tag{4.16}$$

4.2.2 Setup

The measurements were performed at the Speulderbos study site (Ch. 2), where fiber optic cables were placed vertically along a 48 m tall measurement tower. Two cables with different diameters were used. The first cable has a diameter of 6 mm and has both a dry and a wetted stretch. To wet the cable it was wrapped in cloth, and water was supplied to it continuously. A second cable with a diameter of 3 mm was used to study the effects of solar radiation, as a thinner cable will warm up less (De Jong et al., 2015). However, this method added additional uncertainties due to the required extrapolation and the 3 mm cable was not used in this study. Both cables were connected to the same DTS machine (in single-ended mode) and calibrated with a single calibration bath (see Fig. 4.2)

The DTS machine used was the Silixa Ultima (Silixa Ltd, 2017), which has a sampling resolution of 12.5 cm, measurement resolution of 35 cm, and a measurement standard deviation of 0.06 K at a 1 minute time resolution.

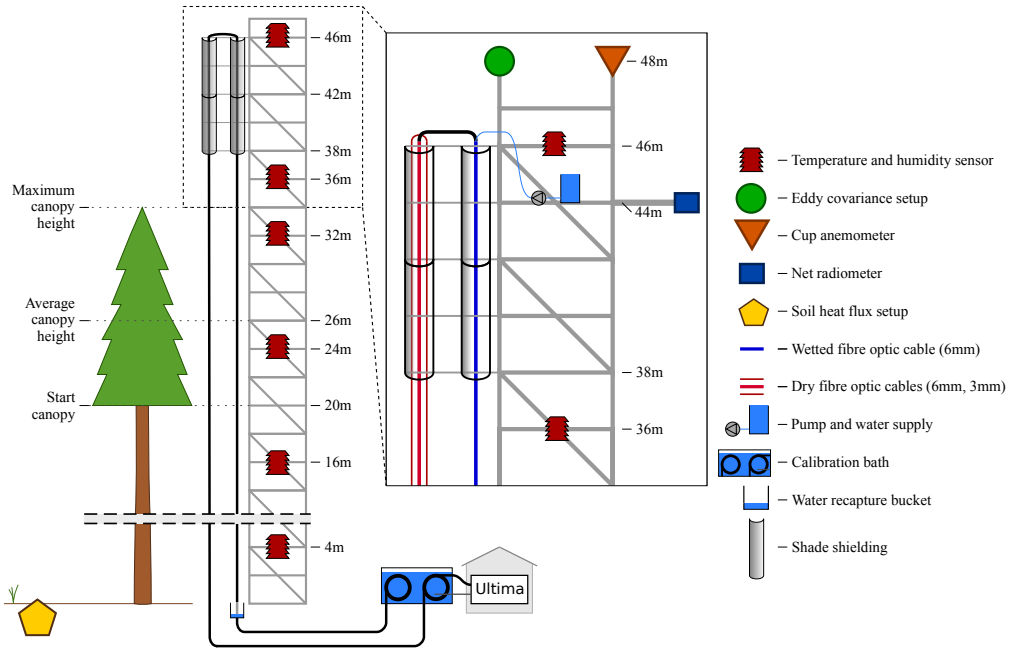

Figure 4.2: Schematic overview of the measurement setup at the tower.

The fiber optic cable with a diameter of 6 mm was secured at the top of the tower, with the dry stretch hanging 1.2 m away from the tower, and the wet stretch 0.25 m away. The cable with a diameter of 3 mm was secured next to the dry 6 mm cable. The response times of the cables are in the order of 2 - 3 minutes for the 6 mm cable, and 20 to 40 seconds for the 3 mm cable. The cables were secured at multiple locations distributed over the height (in and above the canopy, see Fig. 4.2), using loops (with a diameter of 5 cm) to prevent direct contact with the support structure. For both cables a stretch of 10 m at both the start and end was placed in a calibration bath, an enclosed Styrofoam box filled with water, along with two Pt100 temperature probes that were connected to the DTS machine.

An aquarium air pump was installed in the Styrofoam box to ensure a homogeneous temperature distribution. The cables were shielded from direct solar radiation using screen gauze secured onto PVC rings, see Fig. 4.3. Only the southern 180 degrees of the cables was shielded, to allow for sufficient ventilation. The screen gauze had holes 1.5 mm wide, and the mesh material had a diameter of 0.3 mm. Two layers of the gauze were used. Each segment of shield was 2 m long, and was secured to the tower with a horizontal beam. Due to the angle of the incident sunlight the gauze was able to block most direct sunlight, except during the early morning. To supply the wet cable with water, a reservoir was installed near the top of the tower, along with a pump. The pump speed was set to 1500 ml h^{-1} during sunny days without rainfall, and to 800 ml h^{-1} on other days, which was enough to keep the cable wet over the entire height, while keeping the influence of relatively warm water at the top of the cable at a minimum. As water supplied at the top has a higher temperature than the wet bulb temperature, the top two meters of wet cable data was excluded from the data analysis to allow the slowly flowing water to reach the wet bulb temperature.

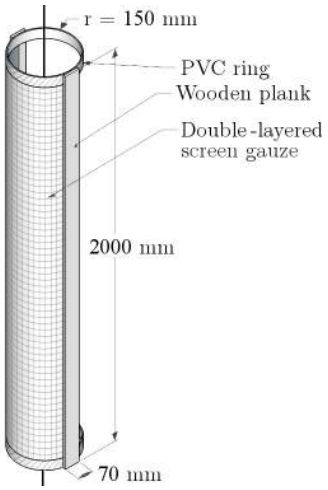

Figure 4.3: Schematic of one 2 m segment of the solar screen construction.

A net radiometer (Kipp & Zonen CNR4) was located on the top of the tower (48 m), measuring both incoming and outgoing short- and longwave radiation. One minute averages were logged. On the tower six humidity and temperature sensors were located over the height, at 4, 16, 24, 32, 36 and 46 meters above ground level. The lower four were Rotronic HC2-S3C03 sensors (with active ventilation), and the top two were Campbell CS216 sensors with passive ventilation. The sensors were inter-calibrated to the sensor at 24 meters. The temperature and humidity was logged at one minute averages.

At the top of the tower an eddy covariance system was installed to measure the sensible and latent heat fluxes. It consisted of a Campbell CSAT3 sonic anemometer and a Li-Cor Biosciences LI7500 gas analyzer connected to a CR5000 Campbell data logger, to which the data was logged at 20 Hz.

Two cup anemometers (Onset S-WSB-M003) were used to measure the wind speed,

one at the top of the tower (48 m), and one below the canopy (4 m). The data from the lower anemometer lacks the resolution to properly measure the low wind speeds below the canopy, which are at times too low to be registered. One minute average wind speeds, along with the maximum gust speeds were logged.

The biomass heat storage change and the photosynthesis energy flux were not measured. The biomass heat storage change is estimated to have a maximum of 45 W m^{-2}, and the photosynthesis energy flux is estimated to be in the order of 5 W m^{-2} (Barr et al., 1994; Michiles and Gielow, 2008). For the soil heat flux, the soil temperature was measured at different depths (1, 3, 4, 8, 20, 50 cm). Soil moisture was measured using Campbell Sci. Inc. CS616 water content reflectometers. Thermal conductivity was fitted to soil heat flux measurements done at 8 cm. The soil heat flux was then determined using the harmonics method (van der Tol, 2012).

4.2.3 Data Processing

The DTS machine was set to measure the cable temperature at one minute averaging intervals. For the comparison with reference temperature sensors, this one minute resolution data is used. To compare the wet-bulb temperature measured by the fiber optic cable to the reference sensors, the reference wet-bulb temperature is iteratively derived from the reference air temperature and relative humidity (as no analytical 'reverse' equation exists to calculate T_w from T_a and relative humidity (Stull, 2011)). For the purpose of calculating the Bowen ratio, the temperature and actual vapor pressure are averaged over time for 15 minute time periods. For DTS Bowen ratio calculations, the temperatures between 38.5 m and 44 m are used. This area is shaded from the sun by the screen gauze, and at the top of the stretch the new water on the wet cable has reached the wet-bulb temperature.

When calculating the gradients for the Bowen ratio, the 15 minute average temperature and vapor pressure are fit to the natural logarithm of the height, in the following form:

$$T_{a,\text{fit}} = a \cdot \ln(z) + b \tag{4.17}$$

This allows making use of the entire temperature profile this way, rather than just a few DTS measurement points, therefore reducing measurement uncertainty. A logarithmic shape of the profiles was assumed based on Monin-Obukhov similarity theory. A linear fit was also looked at, but it resulted in a minimal difference in the resulting fit. From the fits the temperature difference over height is then calculated:

$$\begin{aligned}\frac{\partial \theta}{\partial z} &\approx \frac{\partial T_a}{\partial z} + \Gamma(z) \approx \frac{\Delta T_{a,\text{fit}}}{\Delta z} + \Gamma(z) \\ &\approx \frac{T_{a,\text{fit}}(z=44) - T_{a,\text{fit}}(z=38.5)}{44-38.5} + \Gamma(\bar{z}=41.25)\end{aligned} \tag{4.18}$$

$$\frac{\partial e_a}{\partial z} \approx \frac{\Delta e_{a,\text{fit}}}{\Delta z} = \frac{e_{a,\text{fit}}(z=44) - e_{a,\text{fit}}(z=38.5)}{44-38.5} \tag{4.19}$$

Where $\Delta T_{a,fit}$ is the difference in air temperature (K) of the fitted temperature curve, between the top and bottom of the height range used for the Bowen ratio. $\Delta e_{a,fit}$ is the difference in vapor pressure (kPa) of the fitted vapor pressure curve between those heights.

Δz is the difference in height (m). The coefficients of determination of the regressions of the temperature and vapor pressure, $r_{T_a,z}$ and $r_{e_a,z}$, can be used for determining the goodness of fit. A high (positive or negative) regression means that the logarithmic slope (of the 15 minute average) is very well defined.

To calculate the air column storage terms $\frac{\mathrm{d}Q_H}{\mathrm{d}t}$ and $\frac{\mathrm{d}Q_E}{\mathrm{d}t}$ (Eq. 4.15 & 4.16), the DTS measured temperature and vapor pressure are used, except for the center of the canopy where DTS data is not accurate due to the sunlight and lack of screens in the canopy. The temperature and specific humidity are integrated over the height from 0 to 41 m, up to the height of the Bowen ratio measurements.

As quality control scheme for the DTS-Bowen ratio, two flags are used. The first flag tests the correlation coefficient of the actual vapor pressure over height, for which we chose a lower limit of 0.20 (Eq. 4.20). We do not consider $r_{T_a,z}$ of the air temperature gradient as it is always higher than $r_{e_a,z}$ (as the uncertainty in e_a is higher due to the propagation of errors in T_a and T_w). The second flag is for the case where the Bowen ratio approaches -1, which causes the uncertainty in the BREB fluxes to be very high, as the denominator of Eq. 4.12 and Eq. 4.13 approaches 0 (J. O. Payero et al., 2003).

$$\text{Flag 1} : r_{e_a,z}^2 > 0.20 \tag{4.20}$$

$$\text{Flag 2} : \beta < -1.1 \text{ or } \beta > -0.9 \tag{4.21}$$

If flag 1 is true, the outcome of the Bowen ratio calculation is considered reliable. The other data points are removed from further analysis. If flag 2 is also true, then the Bowen ratio can be used for calculating the atmospheric heat fluxes.

After processing the eddy covariance data using LI-COR's EddyPro® software (LI-COR Inc., 2016), several quality flags are available. The quality flag system used is from Mauder and Foken (2006), ranging from 0 (best) to 2 (worst). The eddy covariance fluxes with a quality flag of 0 or 1 are used in this research.

To summarize, the method of this paper differs in a few points from Euser et al. (2014). The fit of the Bowen ratio temperature and vapor pressure profiles is done separately, to get the correct ratio, as $\frac{\partial T}{\partial z} / \frac{\partial e_a}{\partial z} \neq \frac{\partial T}{\partial e_a}$. More energy balance storage terms are taken into account, namely the latent and specific heat storage in the air column. The potential temperature is used instead of the air temperature, to correct for the lapse rate. The local air pressure is taken into account in the calculations, as it has an influence on the psychrometric constant, specific heat capacity and specific humidity. Lastly, a system for simple quality flags is introduced to allow for simple objective quality control.

4.3 Results and Discussion

4.3.1 Meteorological Conditions

For the comparison of the DTS temperature with the reference temperature data (Section 4.3.2), the days 10-22 August 2016 are used.

For a good comparison between DTS and EC, both devices should work properly. Due to several technical problems with data collection, only 11 days within the measurement

campaign have both eddy covariance and DTS data available, namely 10, 12-14, 19-22, and 28-30 August 2016. On the other days data is missing in either the eddy covariance or the DTS. The meteorological conditions of these days are shown in Figure 4.4. All days were partially clouded, or completely clouded. The wind direction was mainly west and north-east. Above the canopy the wind speed varied between 2 and 6 m s^{-1}, while under the canopy the wind speed was often too low to be measured with the cup anemometer (under 0.4 m s^{-1}).

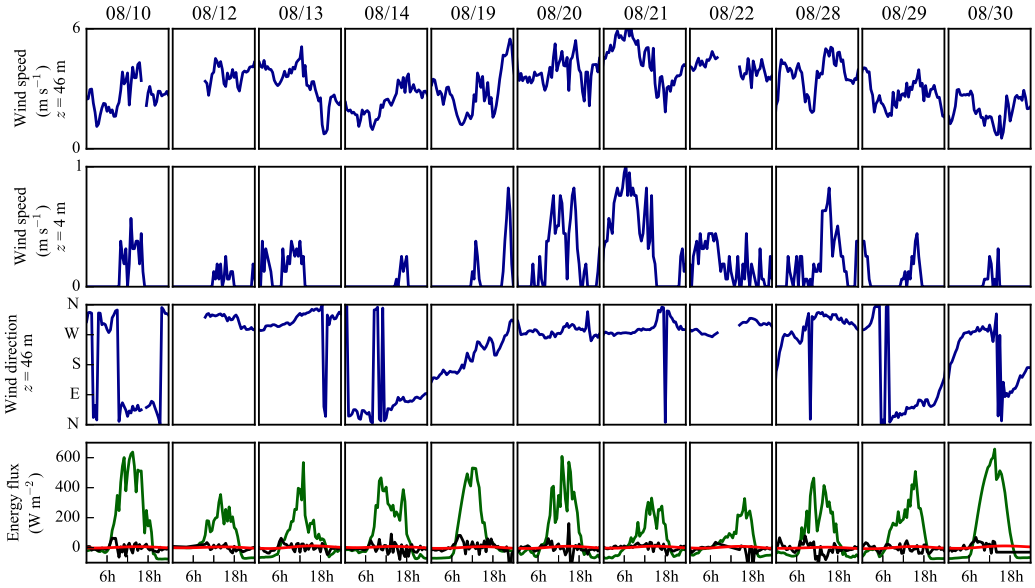

Figure 4.4: Meteorological conditions during the days that both DTS and eddy covariance data was available. From top to bottom: wind speed at the top of the tower, wind speed at the bottom of the tower, wind direction at the top of the tower, and the measured energy fluxes (green: net radiation, red: soil heat flux, black: energy storage change $\frac{dQ}{dt}$).

4.3.2 Temperature validation

In Fig. 4.5 the comparison between the 6 mm DTS cable and the reference sensor is shown. For the above canopy comparison, the 46 m reference sensor is compared to the cable temperatures at 44 m height, as the temperatures at the top are unreliable due to influence from the sun and the warm water from the reservoir. Below the canopy the dry cable temperature correlates perfectly with the reference sensor temperature (Fig. 4.5e). In and above the canopy incoming solar radiation warms up the fiber optic cable (Fig. 4.5a, 4.5c), which causes an error at 34 m where no screen was installed. This error is a deviation of up to 3 K from the reference sensor temperature (for 1 minute temperature averages). The comparison at 34 m also has an offset, this is a constant error of about 1 K, due to the reference temperature sensor drift and inter-calibration problems. The addition of screens above the canopy largely reduces the error from solar radiation to under 1 K, leading to a very good agreement between the two sensor types (Fig. 4.5a).

Below the canopy the wet cable temperature is in good agreement with the reference wet-bulb temperature (Fig. 4.5f), even though wind speeds were often low. This shows that the wet cable gives a good estimate of the wet-bulb temperature. At 34 m, where no screens were placed, the error in the wet-bulb temperature is larger than the error in the air temperature. Deviations of up to 4 K occur in the measurement period. The shielded top part of the wet cable performs much better (Fig. 4.5b), and errors are small (under 1 K).

4.3.3 Bowen ratio verification

The Bowen ratio resulting from the BR-DTS method (β_{DTS}) is compared to the eddy covariance Bowen ratio (β_{EC}), at a 15 minute averaging interval. In Figure 4.6 the correlation between the eddy covariance Bowen ratio estimate and the BR-DTS is shown. It shows a grouping around the 1:1 line, and a good correlation (r^2 = 0.59). The eddy covariance Bowen ratio was only calculated for fluxes with an absolute value larger than 10 W m^{-2}, as the uncertainty of the eddy covariance Bowen ratio is very high when the fluxes are small. Even the negative (night-time) values seemed to be accurate, since they passed the quality control flags. However, both eddy covariance and BR-DTS have problems measuring the night-time Bowen ratio. For eddy covariance this is due to the lower friction velocity at night (Wilson, 2002), while for the BR-DTS method the gradients are very small due to the small fluxes.

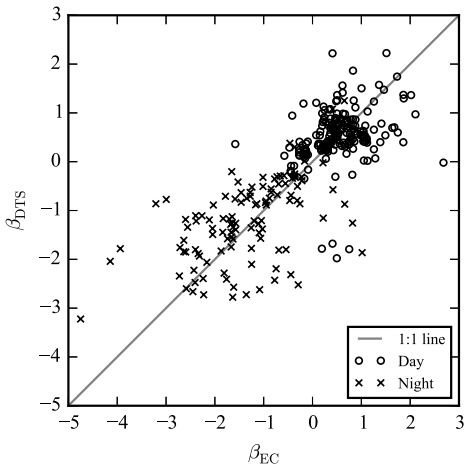

Figure 4.6: Correlation between the DTS measured (β_{DTS}) and eddy covariance measured (β_{EC}) Bowen ratios. Daytime data is between 7:00 and 18:00. Data from 10, 12-14, 19-22, and 28-30 August. R^2=0.59. RMSE=0.81. n = 319 data points.

One drawback of the DTS based Bowen ratio, is the assumption that the eddy diffusivity of heat and water vapor are the same. In reality these eddy diffusivities can be dissimilar (Irmak et al., 2014). This can cause an error (both a bias and extra noise) in the Bowen ratio as measured by the temperature and vapor pressure gradients compared to the eddy covariance Bowen ratio. Another source of differences between β_{DTS} and β_{EC}, is that the two are measured at different heights.

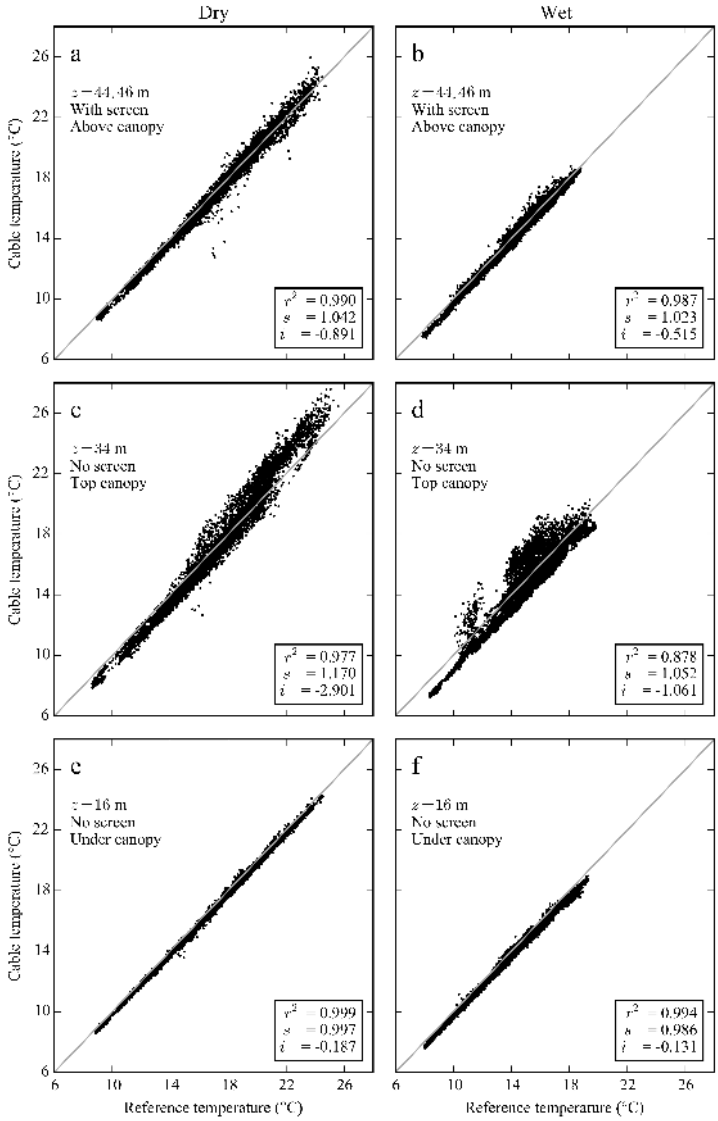

Figure 4.5: Comparison between the 6 mm DTS cable and reference temperatures. Grey line shows 1:1 correlation. Data from 10-23 August 2016. **a**: Dry cable at 44 m and reference air temperature at 46 m, the cable is shielded by the screen. **b**: Wet cable at 44 m and reference wet-bulb temperature at 46 m, the cable is shielded by the screen. **c**: Dry cable and reference air temperature at 34 m, the cable is exposed to direct sunlight. **d**: Wet cable and reference wet-bulb temperature at 34 m, the fiber optic cable is exposed to direct sunlight. **e**: Dry cable and reference air temperature at 16 m, under the canopy so less direct sunlight hits the fiber optic cable. **f**: Wet cable and reference wet-bulb temperature at 16 m, under the canopy so less direct sunlight hits the fiber optic cable. Shown are the linear correlation coefficients; the coefficient of determination (r^2), the slope (s), and the intercept (i).

During the measurement period the 80% fetch of the EC system was between 200 and 300 m. By applying the findings of Stannard (1997), the Bowen ratio 80% equilibrium ratio would be reached at a fetch to height ratio of 20 to 40. This corresponds to a distance of 350 to 700 m. The fetch of the Bowen ratio will therefore not be equal to the eddy covariance fetch, which could cause some differences in measured fluxes.

4.3.4 Energy balance closure

A known problem in measuring fluxes is that the energy balance often does not close well. This is caused by differences in fetch between the used devices, device inaccuracies, and possibly problems with the eddy covariance method (Wilson, 2002). Part of the difference between the BR-DTS method and the eddy covariance method may be explained by this energy balance closure problem. Eddy covariance measurements have a fetch, which does not include the area close to the flux tower. The available energy in the BR-DTS method depends on measurements of net radiation, ground heat flux and heat storage change ($\frac{\mathrm{d}Q}{\mathrm{d}t}$) close to the tower. Heterogeneity in the fetch may cause differences between the two methods. In addition, the biomass heat storage change ($\frac{\mathrm{d}Q_\mathrm{B}}{\mathrm{d}t}$) was not measured for the BR-DTS method, and assumed to be 0 W m^{-2}. The photosynthesis energy flux (G_P) was also assumed to be 0 W m^{-2}.

To investigate the energy balance closure for the two methods, we summed up the available fluxes in the following equations, where $\frac{\mathrm{d}Q}{\mathrm{d}t}$ is the storage term from Eq. 4.14:

$$B_\mathrm{DTS} = R_N - G_S - \frac{\mathrm{d}Q}{\mathrm{d}t} \tag{4.22}$$

$$B_\mathrm{EC} = H_\mathrm{EC} + \rho\lambda E_\mathrm{EC} \tag{4.23}$$

where B_DTS is the energy available for heat fluxes in the BR-DTS method (W m^{-2}) and B_EC is the sum of the eddy covariance measured heat fluxes (W m^{-2}).

To compare the two measurement methods, a Tukey mean-difference (or Bland-Altman) plot was made (Fig. 4.7) (Altman and Bland, 1983). The mean of the two measurement methods is plotted against the difference between them. The mean difference (μ) between B_DTS and B_EC is a 3.4 W m^{-2} underestimation by the BR-DTS method. At low fluxes (below 100 W m^{-2}), the BR-DTS method measures less energy available for fluxes compared to eddy covariance. At high fluxes (over 400 W m^{-2}) the opposite is visible. One possible reason for this is that the biomass heat flux ($\frac{\mathrm{d}Q_\mathrm{B}}{\mathrm{d}t}$) was not measured, which causes an underestimation of the available energy in B_DTS during the night, and an overestimation during the day.

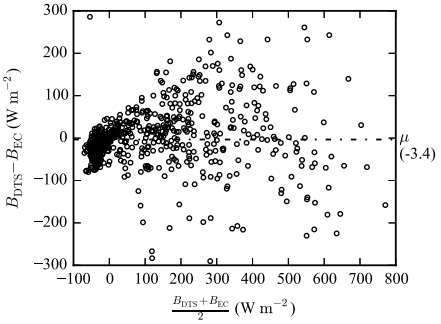

Figure 4.7: Tukey mean-difference plot comparing B_{DTS} and B_{EC}. With μ = −3.4 W m^{-2}, RMSE = 76 W m^{-2}, n = 741 data points. (15 minute averages). Data from 10, 12-14, 19-22, and 28-30 August 2016.

4.3.5 Energy fluxes

Figures 4.8 and 4.9 show the mean difference plots comparing the latent and sensible heat fluxes of the eddy covariance method to the BR-DTS method. The BR-DTS fluxes are calculated above the canopy, using only temperature data from the shielded cables. The Tukey mean-difference plot for the latent heat flux shows no large bias when comparing the BR-DTS method to eddy covariance, with the mean difference being a 18.7 W m^{-2} overestimation by the BR-DTS method (Fig. 4.8).

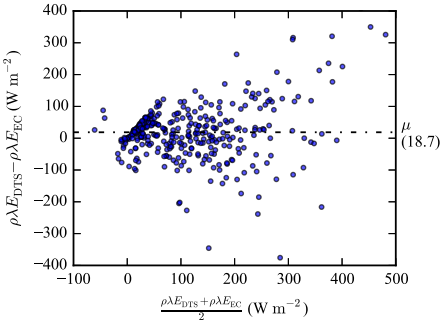

Figure 4.8: Tukey mean-difference plot comparing $\rho\lambda E_{EC}$ and $\rho\lambda E_{DTS}$. With μ = 18.7 W m^{-2}, RMSE = 90 W m^{-2}. (15 minute averages). Data from 10, 12-14, 19-22, and 28-30 August 2016.

The Tukey mean-difference plot comparing the sensible heat flux (Fig. 4.9) shows a strong negative bias for negative fluxes, resulting from the negative bias in the energy balance comparison (Fig. 4.7). At positive fluxes there seems to be a positive bias (H_{DTS} > H_{EC}). The mean difference is small, being a 10.6 W m^{-2} underestimation by the BR-DTS method.

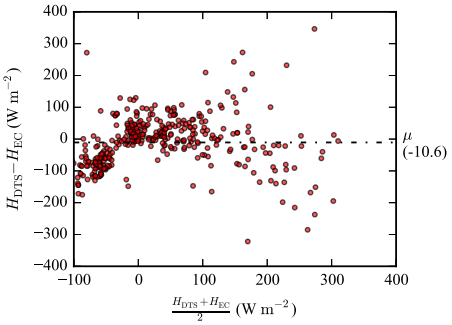

Figure 4.9: Tukey mean-difference plot comparing H_{EC} and H_{DTS}. With μ = −10.6 W m^{-2}, RMSE = 82 W m^{-2}. (15 minute averages). Data from 10, 12-14, 19-22, and 28-30 August 2016.

4

Figure 4.10 shows the time series of the BR-DTS and EC measured heat fluxes. The daytime flux estimates correspond well, and follow the same trends. The night-time BR-DTS estimates of the sensible heat flux are more negative than the EC estimates, one possible reason being the energy balance differences discussed before. On many days, during the early morning and start of the evening, the BR-DTS has missing values, which is mainly due to the inversion of the gradient, as the temperature gradients changes from negative (stable conditions) to positive (unstable conditions) and vice versa. This inversion causes uncertainty, which is filtered out by the quality control flags.

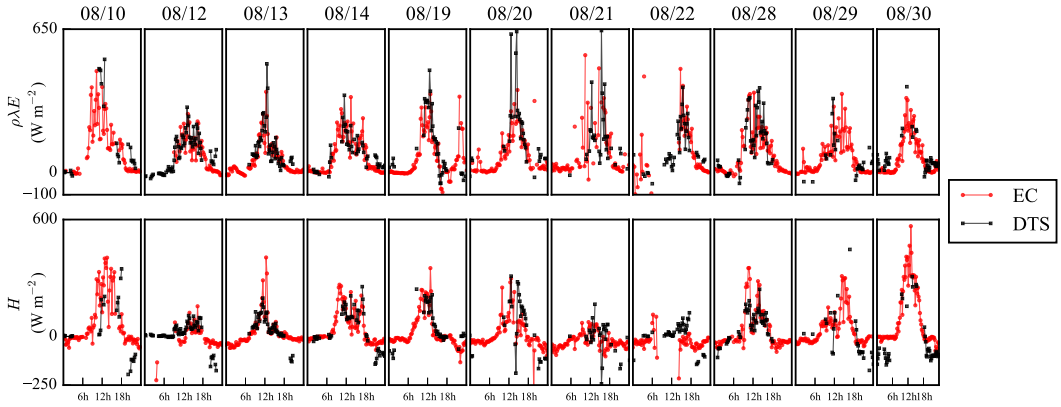

Figure 4.10: Plot comparing the BR-DTS and EC measured sensible (H) and latent ($\rho\lambda E$) heat fluxes over time. (15 minute averages). Data from 10, 12-14, 19-22, and 28-30 August 2016.

4.4 Conclusions and recommendations

This technical note investigates the use of the BR-DTS method above a forest canopy, and introduces a number of improvements on the method as presented by Euser et al. (2014). The performance is investigated by comparing the measured DTS cable temperatures to reference sensors, looking at energy balance closure, and comparing the measured Bowen ratio, sensible heat flux, and latent heat flux to eddy covariance measurements.

When comparing the fiber optic cable temperature to reference sensors, it shows that the wet-bulb and air temperatures can be well represented. Under the canopy, where the cables are shaded from direct sunlight, the DTS cable and reference sensors are in near perfect agreement. However, above the canopy direct sunlight may cause a large error, up to 3 K. This error can be largely mitigated by placing screens to block the sunlight, reducing the error to less than 1 K. Hence screens are effective and should also be placed in the canopy.

The Bowen ratio measured by DTS correlates well with eddy covariance estimates (r^2 = 0.59). A simple quality control method, using the goodness of fit of the vapor pressure gradient, also works well, and filters out most outliers and errors. The small gradients above the forest canopy are hard to measure accurately, which increases the uncertainty during days where fluxes (and thus gradients) are small. The Bowen ratio assumption that the eddy diffusivities of heat and vapor are equal was not studied, but can be a source of differences between the BR-DTS and eddy covariance methods. The difference in fetch for the two methods can also be a cause for differences.

The energy balance closure between the BR-DTS method and eddy covariance is in good agreement, with the mean difference being a 3.4 W m^{-2} underestimation by the BR-DTS method, and an uncertainty of RMSE = 76 W m^{-2}. However, the BR-DTS method estimates a more negative amount of available energy during night-time, and a more positive amount during daytime compared to eddy covariance. One cause could be the lack of biomass heat storage change measurements, which is in the order of 45 W m^{-2}. Another source for the difference is that the energy balance components of the BR-DTS method are generally point measurements, while eddy covariance and the Bowen ratio both have a large fetch. As a result, heterogeneity can cause large differences in the available energy for latent and sensible heat fluxes.

When comparing the latent heat flux of the two methods, they are in agreement, although the uncertainty is high (RMSE = 90 W m^{-2}). The BR-DTS method slightly overestimates the latent heat flux, with a mean difference of 18.7 W m^{-2}. The results for the sensible heat flux are similar, with an uncertainty of RMSE = 82 W m^{-2}, and the BR-DTS method underestimating the sensible heat flux by 10.6 W m^{-2}. However, the underestimation mainly takes place during night-time, which can be caused by differences in available energy.

While the average profiles can be useful and valuable, extra information could be gained by opting for a smaller diameter fiber optic cable, and measuring at a high frequency (1 Hz). This could give new insights into surface interactions and could show convective cells transporting heat upwards.

A way to improve the performance of the BR-DTS method is to find an independent estimate for the sensible heat flux (H), to avoid the uncertainties in the energy balance components (R_N, $\frac{dQ}{dt}$). Through the universal functions of the Monin-Obukhov similarity theory estimates of the sensible heat flux can be made. This could be done either by measuring the wind speed over height (Stricker and Brutsaert, 1978) using DTS (Sayde et al., 2015), or by applying the Flux-Variance method (Katul et al., 1995). The Bowen ratio can then be used to calculate the latent heat flux.

5

A deeper look into the subcanopy

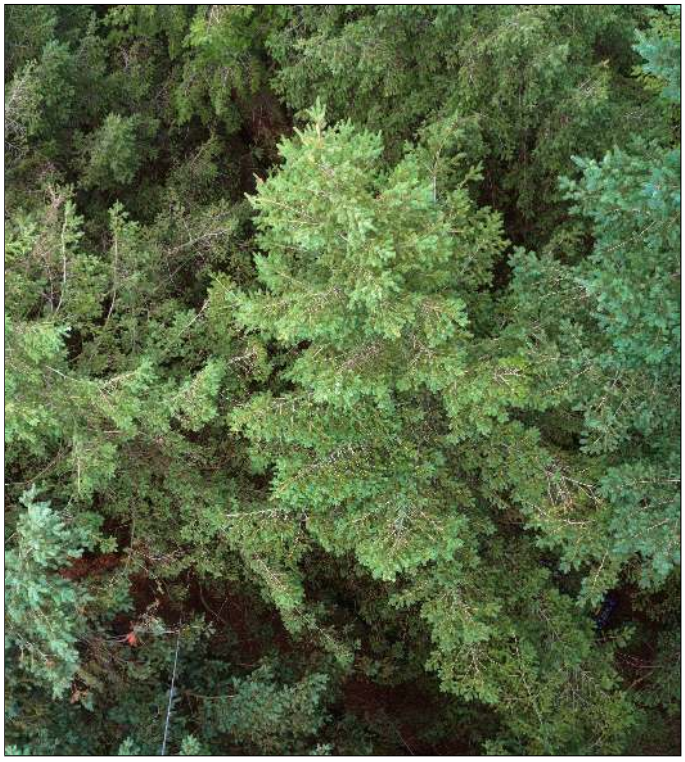

View from above

This chapter is based on:

Bart Schilperoort, Miriam Coenders-Gerrits, César Jiménez-Rodríguez, Christiaan van der Tol, Bas van de Wiel, Hubert Savenije, *Decoupling of a Douglas fir canopy: a look into the subcanopy with continuous vertical temperature profiles*, Biogeosciences **17**, 6426–6439 (2020).

5.1 Introduction

Measuring atmospheric fluxes over complex ecosystems such as forests has always been problematic due to the height of the roughness elements, which typically extends several tens of meters (Wilson, 2002; Barr et al., 1994). The large roughness layer above a tall canopy also makes it difficult to apply many theories of wall flows as well as to apply and validate traditional similarity theory (Katul et al., 1995). As compared to, for example, a thin grass layer, the tall geometry and internal structure of the forest may allow large turbulent structures within the canopy layer, which will interact with the overlying atmospheric flow (Raupach, 1979). This turbulence may either be generated by wind shear from interaction with the canopy geometry, or be generated and suppressed by local buoyancy effects (Baldocchi and Meyers, 1988). When the air near the surface is warmer than ambient air (and thus less dense), convection is generated. Likewise, when the air near the surface is colder, mixing is suppressed due to the density stratification. These local turbulent exchange regimes will greatly influence the exchange rates of energy and matter away from the forest to the higher atmosphere.

Considering energy and gas exchange from the surface to the atmosphere, the different exchange regimes will cause parts of the canopy to be 'coupled' or 'decoupled' from each other and the atmosphere above. When a canopy is coupled to the atmosphere, exchange of heat and gasses such as water vapor and CO_2 takes place between the canopy air and the atmosphere. When a canopy is decoupled from the atmosphere, little turbulent exchange takes place. Different exchange regimes can occur, ranging from a fully decoupled canopy, a partly decoupled canopy, to a fully coupled system where there is turbulent exchange between the subcanopy and the atmosphere (Göckede et al., 2007). These regimes vary per site and are dependent on both the forest structure and the ambient weather conditions.

In particular, nighttime decoupling of the subcanopy is an issue in flux measurements; the so-called 'nighttime (flux) problem' (Aubinet et al., 2012a). This usually occurs when the atmosphere is stably stratified and wind speeds are low (Thomas et al., 2017). If the flow above the canopy is (partly) decoupled from the within canopy flow, above-canopy observations are a poor representative of the overall dynamics (Jocher et al., 2017). This will affect the interpretation of on-site above-canopy flux measurements such as heat, water vapor and CO_2 (Fitzjarrald and Moore, 1990). Especially when determining the net ecosystem exchange of CO_2, decoupling has to be taken into account (Jocher et al., 2017). In cases where the forest floor is sloped, the combination of decoupling and density flows and the subsequent advective transport can play a big role in the transport of heat and gasses (Alekseychik et al., 2013).

In previous studies decoupling has been approached in a number of ways. A commonly used method for flux measurement quality control is the so-called 'u_* filtering' (Goulden et al., 1996; Papale et al., 2006; Barr et al., 2013; Alekseychik et al., 2013). In this method data with low friction velocities (u_*) is flagged to ensure that there is sufficient turbulence for eddy covariance. This means decoupling issues are partially addressed automatically. The threshold for u_* is generally based on the sensitivity of the CO_2 flux to u_*, and can vary in time. Barr et al. (2013) derived a u_* threshold for varying sites and found a stable threshold value for 28 out of 38 tested sites. These site specific stable u_* values are higher than in studies where the threshold varied in time. Ten sites lacked a well defined threshold. Besides the method not being applicable to every study site, u_* filtering also does not take

into account any buoyancy forcing (Jocher et al., 2020). To incorporate this, Bosveld et al. (1999) proposed to use an aerodynamic Richardson number, based on the friction velocity above the canopy, and the temperature difference between forest interior and atmosphere above. However, determining the decoupling threshold requires a highly accurate air temperature profile above the canopy and radiometric surface temperatures of the canopy, which are generally not available.

To address the shortcomings of u_* filtering, methods have been developed that make use of vertical wind speed (w) measured within the canopy. Thomas et al. (2013) introduced a method based on the standard deviation of the vertical wind speed (σ_w) measured both above and in the canopy. When the canopy is fully coupled, the relationship between above and in canopy σ_w is linear. This linear relationship breaks down during decoupling. Jocher et al. (2020) applied telegraphic approximation (TA), the proportion of the data where the directions of w above and below the canopy are aligned (Cava and Katul, 2009). A high value of TA means that the two air masses are well coupled, while low values indicate decoupling. A second method used by Jocher et al. (2020) was the cross-correlation maximum between above and below canopy w, calculated for each flux averaging interval.

With measurements both above the canopy and in the subcanopy, an improved estimation of the fluxes above the canopy is possible (Thomas et al., 2013; Jocher et al., 2018). Hence better knowledge on whether the subcanopy is decoupled or not will increase the accuracy of the interpretation of flux data, and consequently forest behavior. Usually, however, eddy covariance measurements are only available above the canopy.

In the past some high density vertically-distributed measurements have been performed in canopies, namely in a walnut orchard (Patton et al., 2011) and in a very open boreal forest (Launiainen et al., 2007). Several sonic anemometers were distributed along the height of the canopy. However, in both cases the canopies were very open, and decoupling was not an issue at these sites. The main focus of the studies was boundary layer parameterization and profiles of turbulent statistics. Instead of considering discrete point observations along the height of the canopy, we search for a more continuous probing of temperature to get a more detailed view on the influence of static stability on decoupling along the entire height of the canopy.

By using distributed temperature sensing (DTS) technology (Smolen and van der Spek, 2003; Selker et al., 2006), it is possible to measure temperature with a high spatial resolution (30 cm) using a single fiber optic cable. If this cable is placed vertically along a flux tower, a full temperature profile from the forest floor to above the canopy can be measured. As the entire cable is calibrated continuously, it can be used to accurately measure small gradients (Schilperoort et al., 2018; des Tombe et al., 2018; Izett et al., 2019). Additionally, the cable can be installed in a coil configuration to measure at even higher (<1 cm) spatial resolutions (Hilgersom et al., 2016).

The main goals of this chapter are to see how common decoupling is at the Speulderbos site, and to study the influence of shear and buoyancy on decoupling, especially along the height of the canopy. By using high resolution DTS measured temperature profiles we aim to get a more detailed view on decoupling along the entire height of the canopy, the response of the atmosphere-canopy system, and if vertical mixing by turbulence is suppressed or enhanced due to thermal stratification.

5.2 Materials and Methods

5.2.1 Setup

The temperature of fiber optic cables was measured at the Speulderbos forest site (Ch. 2) for 250 days between 2015 and 2018. From the DTS machine a fiber optic cable was routed through a calibration bath, up to the top of a 46 m tall scaffold tower, down along the tower, and back to the calibration bath (Fig. 5.2). The cable was guided by PVC rings secured to horizontal wooden beams. The part of the cable closest to the tower was a wetted cable, for the determination of the wet bulb temperature (not used in this study). The cable further from the tower was used for the air temperature measurements, and was kept at a distance of ~1.2 m away from the tower. To increase the measurement resolution closer to the forest floor a coiled cable was used (Hilgersom et al., 2016). A cable was routed through the calibration bath, over the forest floor to a coil configuration, and then back to the calibration bath. The coil contains 8 m of cable in a coil of 1 m height.

Both cables were 6 mm in diameter, with braided steel wire and a wrapped stainless steel coil around the core, and coated with PVC. The integration time of the DTS device was set to 1 minute, as the response time of the FO cables was up to 5 minutes in air. While the cables have a slow response time, they are robust and able to survive for years without needing replacement. This makes long-term measurement easier than with a less protected (thinner) fast response cable. The FO cables were connected to a Silixa Ultima-S DTS device (Silixa Ltd., Elstree, UK), or to a Silixa XT-DTS from February to March 2018. The FO cables were spliced together and placed in a single ended configuration. To calibrate the cables a calibration bath at ambient temperature with a Pt100 resistance thermometer was used. The water bath was kept well mixed using an aquarium pump. Calibration was performed using the Python package ***'dtscalibration'*** (des Tombe and Schilperoort, 2019; des Tombe et al., 2020).

When measuring air temperature with DTS, direct sunlight will warm up the FO cable, which will therefore deviate from the air temperature. To shield the above canopy section of FO cable from direct sunlight, shade shielding was placed from 38 m to 46 m (Schilperoort et al., 2018). The shielding was not present in the years 2015 and 2018, however a comparison to reference sensors showed that while the daytime gradients were overestimated compared to reference sensors, the absence of shielding did not have a large effect on the measured stability. Below the canopy, direct sunlight rarely reaches the cables.

Beside solar radiation, FO cables are affected by radiative cooling. To estimate the magnitude of the error, we can use the results from Chapter 3. While the environments are different, we assume a similar error because the meteorological conditions (that determine the radiative cooling) are comparable. Under the conditions encountered in the understory, the absolute error will be between 0 and 0.10 K. Errors in the gradient will be up to 0.01 K m^{-1}. All measured temperature gradients were not adjusted or corrected, but left as is.

As the full vertical profile was measured right next to the tower, the tower itself will have an unknown influence on the measurements. The tower itself has a scaffold structure, with a base size of 3.7 by 2.1 m. The scaffold structure is made from 47 mm diameter stainless steel tubes.

At the top of the tower (48 m) an eddy covariance (EC) system was installed, consisting of a Campbell CSAT3 sonic anemometer and a LI-COR Biosciences LI7500 gas analyzer, logged at 20 Hz. The raw data from the eddy covariance system was analyzed using

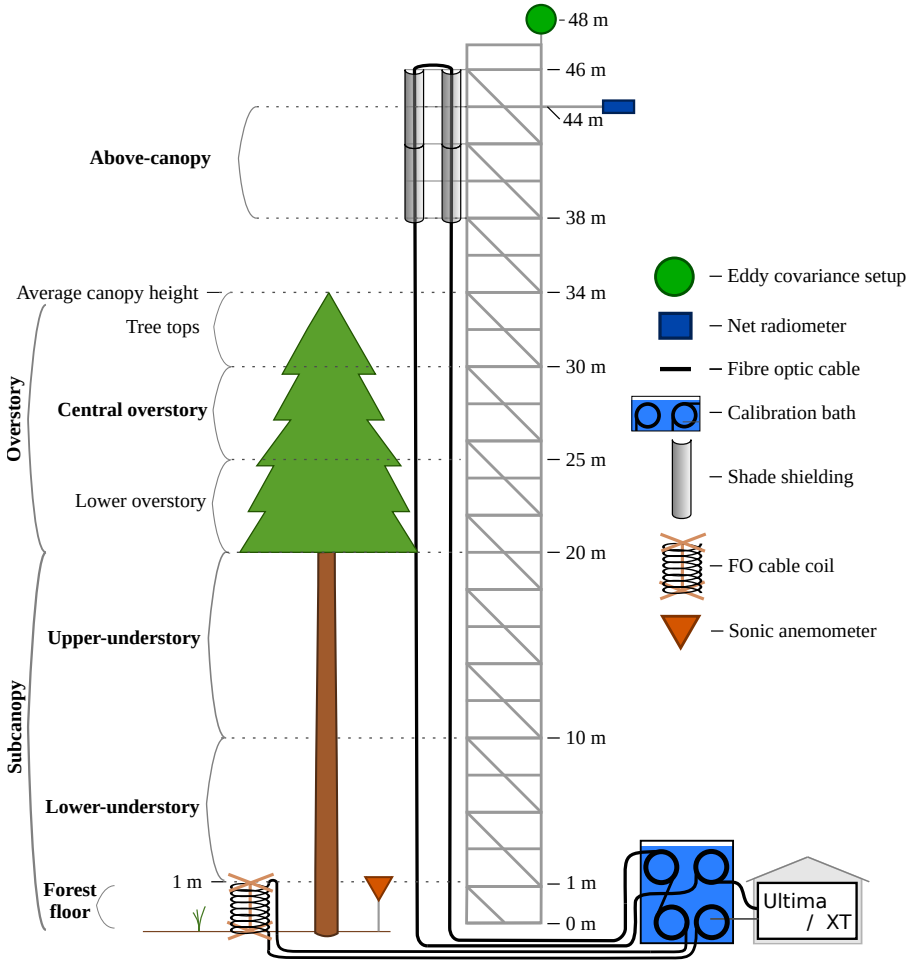

Figure 5.2: Schematic overview of the measurement setup at the tower. On the left the different sections are shown. There is a gap in the sections from 34 to 38 m, as the unshielded DTS data there is not reliable.

LI-COR's EddyPro® software (LI-COR Inc., 2016). The combined quality flag system from Foken et al. (2004) is used. Only the fluxes with a quality flag of 0 or 1 are used in this research. These flags represent fluxes suitable for general analysis, based on steady state tests, integral turbulence characteristics and horizontal orientation of the sonic anemometer. The eddy covariance system was installed on the South West corner of the tower. To account for influences of the tower, all EC data coinciding with a wind direction between 350 and 80 degrees was removed.

At 0.8 m a Gill Instruments Windmaster Pro 1352 sonic anemometer measured 3-dimensional wind speed and sonic temperature, however due to equipment malfunctioning it was only available for a 20 day period in December 2017. This period did not overlap with the DTS or EC equipment. A Kipp & Zonen CNR4 at 44 m measured the incoming

and outgoing short- and longwave radiation. Not all sensors were available for the full measurement period. The DTS measurements were done intermittently, during late summer / early fall in 2015, 2016 and 2017, from January until April 2018 and in June 2018.

5.2.2 Method

To characterize the effect of thermal stratification on turbulent mixing regimes, we calculate the *local static stability* of the potential temperature profile. Static stability of the atmosphere is related to the local temperature gradient. When the temperature gradient is negative, i.e. $\frac{\partial\theta}{\partial z} < 0$, the air closer to the surface is warmer, and natural convection will transport heat upwards. As such it is unstably stratified. When the temperature gradient is positive, the air closer to the surface is colder, no natural convection takes place and turbulent mixing by wind is suppressed. This makes the air stably stratified. When there is no temperature gradient the stability is neutral.

To characterize the *dynamic stability* of the atmosphere, both the effect of thermal stratification and mixing by wind shear have to be taken into account. The ratio of the buoyancy and shear forces can be described using the Richardson number. Following the definition of Bosveld et al. (1999), the aerodynamic Richardson number for decoupling can be calculating using the temperature difference between the air above the forest and the understory:

$$\mathrm{Ri}_A = \frac{gh}{T}\frac{\theta_h - \theta_i}{{u_*}^2} \tag{5.1}$$

where g is the gravitational acceleration (9.81 m s^{-2}), h is the height at the top of the canopy (m), T is the absolute temperature in the subcanopy (K), θ_h is the temperature at the top of the canopy (K), θ_i is the temperature in the subcanopy (K), and u_* is the friction velocity (m $^{-1}$). When $\mathrm{Ri}_A > 1$ buoyancy dominates the flow, when $\mathrm{Ri}_A < 1$ shear dominates the flow. To determine when the canopy would become decoupled, Bosveld et al. (1999) calculated the difference between θ_h and the radiative surface temperature of the canopy, as well as the aerodynamic surface temperature. The aerodynamic surface temperature is derived from extrapolating the roughness-sublayer temperature profile to the height of the canopy. By comparing Ri_A to the difference between the temperature above the canopy and both the radiative surface temperature and the aerodynamic surface temperature, an inflection point was found at $\mathrm{Ri}_A \gtrsim 2$, where the aerodynamic and radiative temperatures diverged and consequently decoupled was assumed.

The friction velocity u_* can be calculated as follows (Stull, 1988):

$$u_* = (\overline{u'w'}^2 + \overline{v'w'}^2)^{\frac{1}{4}} \tag{5.2}$$

where $\overline{u'w'}$ and $\overline{v'w'}$ are the covariance between both horizontal wind speed components and the vertical wind speed component (m s^{-1}).

Also, we utilize the so-called parcel method (Thorpe et al., 1989) in order to estimate the vertical extent that an air package will rise due to natural convection in a steady-state environment. The height to which, e.g., a parcel of air from the forest floor will rise is the height at which the local (potential) temperature $\theta(z)$ exceeds the temperature of the forest floor parcel.

In all analyses we only make use of the dry adiabatic lapse rate. Condensation of moisture can contribute to convection in forests (Jiménez-Rodríguez et al., 2020a), but this effect has not been taken account in this study due to lack of accurate data.

5.2.3 Data Processing

To accurately determine the stability, we need to make use of the entire profile over which we estimate the stability (Schilperoort et al., 2018). To achieve this we fit the data points of each section to a second order polynomial, minimizing the squared error. The temperature gradient is calculated from the profile fit, and consequently, the potential temperature lapse rate is computed (Kaimal and Finnigan, 1994):

$$\frac{\partial \theta}{\partial z} \approx \frac{\partial T_a}{\partial z} + \Gamma \approx \frac{\Delta T_{a,\mathrm{fit}}}{\Delta z} + \Gamma \tag{5.3}$$

where $T_{a,\mathrm{fit}}$ is the fit temperature, and Γ is the dry adiabatic lapse rate (~0.0098 K m^{-1}). The polynomial fits were calculated separately for each section (e.g., lower-understory). The average root-mean-square error of the polynomial fits was ~0.1 K for the main profile, and 0.02 K for the forest floor coil profiles.

To split up the data into the three conditions; stable, (near-)neutral and unstable, we defined the neutral class for a finite interval of gradients between -0.01 and 0.01 K m^{-1} (the same order of magnitude as the lapse rate).

For the calculation of the aerodynamic Richardson number, we used the 10 m DTS temperature as the canopy internal temperature and the 44 m temperature as the top-of-canopy temperature. The 10 m temperature is in the center of the understory, and therefore represents the general temperature of the understory well. It could be possible to use a profile integrated temperature but this will not change the results significantly. Note that the cable at 44 m height is shielded against direct sunlight, in contrast to the cable between 34 and 38 m. The friction velocity measured at 48 m was used.

To split data between daytime and night we have to define these relative to the local time of sunrise and sunset. To account for the uncertainty around dusk and dawn, we define daytime as starting one hour after sunrise and ending one hour before sunset. Nighttime starts one hour after sunset and ends one hour before sunrise. Local sunrise and sunset times for the measurement site were determined using the ***Pysolar*** Python package (Stafford, 2018). We removed all data points both during rainfall and 60 minutes after rainfall (32% of DTS data), to allow for the understory sensors to be fully dry.

5.3 Results

5.3.1 Characteristic temperature profiles

As a demonstration, two typical profiles are shown in Fig. 5.3. 15 October 2017 was a sunny day, causing the overstory to heat up due to solar radiation. In the subcanopy the air stayed cooler, and the profile within the canopy is stable to near-neutrally stratified, with the coldest point at the forest floor. During the night there was strong radiative cooling at both the central overstory and the forest floor. Note that also the forest floor is able to cool through longwave radiation as it partly 'sees' the open sky (Fig. 2.4). This will cause a stable stratification above the canopy and above the forest floor, while the bulk of the

canopy (2 - 26 m) is unstably stratified due to the colder air in the overstory. On 11 October 2017, an overcast and humid day, the canopy was only slightly warmer during the day, and the entire profile was near neutral during the night. Animations of the temperature profiles are available on Zenodo (Schilperoort et al., 2019).

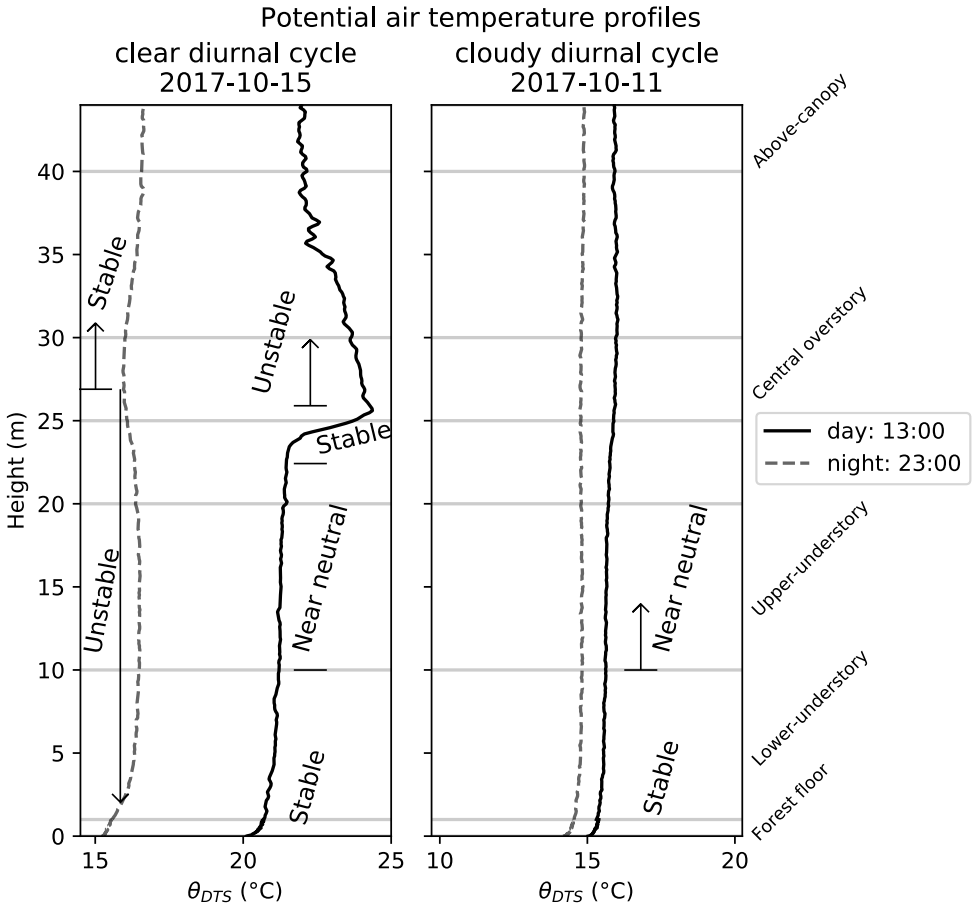

Figure 5.3: Example of potential air temperature ($\theta(z)$) profiles to illustrate the DTS measurements (15 minute average temperature). 15 October 2017 (left) was a sunny day and a clear night. 11 October 2017 (right) was a cloudy day and night. Times are in UTC+1

5.3.2 General climatology: temperature gradient statistics

In order to generalize the features observed in Fig. 5.3, an in-depth statistical analysis of the local gradients in terms of external forcings was made for the full data set. To this end we grouped the DTS gradients in bins of day and night. The bins are split over the four seasons, where winter is from December to February, spring from March to May, summer from June to August, and fall from September to November. For each of these bins, the occurrence of each local stability condition is summed up and compared to the total amount of data

points in the bin. This shows the relative occurrence of stable/neutral/unstable conditions (Fig. 5.4).

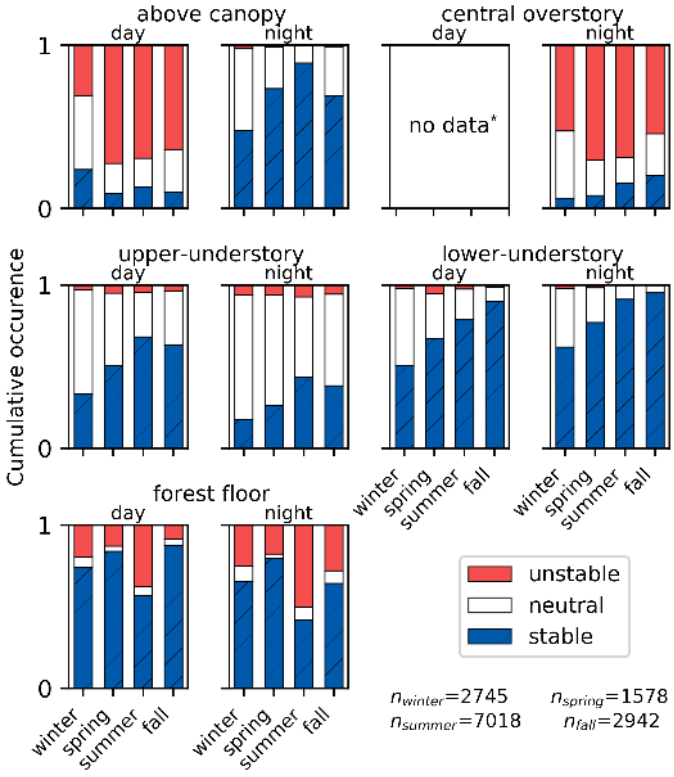

Figure 5.4: Comparison of the local static stability of each cable section (above-canopy, central overstory, upper-understory, lower-understory, forest floor) over time. Y-axis shows the cumulative occurrence of stable/neutral/unstable conditions. Results are split over daytime (left) and nighttime (right), and aggregated over the different seasons. *Central overstory daytime data is not shown due to errors created by solar radiation.

The gradient above the canopy shows the expected diurnal pattern, being mostly unstable during daytime and stable at night. In contrast, the other sections do *not* show this strong diurnal pattern. This discrepancy is an indication that the system in the canopy is often 'decoupled' from the flow above (at least partly), due to the geometry of the vegetation itself, with most of the biomass in the top.

The upper-understory section is mostly stable during daytime and neutral at night. The lower-understory section is nearly always stable, both during daytime and at night. The forest floor section can be both stable and unstable, both during daytime and at night. This may result in persistent mechanical 'blocking' of buoyant air parcels (see below). The unstable gradient at the forest floor section means that convection takes place locally, but due to the stable stratification of the understory this convection would have to travel against the stable gradient in the lower-understory to reach the overstory or atmosphere above the forest. These counter-gradient fluxes are still possible and are likely to occur during

larger sweeps (Denmead and Bradley, 1985), where large scale motions are responsible for transport.

However, the results suggest that the stable conditions in the overstory act as a capping inversion for the buoyancy in the lower understory. The question is, what is the actual vertical extent of the convection driven by surface heating. To study this in more detail we used the parcel method to calculate the maximum height for a floor parcel to rise by convection. Figure 5.5 shows that at night convection from the forest floor rarely exceeds 5 m in height. During the day convective air parcels can rise higher. In 5% of the daytime data they reach 15 m in height, possibly due to sunlight warming up the forest floor. Most likely this occurs at high solar angles during summertime (Fig. 5.4).

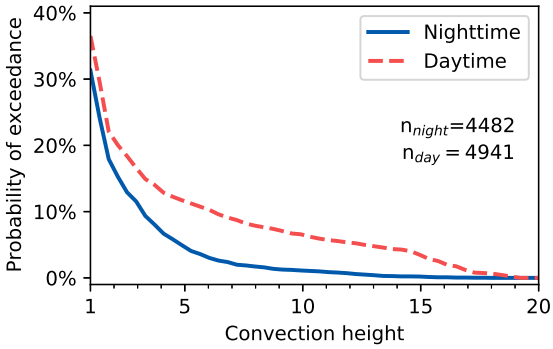

Figure 5.5: Cumulative probability distribution of the convective rising height of a parcel of warm air from forest floor.

From this data it can be expected that there is barely any direct convective transport from the forest floor to the top of the canopy. Also, mixing generated by ambient wind shear over the canopy is largely damped by the thermal stratification of the understory. This may have implications not only for heat transport but also e.g. for the transport of water vapor, CO_2 and trace gases.

5.3.3 Decoupling: the Aerodynamic Richardson number

To characterize decoupling of the understory, both the effects of buoyancy and shear have to be taken into account. To this end we utilize the Richardson number as defined in Eq. (5.1). We restrict ourselves to nighttime cases, which are predominantly influenced by local wind shear above the canopy, and hence by u_*.

A cumulative distribution function of the aerodynamic Richardson number is shown in Fig. 5.6. Only the positive Richardson numbers are shown. However, ~22% of the data points have a negative aerodynamic Richardson number, meaning that the forest interior is warmer than the air above the forest and thus not decoupled. According to Bosveld et al. (1999), decoupling occurs when the aerodynamic Richardson number exceeds approximately 2. In our case this implies that decoupling occurs ~50% of the time at night, showing that decoupling is common at this study site at night.

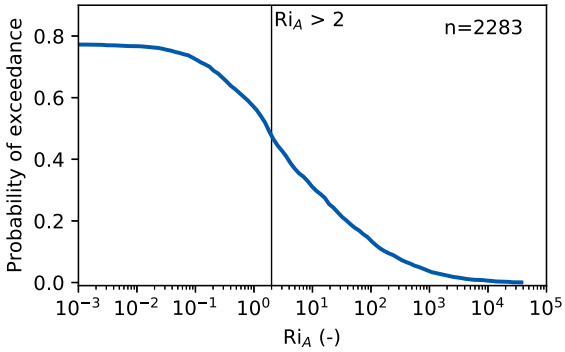

Figure 5.6: Cumulative probability distribution of the aerodynamic Richardson number, for nighttime data. Negative Ri_A values are represented in the maximum of 78% probability of exceedance, i.e., ~22% of the nighttime Ri_A values are negative. Vertical line shows Ri_A = 2, which was defined as the 'decoupling threshold' in Bosveld et al. (1999).

The aerodynamic Richardson number was derived by Bosveld et al. (1999) for nighttime conditions, and is not valid under daytime conditions where the friction velocity will be strongly affected by turbulence generated by convection from the top of the canopy. The suppression of mixing by the stable stratification of the understory during daytime is also not taken into account in the aerodynamic Richardson number.

5.3.4 Influence of shear and buoyancy on decoupling

Magnitude of the temperature difference between the subcanopy and atmosphere

While wind shear over the canopy will induce mixing, a temperature difference between the atmosphere can either suppress or drive mixing. To study the buoyancy forcing, we compare the temperatures at 44, 10 and 2 m height (Fig. 5.7). In ~78% of the available data the middle of the understory was colder than the air above, despite the proximity to the biomass and soil. This was previously observed at this site by Bosveld et al. (1999). Closer to the ground, at two meters height, the air was generally even colder. During the day, the understory was nearly always colder (~99% of the available data). This was to be expected as most incoming sunlight is absorbed at the top of the canopy, heating up the atmosphere above as well, while the understory stays cool.

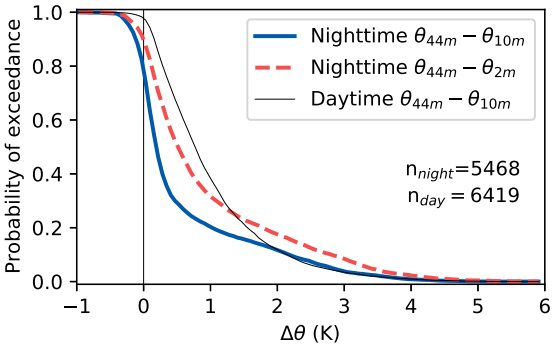

Figure 5.7: Cumulative probability distribution of the difference in temperature between the forest interior and the air above the forest (at 44 m). Solid line shows the nighttime distribution for 10 m, dashed line shows the nighttime difference for 2 m, thin line shows the daytime difference at 10 m. Positive numbers denote a colder forest interior.

5

The relationship between the ambient friction velocity and the local static stability

While stable thermal stratification can suppress mixing, wind shear at the top of the canopy will enhance mixing. Therefore we compare the above canopy friction velocity with the in-situ observed temperature gradient at several heights (Fig. 5.8). To relate the u_*-temperature gradient relationship to decoupling, the aerodynamic Richardson number is shown by coloring the plot markers.

At night the gradient above the canopy is inversely related to u_*, as expected (Fig. 5.8a). At high shear conditions the air above the canopy is well mixed, resulting in small temperature gradients and a coupled canopy. At low shear conditions it is possible for the top of the canopy to cool considerably, allowing strong local gradients to occur.

Interestingly, the understory gradients (Fig. 5.8b, c) show a characteristic L-shaped behavior with a kind of threshold value for u_*: below $u_* \approx 0.4$ large gradients are able to occur, while small gradients are observed for large u_*. This threshold value is in line with the u_* values associated with decoupling of evergreen needleleaf forests found by Barr et al. (2013), although the u_*. threshold is strongly site specific, and it is not always possible to derive a u_*. threshold. Especially the upper-understory gradient shows a distinct split between the two coupling regimes; when the canopy is coupled ($Ri_A < 2$), the local gradient is grouped tightly around 0. When the canopy is decoupled, strong gradients can form, with u_* values ranging between 0 and 0.4 m s^{-1}.

The relationship between u_* and the forest floor gradient is less clear (Fig. 5.8d), however the Richardson number highlights the positive correlation: the forest floor is unstably stratified when u_* is low and the canopy is decoupled, and stably stratified when u_* is high and the canopy is coupled. The relationships between the understory gradients and friction velocity show that the temperature gradients can serve as a proxy for decoupling; when the understory is strongly stably stratified the canopy is decoupled. However, the understory can still be decoupled even without strong thermal stratification, as shown by the data points in the lower left corners of Fig.5.8b, c. When the friction velocity is below ~0.2 m s^{-1}, the canopy is always decoupled. It is likely that at very low friction velocities

the wind will not be able to mix the canopy even though there is no strong temperature gradient (e.g., very low wind, overcast conditions).

While at night turbulent mixing is driven by wind shear (hence friction velocity), during daytime convection generated at the top of the canopy is also important for creating turbulence. Indeed, as shown in Fig. 5.8e, f, g, and h, the dependence of local temperature gradients on (externally driven) u_* is less well defined and sometime even absent. Unlike the nighttime data, the lower- and upper-understory gradients have no clear threshold or correlation at all.

5.3.5 Discussion

The results show that the subcanopy is nearly always stably stratified, both during the day and at night, and will primarily be decoupled during low-wind conditions. The gradient above the forest floor may become unstably stratified, but convection does not rise high enough to penetrate the overstory. The understory shows consistent decoupling and seems to act like a kind of mechanically 'blocking layer' between the forest floor and overstory. In the overstory, nighttime convection is common. Heat stored in the leaves, branches, and trunks warms up the air in the lower overstory, causing within-canopy convection.

This results in four typical exchange regimes observed at the Speulderbos, schematically illustrated in Fig. 5.9. Two daytime (a and b), and two night-time (c and d) situations. Fig 5.9a displays the daytime high wind shear regime. The wind is strong enough to penetrate into the subcanopy and mix the entire canopy. In Fig 5.9b wind shear is not strong enough, and the subcanopy is decoupled. Convection can take place above the forest floor but does not progress further upward into the canopy.

At night, exchange between both the subcanopy and top of the canopy, and the atmosphere is dominated by wind shear. In Fig. 5.9c wind shear is strong enough to mix the entire canopy and prevent strong stable stratification. Local convection can take place within the canopy due to heat released by the leaves, branches and trunks. Fig. 5.9d the wind is not strong enough to enter the subcanopy, and the subcanopy is stably stratified. Convection from the forest floor is possible, but does not reach the overstory. For nighttime, the subcanopy is decoupled in approximately 50% of the available data. Convection above the forest floor takes place in ~50% of the low wind shear conditions. To determine if the subcanopy is fully coupled requires local measurements, either of a temperature profile or of turbulence.

As explained, wind shear above the canopy has a large influence on the thermal stratification of the canopy. We observe strong stratification at night when u_* is below 0.4 m s^{-1}, which is in line with previous research (Barr et al., 2013; Papale et al., 2006). It is important to note that this is not necessarily a fixed threshold, but that some form of hysteresis might be present (van de Wiel et al., 2017). When the subcanopy is already strongly thermally stratified, more wind shear is needed to mix it, while a canopy which is not stratified will stay mixed more easily. It would be interesting to explore the impact of understory stratification on the friction velocity threshold value, by assessing effects of conditional sampling.

We note that effects of heterogeneity and advection may also play a role in the convective coupling between the forest floor and the overstory. Localized transport (consisting of convective plumes (Jiménez-Rodríguez et al., 2020a)) could transport heat from the forest

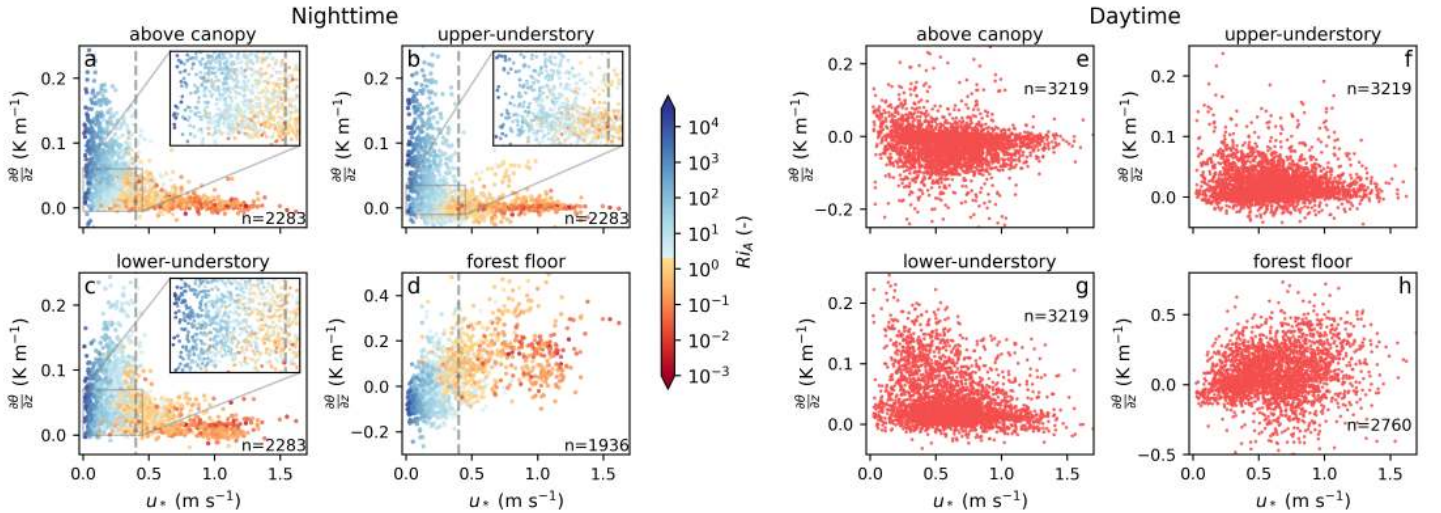

Figure 5.8: Comparison between the friction velocity at 48 m, and the DTS measured temperature gradients. For the nighttime data the markers are colored by the aerodynamic Richardson number, where values of Ri_A < 2 (coupled) are colored red, and values of Ri_A > 2 (decoupled) are colored blue. The gray vertical dashed line indicates u_* = 0.4. Subplot a & e show the above canopy gradient, b & f the upper understory, c & g the lower-understory, and d & h the forest floor gradients.

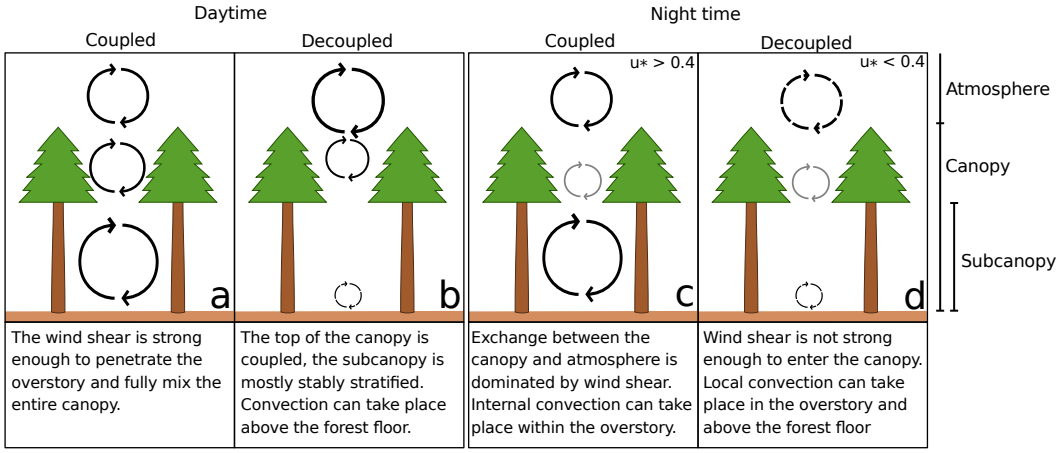

Figure 5.9: Typical exchange regimes observed at the Speulderbos site. The cyclic arrows denote convection/non-local transport.

floor through the canopy. As this transport is very local, the measured 15-minute mean vertical profile might not be representative for the entire forest. Among others, Alekseychik et al. (2013) proved that drainage flows, where dense cold air flows down slope, can be of influence for decoupling. This could be an important mechanism at this site as well, as the slope of the forest floor is non-negligible; approximately 2.5%. Due to the open understory, advection in the subcanopy could be an important process, with wind speeds ranging from 0.5 to 2 m s^{-1}, and gusts of up to 4 m s^{-1}. While it is possible to asses advection and drainage flows if a sonic anemometer is located near the forest floor (Staebler and Fitzjarrald, 2004; Jocher et al., 2017), we did not study this further due to a lack of sonic anemometer data.

Another limitation of this study is the low measurement frequency (which is limited by the response speed of the fiber optic cables). Any exchange mechanisms that have a timescale under 10 to 15 minutes, such as sweeps or ejections (Gao et al., 1989), will be missed.

5.4 Conclusions and recommendations

Due to the tall vertical structure of forests, parts of the canopy can be turbulently decoupled from the overlying atmosphere. If this decoupling is not properly taken into account in above-canopy flux measurements, it can lead to incorrect estimates of gas fluxes, in turn reducing the accuracy of estimates of the net ecosystem exchange of CO_2, or evaporation (Fitzjarrald and Moore, 1990; Alekseychik et al., 2013; Jocher et al., 2017).

In this chapter we used vertical DTS profiles to study the thermal stratification and the potential of decoupling within the forest canopy. We found that on the Speulderbos measurement site stable stratification of the subcanopy is the dominant state over multiple years and seasons, even though convection can take place just above the forest floor both at night and during the day. The local convection above the forest floor rarely exceeded 5 m height at night, and 15 m during the day, and did not reach the overstory.

Local temperature gradients in the understory were nearly always stable, and showed no strong diurnal pattern. The temperature gradient above the forest floor was stable ~70% of the time, and did not show a strong diurnal pattern either. Besides the stable temperature gradients, dynamic stability indicators such as the aerodynamic Richardson number also indicated decoupling of the understory, up to 50% of the time at night. The air temperature of the subcanopy was mostly colder than the air above the forest, at night (~78%) and especially during the day (~99%). When comparing the temperature gradients to the friction velocity, we found that at night decoupling could occur when $u_* < 0.4$ m s^{-1}.

Although it is not possible to determine decoupling with DTS temperature profiles alone, with the DTS temperature profiles we were able to study the canopy-atmosphere interaction in detail. However due to the fiber optic cables not being shielded or actively ventilated some uncertainty remains in the measured temperatures and gradients. This prevents conclusive interpretation in cases when temperature differences are small. A second shortcoming is the limited time resolution of the cables, which means that fast processes could not be studied. In the next chapter we use a thinner fiber for a fast thermal response to show more detail and unveil other processes which are not visible in the data discussed in this chapter. Finally, the current optical fiber technique may also be employed in a actively 'heated' form. In this 'hotwire modus' high resolution observation of wind speed is possible, as explained in Sayde et al. (2015), van Ramshorst et al. (2019), and Lapo et al. (2020). Such data would be complementary to the present study, and would give more insights into the wind shear and dynamic stability throughout the entire canopy. This could aid in studying canopy-atmosphere interaction at forest sites, and would allow determining decoupling along the full height of the canopy. In turn this will increase the knowledge on the general drivers of decoupling in forests, to improve the representativeness of flux measurements above forests.

6

Nighttime inversions within the canopy

(Artificial) fog flowing through the forest at the Speulderbos measurement site

Parts of this chapter are based on:

Bart Schilperoort, Miriam Coenders-Gerrits, César Jiménez-Rodríguez, Antoon van Hooft, Bas van de Wiel, Hubert Savenije, *Detecting nighttime inversions in the interior of a Douglas fir canopy*, Agriculture and Forest Meteorology, *under review* (2021).

6.1 Introduction

Forests cover a large area of the earth's land surface and form important components of both the water and the carbon cycle. However, due to their intrinsic height scale and complexity, measuring their contribution to these cycles has remained very challenging (Wilson, 2002; Barr et al., 1994). In particular during nighttime, when fluxes are modest in magnitude, measuring exchange of carbon dioxide, water vapor, and heat between the forest canopy and atmosphere is difficult.

During the day, strong convection will ensure strong mixing of air which enables frequent exchange of air masses between the forest and the atmosphere above. Likewise, high wind conditions favor such exchange. In contrast, during low wind and clear-sky nights current models and theories fail, as non-turbulent flows and spatial heterogeneity becomes more dominant (Katul et al., 1995). An issue affecting nighttime measurements specifically in forests is decoupling; a lack of turbulent exchange between the canopy and the atmosphere (Aubinet et al., 2012a). This lack of turbulent exchange makes experimental quantification of water, carbon, and energy fluxes above forests difficult, as measurements above the canopy are not representative for what is happening inside the canopy (Jocher et al., 2017). Decoupling is caused by the lack of generation of turbulence due to the absence of sufficient wind shear, and also due to the suppression of turbulence by stable stratification; when the canopy, or parts of it, are colder than the atmosphere above (Baldocchi and Meyers, 1988; Thomas et al., 2017; Schilperoort et al., 2020). If not taken into account, decoupling will affect the interpretation of forest fluxes such as water and CO_2 (Fitzjarrald and Moore, 1990; Alekseychik et al., 2013).

There are different (proxy) methods to assess whether the canopy is in a decoupled state or not. So-called u_* (friction velocity) filtering is often used to filter flux data for periods with low wind shear (Goulden et al., 1996; Papale et al., 2006; Barr et al., 2013). Other methods use the relationship between the standard deviation of vertical wind speed (σ_w), both above and below the canopy (Thomas et al., 2013), or look at (cross-)correlation between the measurements of vertical wind speeds (Cava and Katul, 2009; Jocher et al., 2020). However, the above methods are only proxies for the momentum exchange, and do not actually detect the density stratification over the full canopy-atmosphere continuum. By detecting such stratification one could assess whether indeed temperatures vary smoothly with height or that 'separated' or 'decoupled' layers are being formed.

Besides it has to be realized that decoupling is not a binary state. A range of different exchange regimes can occur, from a fully coupled canopy, to a decoupled subcanopy, to lastly a fully decoupled canopy (Göckede et al., 2007). Strong temperature inversions, where air lower down is colder and thus denser than air above, within or over the canopy, can both affect as well as be the result of the decoupling. By knowing if such an inversion exists, and at which height it is, the degree of coupling of a canopy can be studied in much more detail. In this study therefore, we present high-resolution (~0.3 m) observations of in-canopy temperature using the so-called DTS technique.

Distributed Temperature Sensing (DTS) is a measurement technique that has found increasing use in atmospheric measurements, for measuring air temperature (Thomas et al., 2012; Zeeman et al., 2015; Izett et al., 2019; Peltola et al., 2020) as well as wind speed profiles (van Ramshorst et al., 2019; Lapo et al., 2020). DTS measurements are made by shining a laser down a fiber optic (FO) cable, and analyzing the Raman backscatter signal. As this

Raman backscatter is only sensitive to temperature, the temperature along the entire FO cable can be monitored continuous in space (Smolen and van der Spek, 2003; Hartog, 2017). This is akin to having a long string of standard temperature sensors. In a previous study by Schilperoort et al. (2020) decoupling was investigated in a Douglas fir canopy with the use of a DTS measured vertical temperature profile. It was hypothesized that a 'blocking layer' existed within the understory, which reduces the turbulent exchange between the forest floor and the rest of the canopy. A drawback in their data analysis was that the data had high spatial resolution (30 cm) but that it was limited in its temporal resolution. This was due to the type of FO cables used: thick cables which respond slowly to changes in air temperature. To expand on this study, an adjusted measurement setup was placed on the site, which is capable to detect air temperature variations at a high frequency (~0.5 Hz). This enables us to make more definitive conclusions about the nature of the blocking layer and to detect dynamical features such as internal gravity waves.

Using these high frequency air temperature profiles, we will look at the presence of temperature inversions within the Douglas Fir canopy. We will study their formation and distribution within the canopy, and look at inversion dynamics at different scales. Next we will discuss the reasons why these inversions within the canopy can often elude detection, i.e., why they are not observed more often using more traditional point sensors. Finally, to explain why and under which conditions the inversions form, we present a simple 1-D conceptual model to support our hypothesis on the mechanism behind the layer formation within the canopy.

6.2 Materials and Methods

6.2.1 Setup

To measure a vertical profile of air temperature, a thin fiber optic (FO) cable was placed vertically at the Speulderbos site, from the forest floor up to 32 meters (Fig. 6.2) along a 48 m tall measurement tower. The 'j-BendAble Robust' OM3 fiber (j-fiber GmbH, Jena, Germany) had a translucent acrylic coating, and a diameter of 500µm. The FO cable was not extended beyond 32 meters due to the fragility of the thin cable. To hold it in place, it was connected to horizontal wooden beams which were extended from the measurement tower. The beams were placed every 4 meters, starting at the surface, increasing to every 2 meters from 26 m upward. The thin fiber was spliced to two different FO cables on both ends, which were routed down the tower, through the calibration baths and connected in a double-ended configuration to the DTS machine (van de Giesen et al., 2012). The thin-fiber temperature profile was measured from 21 August 2019 until 17 October 2019, when the FO cable broke.

The DTS machine used was a 2 km range Ultima-S device (Silixa Ltd., UK). The measurement period was configured to 1 second per channel. This results in a double-ended calibrated temperature with an increased measurement period of ~2.3 s due to processing overhead. The raw data was calibrated using the python package 'dtscalibration' (des Tombe and Schilperoort, 2019).

The data was calibrated in a double-ended configuration, using a well-mixed bath at ambient temperature and a different bath maintained at 30 degrees Celsius. As the calibration was performed over splices, this could result in an offset and bias in the final

temperatures (des Tombe et al., 2020). However, to detect strong temperature inversions we are mostly interested in the variations over air temperature over time and height, so a possible small bias in the absolute temperature is acceptable. DTS measurements suffer from inherent uncertainty in the measurements. With our Ultima-S device the expected measurement noise at the highest resolution has a standard deviation of $\sigma_{\mathrm{DTS}} \approx 0.24$ K. By averaging in space and time this uncertainty can be reduced.

At the top of the measurement tower, at 48 m, an eddy covariance setup was placed consisting of a CSAT3 sonic anemometer (Campbell Sci., USA) and a LI7500 gas analyzer (LI-COR Biosciences, USA), both logged at 20 Hz. At 44 m a CNR4 Net Radiometer (Kipp & Zonen, the Netherlands) was placed, logging at 1 minute averages. On the forest floor, at ~0.8 m, a Young-81000 sonic anemometer (R.M. Young, USA) was placed, which was logged at 32 Hz. As this sonic anemometer did not have active heating, condensation on the transducers caused measurement disturbances on some nights. At 2 m another CNR4 Net Radiometer was set up, logging at 1 minute averages. All dates and times are in UTC.

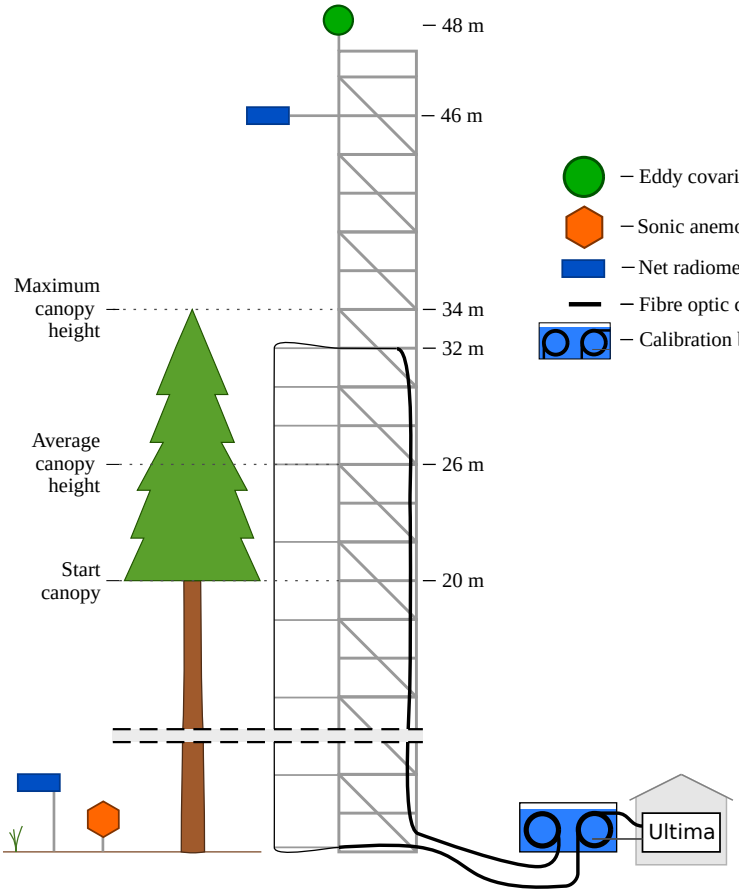

Figure 6.2: Schematic overview of the measurement setup at the tower.

6.2.2 Method

To be able to properly detect inversions within the DTS-measured temperature profiles we corrected all temperature values for the dry adiabatic lapse rate, so as to get the potential temperature θ (K, in reference to the ground level), hereafter just referred to as temperature.

Preliminary inspection of temperatures learned that sharp inversion commonly occurred within the canopy. These inversions are characterized by a temperature jump of 1 - 2 K over a very small distance (< 0.3 m). For a general analysis we need a method to automatically detect the presence and features of these sharp inversions, such as the height at which the inversion is centered on (z_{inv}, m), and the strength (i.e., temperature jump) of the inversion ($\Delta\theta_{\mathrm{inv}}$, K).

However, DTS measurements with high-frequency results in rather high measurement uncertainty, because statistical convergence decreases with decreasing averaging time. Uncertainty in the temperature will lead to difficulties in detecting inversions, when the signal ($\Delta\theta_{\mathrm{inv}}$) to noise ratio is too small. To solve this, we used cross-correlation to detect step changes in the temperature profile. In the cross-correlation method, a sliding dot product is calculated between the vertical temperature profile and a step function (i.e., the sign/signum function):

$$\begin{aligned} \mathrm{sgn}(n) &:= \begin{cases} -1, & \text{if } n < 0, \\ 0, & \text{if } n = 0, \\ 1, & \text{if } n > 0. \end{cases} \\ \text{for } n &= \left[-\frac{N}{2}, \frac{N}{2} \right] \end{aligned} \tag{6.1}$$

where N is the window size ($\mathbb{R}$) of the step function. The inversion height is determined to be at the height of the maximum value of the cross-correlation (Fig. 6.3). The cross-

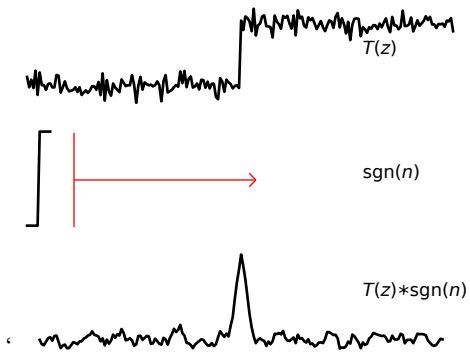

Figure 6.3: Example of the convolution of a synthetic temperature profile ($T(z)$, with white noise) and the sign function, and the resulting cross-correlation. The detected height of the inversion is at the maximum value of the cross-correlation.

correlation method was tested on synthetic data. This showed that we could reliably detect sharp inversion layers down to a minimum strength of $\Delta\theta_{\mathrm{min}} \approx 0.34$ K, if a window size of 32 datapoints was used (corresponding to a physical filter window of 4 m).

After the height of a possible inversion is detected using the cross-correlation method, the temperature difference over the inversion can be determined. To do this, we calculate the difference between the temperature above (θ_{above}) and below (θ_{below}) the inversion height. To reduce the measurement uncertainty, we take the mean temperature in a range from 0.5 to 1.5 meters distance from the detected inversion height. The specific range is a compromise between reducing the uncertainty and how representative the data points are of the inversion strength.

$$\theta_{\text{above}} = \int_{z_{\text{inv}+0.5}}^{z_{\text{inv}+1.5}} \frac{\theta(z)}{\Delta z} \mathrm{d}z, \qquad \theta_{\text{below}} = \int_{z_{\text{inv}-1.5}}^{z_{\text{inv}-0.5}} \frac{\theta(z)}{\Delta z} \mathrm{d}z \tag{6.2}$$

where $\Delta z = 1$ m. The temperature difference over the inversion can then be calculated with;

$$\Delta\theta_{\text{inv}} = \theta_{\text{above}} - \theta_{\text{below}} \tag{6.3}$$

Lastly, we preformed a data screening. As the dataset is limited in time, a visual analysis of the temperature data can be performed to find events where, e.g., a sudden breakup of a strong inversion occurs, these events can then be studied in detail. In a preliminary look at the data, wave-like motions were clearly visible in the inversion height. These motions were visible in both the micro scale, as well as the submeso scale. We will analyze these events to describe their properties and discern their source.

6

6.3 Results and Discussion

6.3.1 Example inversion

As an illustration, Figure 6.4 shows the potential temperature over height and time, as measured with DTS. The inversion height that was detected using the cross-correlation method is displayed over the temperature plot with a red line. During the night, the temperature along the entire profile falls gradually by about 2 K, both above and below the inversion layer. The local inversion has a strength of ~2 K, and varies a in height from 5 to 20 meters. Besides the larger changes in height, the inversion shows regular smaller oscillations of about 2 m at timescale of 1 – 2 minutes.

6.3.2 Inversion statistics

Out of a total of 58 observed nights, persistent inversions (present for more than half of the night) were observed in 14 nights (24%). Eleven nights (19%) had some intermittent inversions, and the remaining 33 nights (57%) had no inversions within the canopy. These statistics indicate that the formation of inversion layers is a regular phenomenon, rather than an occasional event. The inversions were mostly present from 21 August 2019 to 23 September 2019, a period characterized by clear nights and low friction velocities (Fig. 6.5). During the last three weeks of the measurement period wind above the canopy was more turbulent and the sky was cloudy. Consequently, no inversions were detected during this period.

Due to the mechanics of its formation and evolution, the inversion layer will be constrained by canopy morphology (e.g., the Plant Area Index). Figure 6.6 shows the distribution of the inversion layer over height, for two different inversion strengths. The stronger inversions are most likely to occur between ~10 – 20 meters. Inversions were also regularly

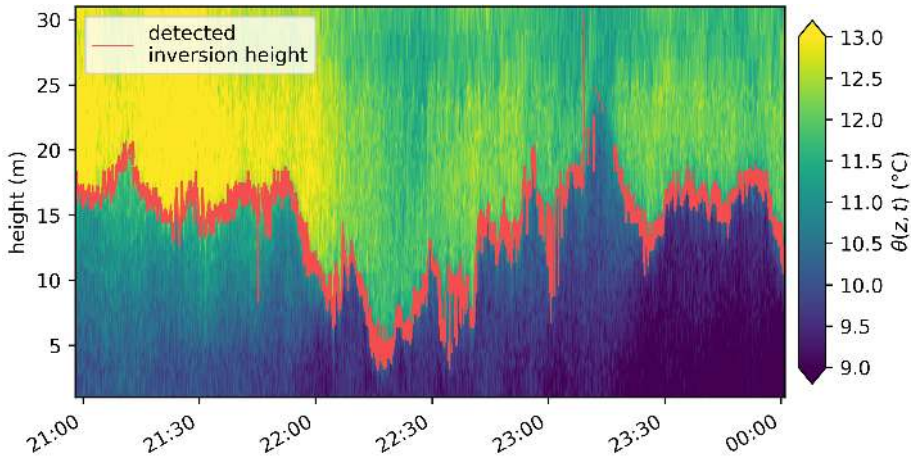

Figure 6.4: Example of DTS measured potential temperature profile in time, along with the detected inversion height (where $\Delta\theta_{\text{inv}} > 1\text{K}$). Data of 14 September 2019. The 2D temperature plot has been smoothed using a Gaussian filter in time and space.

detected just above the forest floor (0 – 5 m) and near the canopy top (28 – 30 m). Within the overstory inversions are rare. It is likely that the dense branches reduce turbulent mixing so that any inversion would quickly rise in height to the top of the canopy.

A reason for the preferential height could be that shear-driven mixing is enhanced both near the forest floor and just above and below the dense part of the canopy (at 20 – 26 m height). This enhanced shear results from the interaction between the wind and rigid (no-slip) surfaces such as the ground and the tree biomass at the top. This could result in a local minimum of the diffusivity between the forest floor and canopy. With the right conditions (i.e., the strength of the overall bulk inversion) this local minimum can exhibit a self-reinforcing effect, where the low diffusivity allows for a local sharpening of the temperature gradient, which in turn lowers the local turbulent diffusion. We analyzed the essence of this positive feedback, by a simple 1-D conceptual model in Section 6.4.

Formation of inversions

To study what could drive the formation of the inversions, the strength of the inversion is compared to the friction velocity and the net radiation, both above and below the canopy (Fig. 6.7). It is that likely these play a role, as a low friction velocity would allow the formation of a stable stratification due to a lack of mixing, and a strong net radiative cooling would allow for large temperature differences.

As expected, the friction velocity above the canopy has to be low for a strong inversion to form or persist (Fig. 6.7a). The friction velocity below the canopy (Fig. 6.7c) shows an even stronger relationship, but causality can not be derived from this as the presence of a strong inversion would cause a very low u_* value at 1 m height as well. The net radiation above the canopy also needs to be highly negative (Fig. 6.7b); meaning clear sky conditions with strong radiative cooling. However, interestingly, the net radiation below the canopy shows no clear relationship with the strength of the inversion (Fig. 6.7d).

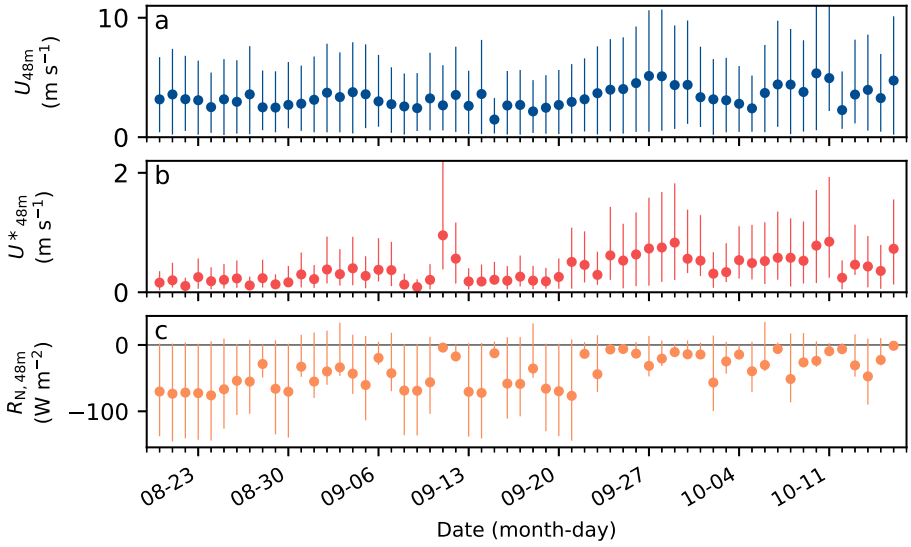

Figure 6.5: Nighttime conditions during the measurement period of the wind speed at 48 meters (**a**), average friction velocity at 48 meters (**b**), and net radiation (**c**). The round markers denote the mean nighttime values, and the error bars the 25th and 75th percentiles.

This lack of correlation between the inversion strength and the net radiation in the understory could mean that the source of the cold air under the inversion is not the cold forest floor. The cold air has to be supplied somehow however, either in the form of cold air plumes falling down from the top of the canopy (Dupont and Patton, 2012), or a different non-local source of cold air (i.e. advection). It could also be that the net radiometer in the understory is located in a warm spot with less exposure to the open sky, and is therefore not fully representative of the whole understory.

Double inversions

On some occasions a double inversion was visible in the measured temperature profiles. An example of this is shown in Figure 6.8. There are two clear temperature jumps visible in Fig. 6.8a, first at 14 m, and a second at 26 m. Both temperature jumps are ~1 K in magnitude. As can be seen in Fig. 6.8b, the inversions are not static in height, but *oscillate* with a period of about 80 seconds and an amplitude of 3 m. The two inversions seem to move in-phase, although small phase differences are small difficult to detect with the limited measurement frequency and the high measurement uncertainty. Due to the oscillations the top inversion dips in and out of view periodically; only when the inversion is below 32 meters it is measured. Therefore the inversion at the top of the canopy could be very common, but remains undetected by the current DTS setup.

6.3.3 Wave-like motions of the inversion

On multiple days strong wave-like motions are visible in the inversion within the canopy. The motions have amplitudes between 2 and 10 meters, and a well-defined period of 50 –

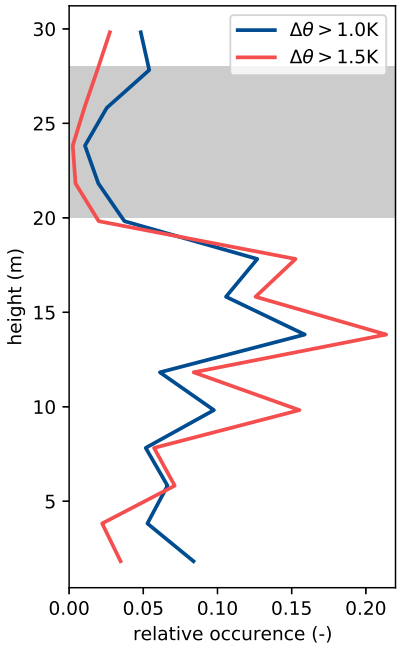

Figure 6.6: Height at which inversions were detected, with two thresholds of minimum temperature differences; 1.0 K (red), and 1.5 K (blue). The gray shaded area shows the most dense part of the canopy.

100 seconds. These motions are already visible in Figure 6.8, both in the inversion at 15 meters, as well as the second inversion when it dips down to 30 meters. While the DTS measurement noise makes it difficult to study the wave-like motions in detail, the motions are very clearly visible in the sonic anemometer data from the top of the measurement tower.

Wave-like motions with similar amplitudes and periods are frequently observed in atmospheric stably stratified layers of all kind. Recently, fascinating Kelvin-Helmholtz billows have been reported by e.g., echo sodargrams at Dome C in Antarctica (Petenko et al., 2019), where the homogeneous terrain and steady meteorological conditions allows detailed studies of the mechanics of the stable boundary layer. During the 'CHATS' experiment in a walnut orchard (Dupont and Patton, 2012) wave-like motions were visible during stable conditions as well, and were described as Kelvin-Helmholtz type structures. Kelvin-Helmholtz structures are formed due to shear stress between two layers of different densities. The discontinuity of temperature over those layers typically coincides with a discontinuity in wind speed, or rather an occurrence of velocity inflections points. Flows with such inflection points are known to be hydrodynamically unstable (van der Linden et al., 2020; Kundu et al., 2016; Banta et al., 2007). Shear instabilities may quickly amplify and growing waves may become unstable and break (mixing events). Figure 6.9 shows a wave-like event on 22 August, where the absolute value of vertical wind speed at 48 m (Fig. 6.9b) was

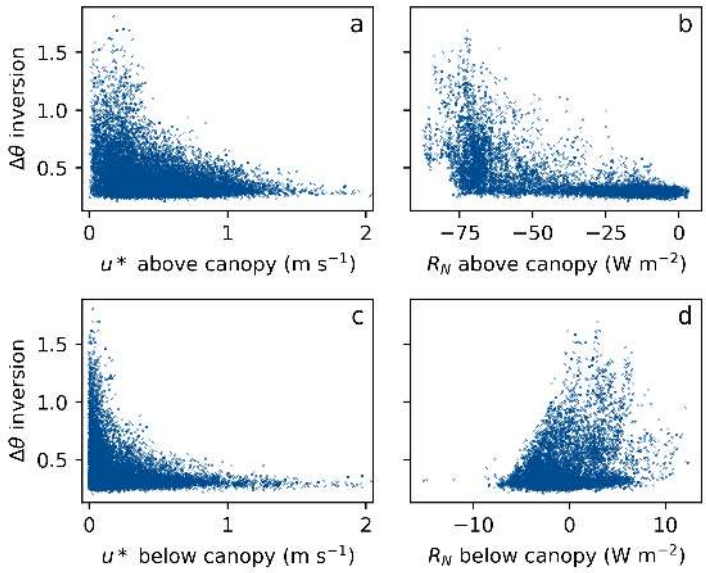

Figure 6.7: Scatter plots of the nighttime friction velocity (**a**, **c**) or net radiation (**b**, **d**), and the inversion strength. Both above (**a**, **b**) and below the canopy (**c**, **d**).

initially both small and steady, until, until an oscillating motion began. The amplification of this oscillation is clearly visible in the sonic temperature (Fig. 6.9c). However, after a few oscillations the vertical wind speed becomes more noisy, and the friction velocity increases (Fig. 6.9a). During this period of increased turbulence the air in the overstory (20 – 30 m height) increases by over 1 K in less than 10 minutes (Fig. 6.9d). This wave activity is generated not within the canopy but rather in the atmospheric boundary layer itself. It is possible that this increased turbulence is the result of Kelvin-Helmholtz waves breaking. However, as our measurements lack any spatial distribution like in Newsom and Banta (2003); Banta et al. (2007), this cannot be stated conclusively. The wave-like motions are visible in the inversion inside the canopy as well, as the vertical motion above the canopy is transferred into the canopy. Due to the low frequency of the motion, the canopy does not dampen the oscillations.

Although wave speed need not to be equal to the average wind speed (except in a symmetric shear layer generating Kelvin-Helmholtz billows), it is tempting to apply Taylor's frozen tubulence hypothesis to assess what horizontal size scale the structure have in case they are purely advected (as in Petenko et al. (2016) and Petenko et al. (2019)f). This allows us to make a rough estimation of the wavelength (λ) using the wave period (τ) and wind speed within the wave layer (V_l): $\lambda = V_l \tau$. For the 27 August event this would lead to a wavelength of 100 – 200 m. The vertical scale has to be estimated, as we only have a single data point above 32 m height. However, the waves are visible at the top of the DTS measured temperature profile, and at the sonic anemometer on top of the tower (48 m height). This means the vertical scale is likely at least in the 20 – 30 meters range .

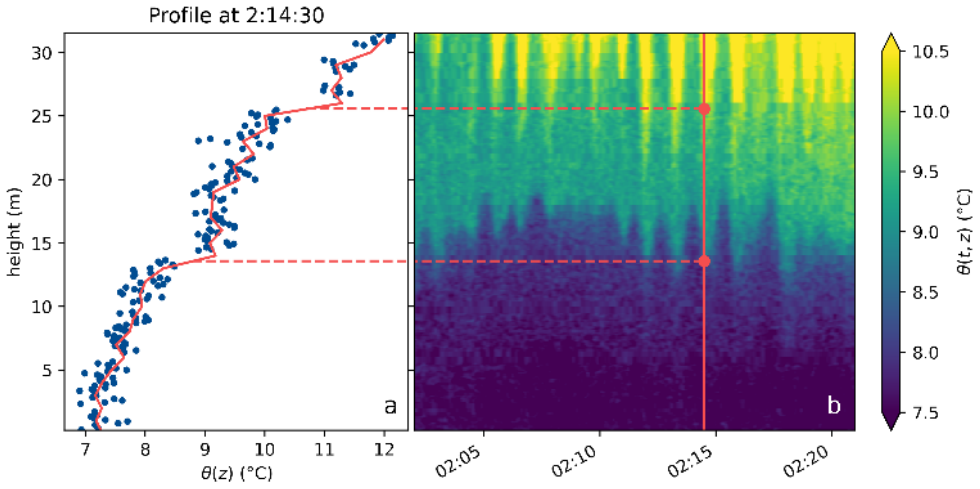

Figure 6.8: Data from an occurrence of a double inversion on 10 September 2019. Figure **a** shows the DTS temperature measurements from one point in time (2:14:30) in blue, with a 1 meter mean in red. The wide distribution of the blue data points is largely due to measurement noise. Figure **b** shows a color plot of the potential temperature in space and time.

However, as we only have data along a single vertical line, and not up or downstream of the tower (like in Heusinkveld et al. (2020)), we can not definitively determine the cause or horizontal size of the wave-like motions. Apart from internal shear instabilities, waves could be induced more directly from a smooth stratified flow over an 'undulating' canopy top or undulating underlying terrain topography.

6.3.4 A wave-like submeso-scale motion

Besides the small scale wave motions, larger scale motions also occurred during the measurement campaign. On the night of 22 – 23 August 2019 a single wave like motion of significant amplitude was visible in the inversion height (Fig. 6.10). The event consisted of three sinusoidal disturbances in the height of a present inversion layer, with a time scale of ~20 minutes. During the disturbances the inversion changed height by 5 – 15 meters. The event was *only* detectable in the 1 m wind speed and the DTS temperature profile. The 3D wind speed measurements (u, w, v) at 48 m did not show any sign of the event. This might indicate that the disturbance is of advective origin rather than transported from above. Some signal of the event was visible in the sonic temperature at 48 m. Before and during the event the wind direction both above the canopy and at 1 m was ~200°(south-southwest).

The temperature decrease of the air under the inversion layer corresponds with a cooling rate of approximately 6 W m^{-2}, assuming no advection or mixing takes place. During the event there is no radiative cooling of the forest floor (~0 W m^{-2}), a negligible sensible heat flux at 1 m (3 W m^{-2}), and barely any ground heat flux (-2 W m^{-2}). While there is strong radiative cooling at the canopy top (-70 W m^{-2}), a top-down convective transport is somewhat unlikely due to the presence of the inversion. Thus it is likely that

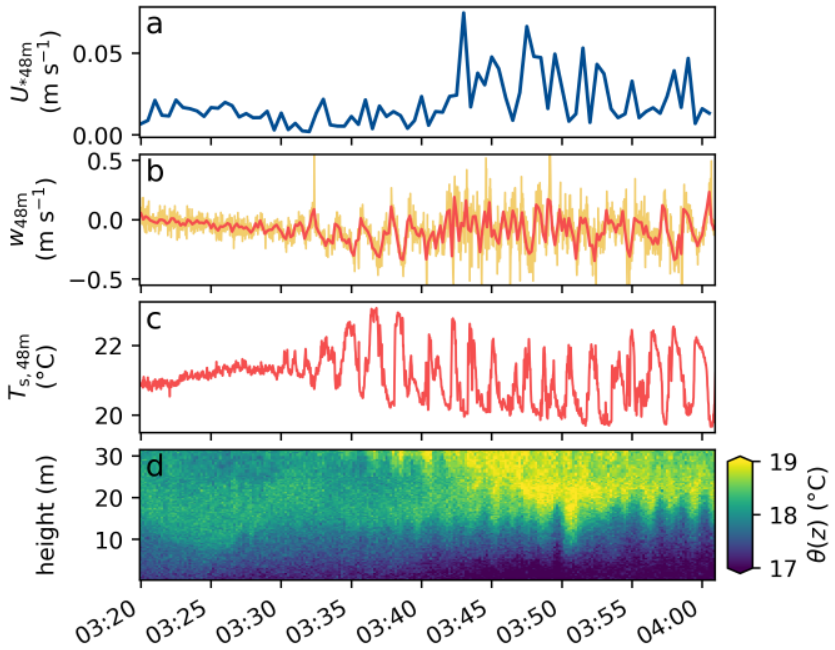

Figure 6.9: Friction velocity above the canopy (**a**), 1 second mean vertical wind speed (**b**, in yellow), 5 second mean vertical wind speed (**b**, in red) above the canopy, sonic temperature above the canopy (**c**), and the DTS-measured temperature profile (**d**) during a wave-like event on 27 August 2019.

the source of the cold air is not local.

However, the slope at the site is approximately southeast (Fig. 2.6), and the wind direction below the canopy is south-southwest. This would make it seem less likely that the origin of the event would be pulsating cold air drainage or density flows (Mahrt, 2007), as those would likely follow the direction of the slope.

6.3.5 Why could inversions within the canopy often elude detection?

While inversions within the canopy occurred frequently during this measurement campaign, it had not been clearly detected before at this site, both in studies without (Bosveld et al., 1999) as well as with DTS measurements (Schilperoort et al., 2018, 2020). In Schilperoort et al. (2020) it was inferred that some 'blocking layer' was present, but as armored DTS cables were used, the time response of the cable was insufficient to see a sharp inversion. The inversion often moves around and oscillates with a period of around 1 – 2 minutes. This makes detecting the presence of a sharp inversion difficult if the time response of the used sensors is longer than 15 – 30 seconds (1/4 of the period of the oscillations, to avoid aliasing).

Besides only time response, the vertical spatial resolution is also important in detecting

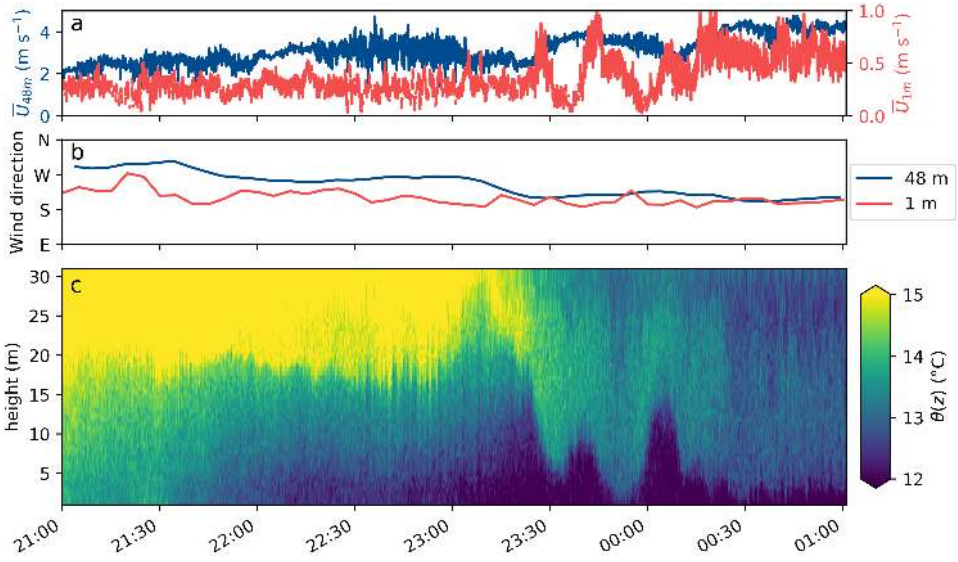

Figure 6.10: Wind speed (**a**), wind direction (**b**) and temperature data (**c**) from the wave-like event on the night of 22 – 23 August 2019. Note that the wind speed (**a**) has two different scales for the two measurement heights. After an inversion at around 18 meters lasting until 23:00, a clear wavelike feature can be seen starting at 23:20, and lasting until 00:15.

the inversions. If DTS is used this is generally not a problem because these devices typically have a spatial resolution between 0.25 and 1 m. However, when using classical discrete sensors, the density of sensors can become an issue. A large amount of fast response sensors (e.g., fast-response thermocouples or sonic anemometers) would be required, one every ~2 m. For a subcanopy with a height of 20 meters this will quickly become a practical and financial issue.

Because detection of local inversions requires a very high measurement resolution, they are difficult to see with classic point sensors. This could mean this type of inversion is very common, but that they have thus far eluded detection.

6.4 Conceptual model for temperature-gradient sharpening

To test the hypothesis that layer formation is due to increased (turbulent) mixing near the canopy and forest floor, we created a conceptual model with the minimum ingredients to form a sharp inversion in the middle of the canopy. The 1-D numerical model describes the evolution of the (vertical) temperature profile with an effective turbulent diffusivity K;

$$\frac{\partial \theta}{\partial t} = \frac{\partial}{\partial z} K \frac{\partial \theta}{\partial z} \tag{6.4}$$

where K is modeled by considering the effects of a constant background diffusivity (K_b), a stability correction, and a height-dependent correction in a dimensionless setting;

$$K_c = K_b \left(1 + 4\frac{C_k}{z_c^2}\left(z(z - z_c)\right)\right) \tag{6.5}$$

which will create a parabolic profile, where z_c represents the height of the canopy, and C_k determines the minimal value (namely $(1 - C_k)K_b$) in the center of the profile. The parabolic profile is chosen to represent increased mixing at the ground surface and canopy crown compared to the trunk region, as wind shear is highest near the ground surface and canopy. Note that the surface flux is computed as $H = K\frac{\partial\theta}{\partial z}$. A stability correction is applied to K_c, to account for the suppression of mixing by stable stratification;

$$K = K_c e^{-\alpha\frac{\partial\theta}{\partial z}} \tag{6.6}$$

with α as an inverse temperature-gradient scale, which controls the stability correction. For the numerical implementation a minimal diffusivity (K_{min}) is needed to prevent the diffusivity to approach 0. As the exact source of the cold air is unknown, and to simplify the model, a constant temperature difference of $\Delta\theta$ is maintained between the top ($z = z_c$) and bottom ($z = 0$) of the profile. Equation 6.4 is solved using the freely available Basilisk toolbox (Popinet, 2015) and the setup details can be found online (van Hooft and Schilperoort, 2021).

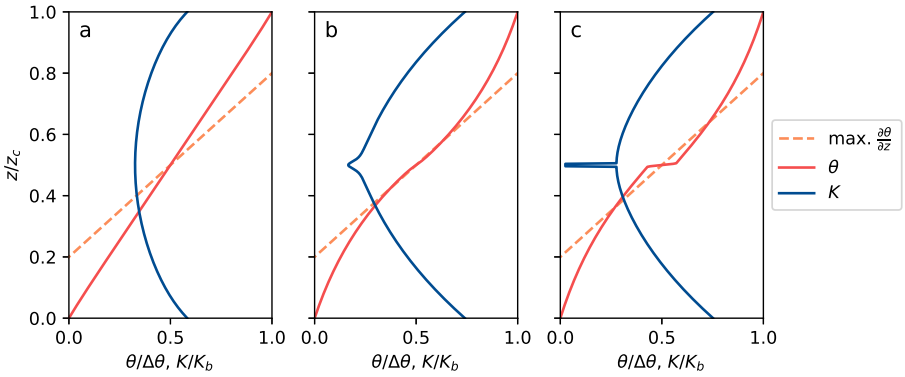

Figure 6.11: The formation of an inversion layer based on the 1-D model. **a** shows the initial conditions, **b** shows the onset of the collapse, and **c** shows the resulting inversion layer. The dashed orange line shows a profile with the maximum sustainable temperature gradient (see text). If the actual gradient is sharper than this theoretical limit a local inversion jump is formed.

Figure 6.11 shows how the inversion layer forms in the 1-D model. The temperature gradient in the center of the profile will become sharper, until the gradient matches the maximum sustainable value. After reaching this the system quickly collapses forming a discrete temperature change in the center of the profile. Values of C_k and α were tuned to generate layer formation.

In order to better understand the details of the presented conceptual system, we analyze the existence of steady-state solutions. A steady state solution is characterized by a heat flux which is constant over height. For a system that is not collapsed;

$$H = K\frac{\partial\theta}{\partial z} = K_c e^{-\alpha\frac{\partial\theta}{\partial z}} \cdot \frac{\partial\theta}{\partial z} \tag{6.7}$$

which has a maximum gradient for $\frac{\partial\theta}{\partial z}(z = 0.5z_c) = \alpha^{-1}$. With stronger temperature gradients the heat flux will decrease and the system will collapse, following the theory of maximum sustainable heat flux (Van de Wiel et al., 2012a,b). This concept is illustrated by Fig. 6.12, which shows the heat flux as a function of the temperature gradient. With an increasing gradient the heat flux reaches a maximum at $\partial\theta/\partial z = \alpha^{-1} = \sim 1.67$ K m^{-1}, after which it decreases. At the left hand side of the maximum a negative feedback occurs: a larger temperature inversion result in a larger flux, which decreases the temperature contrast over the inversion. On the right hand side however, a positive feedback occurs: a stronger inversion decreases the heat flux, which results in a stronger inversion. The positive feedback is enabled by the non-linear dependency of K with respect to $\frac{\partial\theta}{\partial z}$.

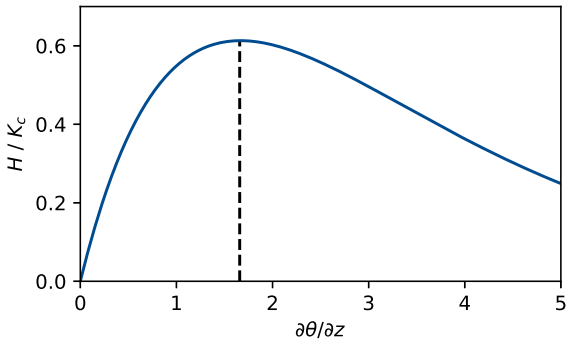

Figure 6.12: The heat flux H (scaled by K_c), shown against the temperature gradient. With an increasing gradient, the heat flux will increase up to $\frac{\partial\theta}{\partial z} \approx \sim 1.67$ K m^{-1}, after which the heat flux decreases with increasing gradient. The maximum sustainable heat flux is illustrated by the dashed line, which is at $\frac{\partial\theta}{\partial z} = \alpha^{-1}$ K m^{-1}

As the height-average of $\frac{\partial\theta}{\partial z}$ is equal to $\langle\frac{\partial\theta}{\partial z}\rangle = \Delta\theta/z_c$, and the fact that the temperature gradient is strongest in the middle of the profile ($z = 0.5z_c$), we can derive that the system is always (mathematically) unstable when for the overall or *bulk* inversion;

$$\Delta\theta > \frac{z_c}{\alpha}, \tag{6.8}$$

and will collapse for any value of C_k. Higher values of α will cause the system to collapse at a lower bulk $\Delta\theta$. Note that higher values of C_k can allow the collapse to occur before the bulk condition (Eq. 6.8) is met. This is because a higher value of C_k allows K_c to become small locally. The *local* $\frac{\partial\theta}{\partial z}$ can then already reach the critical value of α^{-1} while the overall (bulk) gradient is modest and smaller than in Eq. 6.8. This is illustrated in Figure 6.11b.

These results agree with our hypothesis and findings, and thus the simple model ingredients could hint at a potential mechanism for the formation of sharp inversions. However, this can not be conclusively stated from this simplified model and with the available measurement data.

6.5 Conclusions and recommendations

This study demonstrated the presence of a previously not directly observed phenomenon; a spatially localized and highly dynamic inversion in the understory of a tall forest canopy. The presence of an inversion below the canopy will have a large effect on vertical transport of gasses such as carbon dioxide. The forest floor and soil are large sources of carbon dioxide, and any gas released at night during an inversion will not be transported vertically to the sensors above the canopy. The strong inversion was mostly present five to ten meters below the dense overstory, and formed during nights with strong radiative cooling and low friction velocities. The inversions did not build up from the forest floor. Instead, the source of the cold air was either cold air falling down from the canopy top or supplied through advection. However, in the locally measured temperature profile the air near the forest floor was generally 1 – 2 K colder than the air in the canopy top, leaving advection as the most likely candidate.

A possible mechanic that could explain the formation of sharp inversions within the canopy could be a local minimum in the diffusivity. There is top-down mixing near the canopy top, and shear near the forest floor, while the middle of the understory is very bare. This mechanic was studied using a conceptual model with minimal ingredients, which gave results in line with the hypothesis. We found that a sharp inversion layer would always form within the canopy if the temperature difference between the forest floor and canopy top was large enough.

The inversion within the canopy was not the only one present. Above the canopy a second inversion regularly occurred, as would be expected under nocturnal conditions. Wave-like motions of this second inversion, possibly due to Kelvin-Helmholz billows, induced waves in the inversion inside the canopy. These wave-like motions had a period of 50 – 100 seconds, with an amplitude of at least 20 – 30 meters above the canopy, and a reduced amplitude of 5 – 10 meters within the canopy. Wave-like motions at larger scales were also detected. These submeso-scale motions were more transient and their source could not be conclusively determined.

While persistent temperature inversions within the canopy could be a feature specific to this study site, it is possible that this is a more regular feature in similarly structured canopies. Due to the vertical oscillations of the sharp inversion, sensors with a fast time response (better than 15 – 30 seconds) have to be vertically distributed over the height of the canopy. Traditional temperature sensors do not respond fast enough, and sensors that do, like ultrasonic anemometers, are too costly to place at the required density. Due to these practical issues, features such as a sharp inversion within the canopy can often elude detection.

The fiber support structures did influence the data analysis, either when leaving them in (the fiber temperature will be affected by them), or when leaving gaps in the data. In follow up research a straddled support structure could be used to overcome this issue, where two stretches of optical fiber are placed in close proximity to each other without

sharing the same support structure at the same heights. This would allow for a continuous temperature profile to be measured without gaps or artifacts. An increase in the number of fibers would also allow averaging them, thus lowering the measurement noise, allowing more subtle features to be detected.

By additionally using actively heated fiber optics, a continuous wind speed profile could be measured in addition to just the air temperature. The wind speed profile would aid in describing the interaction between the atmosphere and the canopy, as it would allow studying the wind shear, which is the driver of the turbulent mixing. To be able to study the wave-like features of the inversions in more detail, and to be able to conclusively determine their source, spatially distributed measurements, e.g., upstream and downstream of the tower, would additionally be required. With such a setup, it would be possible in the near future to finally explain the observed inversions and wave-like motions.

7

A DTS BASED SOIL TEMPERATURE PROFILER

View of the forest floor at the Speulderbos measurement site

7.1 Introduction

The exchange of heat between the atmosphere and the land surface is one of the main components of the local energy balance, together with irradiation and the sensible and latent heat fluxes. This heat exchange takes place at the surface, but is driven by the temperature gradient between the surface and soil deeper down. The process is strongly affected by soil cover, the soil type and the hydraulic and thermal properties of the soil.

In order to study land-atmosphere heat exchange knowledge of the surface-skin temperature is important (Holtslag and De Bruin, 1988; Heusinkveld et al., 2004). Unfortunately, from an observational perspective, measuring this 'skin' temperature is very challenging (Van de Wiel et al., 2003). With traditional sensors the upper soil is easily disturbed, as the observation should be done as close to the surface as possible. Moreover, the soil near the surface tends often is strongly heterogeneous due to enhanced organic matter content as compared to deeper mineral layers. As measurements of the 'skin temperature' are made at finite depth, it can thus be questioned how representative these are.

Alternatively, modeling approaches can be followed in order to infer the skin temperature from the deeper soil temperatures: as the surface temperature varies with the diurnal rhythm, many analyses focus on the amplitude damping (van Wijk and de Vries, 1963; Van de Wiel et al., 2003), phase shifts, or harmonics (Verhoef, 2004; Heusinkveld et al., 2004; van der Tol, 2012; van der Linden et al., 2021) to model the propagation of heat through the soil. With these methods, the soil temperature and heat flux measured at certain depths are interpolated and extrapolated to obtain an entire profile, or the heat flux and temperature at the surface. However, these methods are sensitive to the parameterization of, among others, 'how easily heat moves through the soil', i.e. the soil thermal diffusivity (Xie et al., 2019). For determining the soil thermal diffusivity, the soil temperature at at least three depths is required (although if one assumes the soil to be homogeneous over depth, two can suffice). This means that high resolution profiles of thermal diffusivity require an even higher density of temperature measurements.

Not only are the soil temperature models sensitive to the parameterization, great care has to be taken in the placement of the sensors themselves. Near the surface temperatures can be very heterogeneous, due to differences in soil cover or vegetation height. Deeper down this is less of an issue, as any surface differences will smooth out due to lateral diffusion. Note due to strong gradients near surface a small change in depth will result in a large change in temperature. Thus, exact determination of the depth at which the sensors are located is very important as uncertainties in this will propagate through the analysis (Dong et al., 2016). Some soil sensors already take this into account, by affixing multiple temperature sensors to a solid structure which is placed into the soil, ensuring that the relative spacing is accurate down to the millimeter.

In recent years distributed temperature sensing (DTS) has become more prominent in studies of soil temperature and properties. Many of these studies have aimed to measure the spatial distribution of soil moisture, either with passive measurements combined with the soil properties (Steele-Dunne et al., 2010), or by actively heating the fiber-optic cable to gain more information on the soil (Sayde et al., 2010; Shehata et al., 2020; Wu et al., 2021) Other studies focused on measuring the spatial distribution of the soil or surface heat flux (Jansen et al., 2011; Dong et al., 2016; Bense et al., 2016). In nearly all these studies the fiber-optic cables were placed horizontally in the soil, sometimes with a specially designed

plow. Even then, horizontal cable placements will have some uncertainty and small errors in the placement depth strongly affect results (Steele-Dunne et al., 2010). However, simply placing a cable vertically has no use due to the spatial resolution of DTS measurements, which is 0.25 m at its best. To overcome this, the cable can be placed in a *fixed coil* shape (Hilgersom et al., 2016; Schilperoort et al., 2020; Wu et al., 2020). Affixing the cable to a coil effectively increases the vertical resolution, and can ensure that the distance between each measurement point is both fixed and more accurate than with separate sensors or cables.

To this end we designed a DTS-based soil temperature probe that can be placed in the soil using a fiber-optic cable as the screw-thread. In this chapter we discuss the design of the probe, how to build it, and we test the probe in the field with a comparison to reference sensors. We present the temperature profiles and derived diffusivity profiles that can be measured using the probe, as compared to standard discrete sensors. Lastly, we will discuss the limitations of the design and give an outlook to improvements and future use cases.

7.2 Materials and Methods

7.2.1 Probe design

The concept behind the design is twofold; place more optical fiber in a smaller space for a higher resolution, and create a helical screw thread. When the fiber optic (FO) cable that is used for the probe has a large diameter, the cable itself can act like the screw thread to ensure good contact with the soil. This is required to get a representative temperature measurement, and will also prevent water from flowing straight down along the tube. Such a probe could be constructed by 3D printing or adding a spiral groove in, e.g., a PVC pipe with a lathe. Besides good soil contact, a cable with a low heat capacity and low thermal conductivity is also required to avoid disturbing the temperature profile of the soil. As cables with a large diameter often have metal inside them, which is highly conductive, we chose to use a thin fiber optic cable as an alternative. However, with smaller diameter cables, the 'screw thread' would not protrude out from the core as far. This could cause insufficient contact with the soil. A second issue is that smaller diameter cables have less protection of the fiber, which increases the chance of the fiber being damaged during installation.

To mitigate these problems, a protruding screw thread is incorporated into the design used in this chapter (Fig. 7.2). This creates a screw that makes good contact with the soil, and provides a groove to install the fiber optic cable into.

Inside the probe is an empty central tube. This space runs vertically through the probe, and allows the routing of the fiber optic cable back to the top of the probe. During assembly it is filled in with expanding polyurethane foam to prevent heat transport and to seal out moisture. Hexagonal protrusions and slots are present on the top and bottom of the segments to make alignment easier during assembly.

7.2.2 Fused filament 3D printing

To manufacture this design we used consumer grade 3D printing technology. The most common consumer 3D printers make use of the 'fused filament fabrication' method, where a computer guided extruder heats up plastic filament and deposits it in the right location to form an object (Chua, Chee Kai; Leong, Kah Fai; Lim, 2003). The extruder can only print

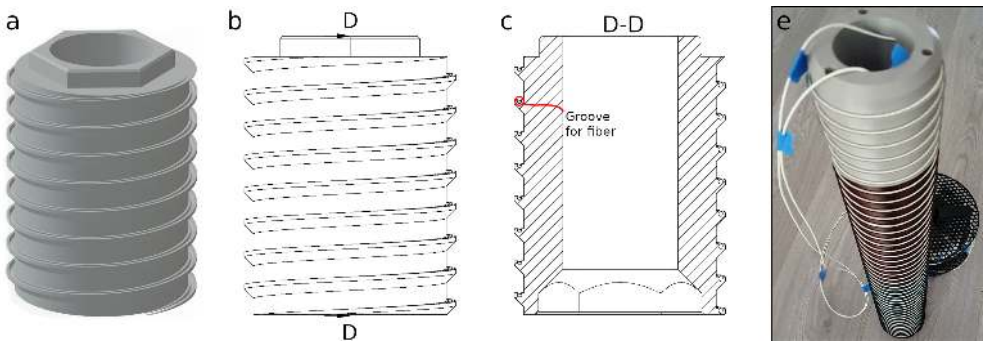

Figure 7.2: 3D render (a), a side view (b) and a vertical cross-section (c) of a segment of the DTS probe. A photo of the probe with all elements assembled is shown in (e).

lines with a width of the nozzle (most commonly 0.4 mm). The printing is done layer by layer to slowly build up an object in the vertical axis. A limitation of this method of 3D printing is that new layers have to be supported by layers below, which puts a limitation on the shapes that can be printed without adding support material. So-called 'overhangs' are possible, but have a maximum angle of around 50 degrees before the plastic will droop.

For our sensor the plastics PLA and PETG can be used as printing material. These two are easily printable on consumer printers, without the need for post-processing or special enclosures. PLA is not recommended for parts in sunlight, or in places where soil temperature exceeds 50 °C, as it is not heat resistant or UV-stable.

The bulk density of printed objects can be substantially lower than the material density, as only the shell is made of solid plastic. In contrast, the internal volume is printed with so called 'infill'. This infill can take on different structures. Generally, the infill of a print is set to a certain percentage of the volume, e.g., an infill of 40% means that 40% of the internal volume consists of plastic and the remaining 60% is air. The bulk density of a printed part can be determined by dividing the final weight of the printed part by the volume the part takes up (as derived from the 3D model). The chosen infill structure will depend on the required properties. In this case we chose for a 'cubic' infill, which will fill the volume with tessellated cubes. This structure will create enclosed pockets of air, which will hinder convection and as such reduce the heat flux through the printed part.

The pure plastic out of which the probe is constructed has quite a high heat capacity (Table 7.1). However, due to the hollow structure of the 3D printed parts and the polyurethane foam core of the probe, the thermal conductivity and heat capacity will be lower than the soil.

A middle section of the probe printed in PLA plastic has an effective infill of 48%; more than half of the volume of the object consisted of air pockets. This results in a heat capacity which is lower than most soils, even when the soil has a high fraction of air-filled pores. The effective thermal conductivity is at least a factor of 4 lower than dry soils, thus causing a minimal effect of the probe itself on the distribution of temperature in the soil.

	PLA	PETG	PLA probe section	Sandy, silty or clay soils
(bulk) density (kg m^{-3})	1240[a]	1270[a]	595	
specific heat capacity (J kg^{-1} K^{-1})	1590[b]	1300[c]	1590	
volumetric heat capacity (10^3 J m^{-3} K^{-1})			946	1200 – 2800[d]
thermal conductivity (W m^{-1} K^{-1})	0.11[b]	0.21[c]	0.05	0.2 – 2.2[d]

Table 7.1: Thermal properties of 3D printed plastics and a section of the printed probe, compared to typical values of sandy, silty or clay soils. [a]Prusa Research (2018, 2020).[b]At ~50 °C (Farah et al., 2016). [c] Rigid.ink (2017). [d]Over the full range of volumetric water content and air-filled porosity (Ochsner et al., 2001).

7.2.3 Probe assembly

The parts are 3D printed on a Prusa Mk3 printer (Prusa Research, Prague, Czech Republic), using Prusament PLA filament for all segments embedded in the soil and Prusament PETG filament for the top (Prusa Research, 2018, 2020). No post-processing of the printed parts was needed. All segments are glued together using cyanoacrylate adhesive (superglue). We used five segments, making the total length of the probe 50 cm, out of which 45 cm has a groove for the fiber optic cable.

A fiber optic cable with a diameter of 1.6 mm is routed via the top through the hole at the bottom of the helix. The cable is then coiled around, using the groove as a guide. While coiling the cable it is glued in place using cyanoacrylate glue, which will provide a good bond between the cable and the PLA or PETG plastic. When getting near to the end of the spiral, the rest of the cable will have to be routed through the top hole. After this is done the remaining part of the spiral can be glued in place. When the spiral is in place, the bottom cap can be added to the probe, and the core can be filled with expanding polyurethane foam. This filling will prevent vertical transport of heat or water ingress through the core of the probe. After this the top cap can be installed to finish the probe.

7.2.4 Probe and reference sensor installation

The soil probe was tested at the Speulderbos study site, between 15 July 2020 and 30 September 2020. To install the probe, a layer of moss and needles was carefully removed and placed to the side. A hole was pre-drilled using an auger, and the probe was inserted into the soil by screwing it in place, leaving the top sticking out. A specially designed tool was used to insert the DTS probe into the soil (Fig. 7.3). After this some of the sand that was removed with the auger was flushed back in using water, until no more sand flushed down. Some removed moss and needles was carefully placed back around the probe, to restore the previous soil cover.

For reference, four Onset TMCx-HD temperature sensors were placed into the soil at a distance of ~50 cm from the DTS probe. The sensors were connected to an Onset HOBO 4-Channel External Data Logger (HOBO U12-008). In this setup the temperature sensors have a manufacturer specified accuracy of ±0.25 K. A hole was dug and the sensors were horizontally inserted into the soil at depths of 0, 10, and 30 centimeters (Fig. 7.4). The litter layer consisting of moss, twigs and needles has a depth of varying between 2 and 5 cm. Another temperature sensor was inserted in the litter layer, approximately 2.5 centimeters

Figure 7.3: Installing the DTS probe using the installation tool (left), the probe during installation (center), and the probe after removal (right).

above sensor at the soil-litter interface. The depth of this sensor will be represented by a value of -2.5 cm.

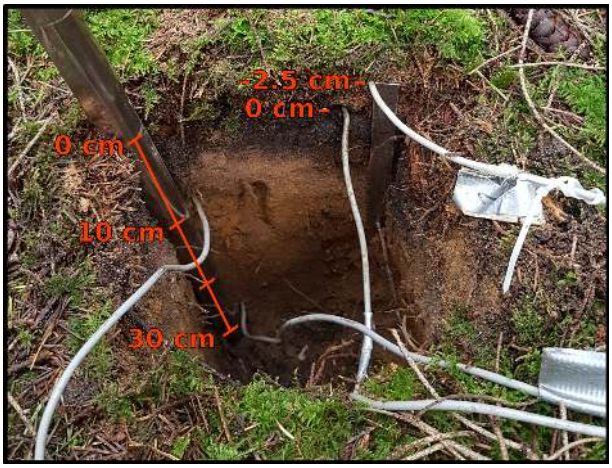

Figure 7.4: Installation of reference sensors. One sensor was placed in the litter layer, the others at 0, 10 and 30 cm depth relative to the soil-litter interface. Notice the decreasing organic content with depth.

7.2.5 Fiber optic configuration and calibration

For performing the DTS measurements an Ultima-M (Silixa Ltd., Elstree, UK) DTS unit was used. The Ultima-M was housed in a small container on the forest floor. The DTS probe consisted of one long FO cable without splices. From the DTS machine the cable was routed out of the container, through a heated bath, and through a bath at ambient temperature. Both baths were kept mixed using aquarium air pumps with air stones. After the baths the cable was lead to the measurement location under a suspended steel cable, to

avoid rodents and to protect the fiber from falling branches. After going through the 3-D printed probe, the FO cable was routed back under the steel cable, through both baths, and back into the container. Originally the setup was supposed to be double-ended; where the fiber is interrogated from both sides as to improve calibration. Due to rodent damage at the container, which occurred near the start of the measurement period, the fiber was only measured in a single-ended configuration. This could cause a small systematic error in areas where the fiber is strained, such as in the tight coil of the probe. To ensure the accuracy of the measurements the data from the first day, when the fiber was not damaged yet, was calibrated in both single- and double-ended configurations. The difference between the two was insignificant and as such we proceeded with calibrating the DTS data in single-ended configuration during the entire measurement period.

As the DTS measurements will only provide temperature as a function of the *length along the optical fiber*, these coordinates have to be transformed into depth values. This consists of two steps; translating the scale from meters along the fiber to centimeters along the coil by using the dimensions of the coil (radius, pitch, height), and aligning the soil surface of the probe. The surface can be aligned ('benchmarked') by doing a heat trace experiment, where a specific section of the coil (e.g., part sticking out above the surface) is heated or cooled, and the location along the length of the fiber where there is a sharp temperature spike is noted down. Alternatively, the probe can be aligned by comparing its temperature to the temperature of a reference temperature sensor at a known depth, and minimizing the difference between the two. In this study the final depth alignment of the probes was performed using the reference sensor at 10 cm. This depth was chosen because small local effects will average out across the soil. To avoid misalignment due to a constant bias between the two sensors, the amplitude of the diurnal temperature oscillation was used for alignment.

7.2.6 Determining soil diffusivity

The thermal diffusivity of a medium can be determined using a measured temperature profile through time. If we assume that the medium is homogeneous, the diffusion of heat through the soil can be described by the following equation:

$$\frac{\partial T}{\partial t} = D\frac{\partial^2 T}{\partial z^2} = \frac{\kappa}{C}\frac{\partial^2 T}{\partial z^2} \tag{7.1}$$

where T is the soil temperature (K) at a certain depth z (m), t the time (s), D the thermal diffusivity ($m^2\ s^{-1}$). With only a temperature profile over time, we cannot discern between the thermal conductivity, κ ($W\ m^{-1}\ K^{-1}$), and the heat capacity, C ($J\ m^{-3}\ K^{-1}$). This would require that soil properties are determined in a lab, or a heat flux plate is installed next to the measured profile. Note that in Eq. 7.1 the effects of latent heat fluxes or heat transported by the movement of air or water are neglected (Steele-Dunne et al., 2010).

Since the observations provide information of the soil temperature over depth and time, in principle the 'effective' D could be calculated directly from the discretized version of equation 7.1. However, attention has to be given to proper estimation of the second derivative, because small observational errors may lead to a large uncertainty. Here we choose to estimate the diffusivity by fitting a numerical model of Eq. 7.1 to the measured temperature data, assuming that the diffusivity is constant in time over the period that

is studied. We used a (second-order) central finite difference equation (Vuik et al., 2007) to describe the evolution of temperature through time, for a section between two depths. The measured temperatures at the top and bottom of this section are prescribed, and the temperature in the middle is modeled with an estimate for the diffusivity. By comparing the modeled temperature to the measured temperature the difference can be minimized, and the apparent diffusivity determined.

$$\frac{\partial T(z)}{\partial t} \approx D \frac{T(z+\Delta z) - 2T(z) + T(z-\Delta z)}{(\Delta z)^2} \tag{7.2}$$

Due to the large amount of measurement points of the DTS probe, this equation can be used to determine the thermal diffusivity of the soil as a function of depth over the entire vertical profile. This could be expanded upon by incorporating more nearby measurement points for more accuracy, instead of the three points of Eq. 7.2.

While Eq. 7.2 has equidistant spacing, this is not necessarily required. For an irregularly spaced sampling, such as with the separate reference probes, the equations can be adjusted (Fornberg, 1988; Taylor, 2016). However, as the reference sensors only measured at four locations in depth, the thermal diffusivity can only be calculated for two (overlapping) sections.

7.3 Results and Discussion

7.3.1 Sample temperature profile

To demonstrate what the data from the probe looks like, Fig. 7.5 shows the evolution of the soil temperature profile over a 24 hour period; 1 August 12:00 until 2 August 12:00.

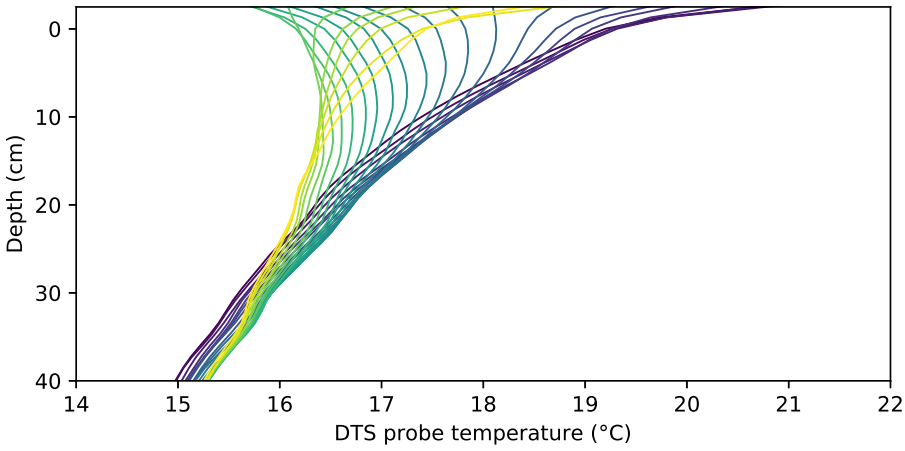

Figure 7.5: Temperature over depth as measured by the DTS probe. Hourly data from noon at 1 August 2020 (dark color) to noon 2 August 2020 (light color). The highest and lowest surface temperature occurred at 13:00 and 5:00 respectively.

Starting at midday, the temperature profile is warmest at the top, cooling monotonously towards the deepest measurement at 40 cm depth. Soon after this point in time the soil

near the surface starts cooling continuously until early morning. However, the soil below around 30 cm depth continues warming throughout the entire period shown (probably as a result of a long-time scale trend in the weather). Note the extremely large gradients near surface. In particular those gradients are difficult to measure with traditional temperature sensing. During the night the surface cools down the most, creating a zone 10 – 15 cm below the surface which is warmer than both the soil above and below. This local maximum persists until the soil warms up in the morning and a monotonous profile returns. Due to the very exact vertical spacing and high resolution of the DTS probe, phenomena such as this 'hockey stick' profile can be observed.

The soil temperature deeper down was continuously coldest, as both 1 and 2 August were relatively warm days. A downward heat flux at 40 cm was observed from the start of the measurement period (15 July) until the late September.

7.3.2 Comparison with reference sensors

To compare the probe with the reference temperature sensors, the root mean square error between the DTS probe and the reference sensors is computed. However, to reduce any systematic biases between the probe and reference sensors, the data is first detrended based using a five-day moving average. Systematic biases in the temperature can have their origin in, for example, a slight difference in calibration between the probe and reference sensors. The mean biases between the four reference and the DTS probe ranged between 0.10 and 0.30 K, within the expected uncertainty of the reference sensors and DTS measurements.

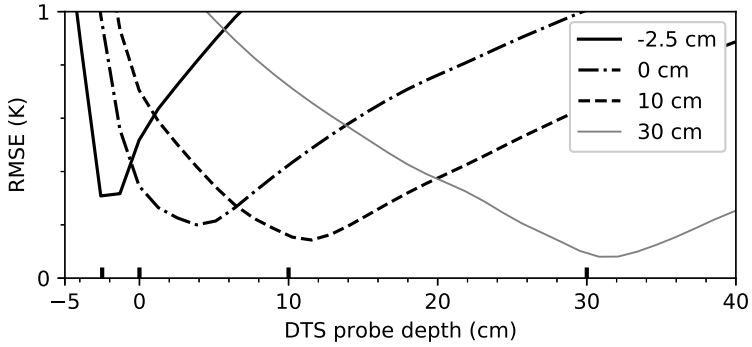

Figure 7.6: Root mean square error (RMSE) of the DTS probe temperature compared to the reference sensors, for the four available depths.

Figure 7.6 shows a good agreement between the DTS probe and the reference sensors, apart from the reference sensor at the soil-litter interface. Even though the probe and reference sensors were placed in relatively close proximity to each other, variations in the thickness of the litter layer could case discrepancies near the surface. Note that the largest error is also expected near the top where the diurnal amplitude is largest (no scaling of the error is applied).

A second way to compare the probe to the reference sensors is to study how much the diurnal variations in temperature are dampened as depth increases. By comparing the data

in this fashion, biases in the absolute temperature are not relevant. Figure 7.7 shows the temperature variance as a function of depth, after detrending using a 5-day running mean. The variance decreases most strongly in the litter layer, and flattens off deeper into the soil. The reference sensors agree mostly with the DTS probe. As calibration was done with the 10cm probe both agree by definition, but also the litter and the 30cm sensors seem to agree well. The sensor at the soil-litter interface deviates again, just as it did in the previous results. Again, it seems that the deviating reference sensor should be at ~4 cm depth, just as Fig. 7.6 shows. However, the physical distance between the reference sensors in the litter and the deviating sensor is 2.5 cm, as can be seen from the ruler in in Fig. 7.4. The source of the deviation is unlikely to be a too-low spatial resolution of the DTS data, as its spatial resolution is 3 cm.

Between the depths of 15 to 40 cm the DTS probe shows an approximately linear decrease in the logarithm of the temperature variance. This exponential dampening is expected, as long as the soil thermal properties do not vary significantly over depth. That the stronger the slope is, the stronger the dampening. Just above the surface, which is covered by a layer of moss and litter, dampening is strongest. Deeper down the dampening is higher as there is less organic matter in the soil.

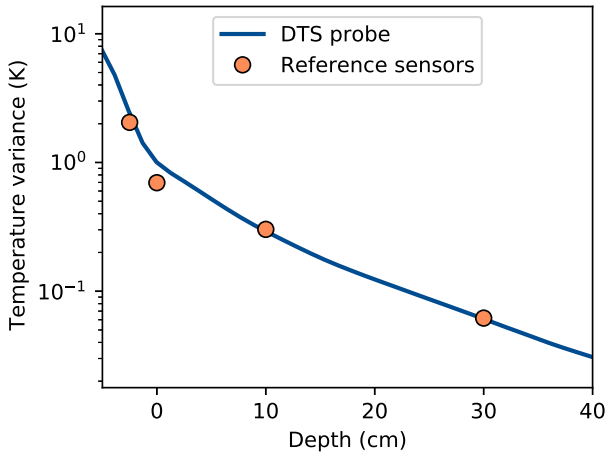

Figure 7.7: Relationship between the temperature variance and depth for DTS probe and reference sensors. Depth values smaller than 0 cm denote parts of the coil possibly sticking out above the surface.

7.3.3 Thermal diffusivity

The availability of an almost continuous temperature profile by the DTS, allows for determination of the soil thermal diffusivity. As there are many data points distributed over the depth, the thermal diffusivity can be estimated in many more intervals compared to standard sensors, as at least 3 measurements of temperature are needed to compute the diffusivity. For the reference sensors only 2 diffusivity values could be computed, using either the sensors at -2.5, 0 and 10 cm, or the sensors at 0, 10 and 30 cm. For the DTS probe data we chose to estimate the diffusivity over increasingly large intervals, from a 2.5

cm wide interval near the surface, to a 10 cm wide interval near the deeper measurement points. This was required as the signal becomes weaker the deeper you go down into the soil, making the uncertainty in the estimate of diffusivity higher. A difficulty of the separate reference sensors is that any uncertainty or error in the relative depths will directly translate into uncertainty or errors in the diffusivity estimate. If, for example, sensors are slightly further away in reality compared to how they are assumed to be, a higher diffusivity value will be found.

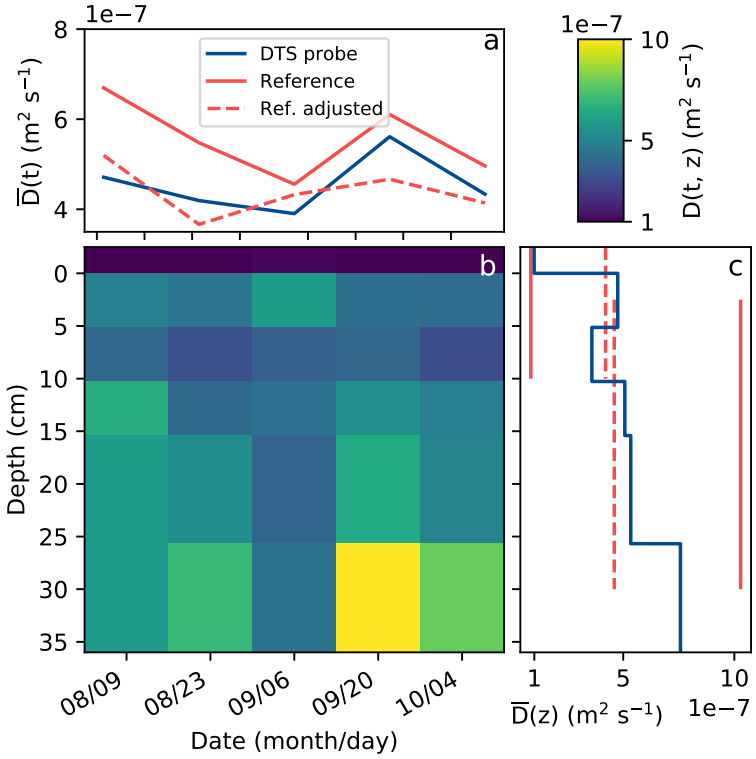

Figure 7.8: **a:** Mean diffusivity as a function of time, of both the reference sensors and the DTS probe. The red dashed line shows the reference if the second sensor depth is assumed to be at 4 cm depth instead of 0. **b:** The diffusivity as measured by the DTS probe as a function of depth and time. **c:** Mean diffusivity as a function of depth, of both the reference sensors and the DTS probe.

Figure 7.8 shows the computed diffusivity values as both a function of time and space. In time the DTS probe and the reference sensors show a very similar pattern in the variations of diffusivity, with just a slight difference in the absolute value. As in Figure 7.7 we saw that the second reference sensor correlated better with the probe's temperature at 4 cm depth, the diffusivity values of the reference data with this adjusted sensor was calculated. This data shows a pattern in the diffusivity over time that correlated less with the DTS probe data, although the mean error is smaller. The adjusted data shows barely any variation in diffusivity over depth.

The change in diffusivity over time is likely related to soil moisture, however for sandy soils this is non-linear with very low moisture contents (under 0.07 kg kg^{-1}, Abu-Hamdeh (2003)). With higher moisture contents the thermal diffusivity of sandy soils is insensitive to moisture, and typically has values around 5×10^{-7} m^2 s^{-1} (Abu-Hamdeh, 2003).

Over depth the data of the DTS probe shows a lot more resolution, from the poorly conducting litter layer at the top (dark blue), to higher diffusivity values deeper down (green and yellow). These values of diffusivity vary due to variations in the soil composition and structure, depending on the content of organic matter or, e.g., gravel. Near the surface the reference sensors at the DTS probe agree in the diffusivity, but for the deeper layers the reference sensors estimate a higher value. The value derived using the DTS probe is closer to the expected value for sandy soils. The two methods previously agreed in the temperature variance at the depths of 10 and 30 cm, and as such the deviating sensor at 0 cm would be the most likely cause of the error. Even a slight misalignment such as inserting the sensor on an angle could cause the actual measurement depth to deviate by a centimeter or more.

7.4 Conclusions and recommendations

In this study we presented a design for a DTS-based soil temperature probe, and we tested its performance in the field. The results were in general agreement with the reference sensors, and were able to show more detail than standard sensors are capable of. It was possible to determine the thermal diffusivity of the soil in resolutions down to 2.5 cm, which is a many times better than the capabilities of discrete probes. With the higher resolution temperature data, the thermal properties of layers in the soil can be determined at a higher resolution.

While the DTS-based soil temperature probe does perform well, and could provide more information than conventional sensors, it is important to consider the cost of DTS interrogators. With the high cost associated with these devices, and the many other possible applications for them (Selker et al., 2006; De Jong et al., 2015; Hilgersom et al., 2016; des Tombe et al., 2018; Izett et al., 2019; Heusinkveld et al., 2020), it would not be logical to use them for soil temperature measurements alone. Even so, the probes can be integrated within a network of other DTS measurement of, for example, air temperature or horizontally distributed soil temperature. As long as the DTS interrogator has available measurement length the FO cables of the different setups can be spliced together into a single continuous fiber, and the entire setup can be measured at once.

To make calibration easier and less dependent on calibration baths, two standard soil temperature sensors could be integrated into the probe. This would allow calibration of the probe even if its more fragile FO cable is spliced to a more manageable and rugged FO cable. As a bonus the calibration baths would not be required anymore, which can simplify the setup.

Although this study only looked at the accuracy of the temperature measurement, the sensor can be expanded upon by using active heat tracer experiments. This would involve integrating an electrical conductor into the probe, e.g., a metal-tube fiber optic cable, and heating this using its electrical resistance (Bakker et al., 2015; van Ramshorst et al., 2019). If the power is supplied in a pulsed manner, the transient response can be studied to derive the the *heat capacity and thermal conductivity* over depth (Sayde et al.,

2010; Striegl and Loheide II, 2012). Using these properties the soil moisture over depth can also be inferred, e.g., as in Wu et al. (2020). In this case two separate probes can be used, where one measures the undisturbed background soil temperature, and the other measures the thermal properties of the soil. As soil moisture it is an important variable in surface hydrology and land-atmosphere interactions, the continuous monitoring with a combination of vertical and horizontal distributed measurements could provide the best of both; capturing spatial heterogeneity while not sacrificing any accuracy.

7.5 Design availability

The design files for all parts of the 3D printed probe are available on `github.com/BSchilperoort/dts_soil_coil`, including 3D renders of all parts.

8 Synthesis

The treetops of Speulderbos

8.1 Main findings

In the previous chapters, several ways were discussed to study heat exchange in coniferous forests, specifically to help to tackle the issues of non-closure of the energy balance and canopy decoupling. This chapter summarizes the findings of these, and discusses their implications both for current and future research. Finally an outlook is given to what developments may lay ahead, and which role distributed temperature sensing can play in these.

8.1.1 On the measurement of air temperature with DTS

Centrally to this thesis are measurements of air temperature with a fiber-optic cable. As the cable will be suspended in the air and subject to the elements, it is essential to characterize the errors that can be expected. In chapter 3 the influence of both sunlight striking the cable, and radiative cooling of the cable was studied. Sunlight causes a ⌀6 mm fiber-optic cable to deviate up to 1.0 K from the true air temperature, especially at very low wind speeds. As is to be expected, more intense insolation causes larger errors. If a higher accuracy is required, the cables have to be shielded from direct sunlight, as is usually done with conventional air temperature sensors.

At night, the FO cable cools down through the emission of long wave radiation. The long-wave cooling rates are an order of magnitude lower than solar radiation, but can still cause very large deviations from the air temperature. During particularly cloudless and low-wind nights, the error can be up to 1.0 K. However, even a small breeze will prevent the error from exceeding 0.5 K. Unlike with sunlight, a screen does not fix the error, as the screen itself will cool down by emitting longwave radiation. For this reason, conventional sensors require active aspiration (Georges and Kaser, 2002), but this is unfeasible for DTS measurements. The results of chapter 3 do show however, that the errors found are very strongly correlated with the net longwave radiation and wind speed, likely due to the low amount of turbulence on clear sky low-wind nights. As such, an empirical relationship can be used to correct the measurements if a higher accuracy is required.

Apart from accuracy, the time response in FO cables is also important to consider. If the cable takes 5 minutes to adjust to a change in air temperature, it is not possible to study processes that happen on smaller time scales. While the thick cables can be attractive due to their robustness, they are too slow to respond for many applications. Thin cables, while fragile, allow studying more transient events and processes. An added advantage is that the thinner cables are less affected by radiation (De Jong et al., 2015), and that an error in the absolute temperature can be irrelevant if the main focus is on variations of air temperature.

8.1.2 Use of dry and wet cable profiles

In chapter 4 the evaporation rate of the Speulderbos forest site was determined using the Bowen ratio, calculated using temperature profiles of a dry and a wet DTS cable. With sufficient shading, the results are in agreement with the standard Eddy Covariance method, despite the very small temperature gradients observed at the site. However, setting up these measurements proves to be very laborious, and as such they are not as useful if the standard methods are available.

However, the dry and wet profiles give more insight into the storage of sensible and latent heat within the canopy. In short canopies, such as most crops, the amount of

heat stored in the air column of the canopy is negligible. In tall canopies, such as at the Speulderbos site, these two storage terms can amount to such a significant portion of the energy balance that they have to be taken into account (20 – 40% of the net radiation, as demonstrated in chapter 4).

Besides energy storage, the air temperature profile as measured with DTS can be used to study decoupling of the understory (Ch. 5) over multiple months and seasons. The understory at the Speulderbos forest site was nearly always colder than the air above the forest, which suppresses turbulent mixing by the wind. However, this temperature difference is both a driver and a result of the decoupling, and knowledge about the wind shear is essential to asses decoupling of the canopy. During the day there usually is enough wind to keep the air in the forest mixed with the air above, but at night the forest regularly (~50% of the time) was in a decoupled state. Interestingly, the air near the forest floor was commonly warmer than the air in the center of the understory. This temperature difference can drive local convection. Nevertheless, the measured continuous temperature profiles can be used to asses to which height this convection could rise. The convection height generally was limited to 5 m during the day, and a maximum of 15 m at night. Thus this convective mixing was confined to the understory due to the stable stratification conditions in the overstory, akin to a capping inversion. The dominance of decoupling at this site again demonstrates that it is very important to take decoupling into account when analyzing above-canopy flux measurements.

8.1.3 Uncovering previously unseen processes

Thin fiber optic cables (⌀0.5 mm) allow studying of the previously theorized capping inversion in more detail, as they take on the air temperature much more rapidly than the previously used thick cables (⌀6 mm). These provide profiles of the air temperature in the forest at a 1 – 5 second resolution. The data now clearly regularly showed a sharp inversion at night, which could not be measured previously. The inversion formed during cloudless low-wind nights, and usually was located in the upper-understory. The inversion was highly dynamic and was generally not stationary in height, moving with wave-like motions at time scales of 50 – 100 seconds and with amplitudes of 5 – 10 meters. With a simple 1-D model a hypothesis was tested, namely that the sharp inversions formed within the canopy due to a local minimum in the diffusivity. The results of the model are in line with the hypothesis, and found that a sharp inversion will always form if the temperature difference between the canopy and forest floor was large enough.

Due to the dynamic nature of the inversions, only a network of very dense (every 2 meters) and fast response (under 30 seconds) is able to measure them. It is possible that they have therefore mostly eluded detection up to now, and could be a very regular feature in similar forests.

8.1.4 Soil temperature probe

The designed DTS-based soil temperature probe is able to measure the soil temperature with high accuracy, although there were some differences between the probe and one of the reference sensors. The main advantage over the reference sensors is that with the very high density of temperature measurements the thermal diffusivity of the soil could be determined at a very high resolution. With more improvements, such as two reference temperature sensors integrated into the probe itself, the probe can be manufactured to be 'plug and play'. This allows users with less intimate knowledge of DTS to still make use of the technology. While the soil thermal diffusivity was determined with high accuracy, the thermal conductivity or heat capacity are still unknown. These parameters can be determined with an additional actively heated DTS probe, to get a full picture of the heat flux and soil composition.

8.2 An outlook

Often the measurements in this thesis lacked sufficient wind data. While the DTS provided measurements of air temperature along the entire profile of the forest, wind speeds were only available from standard sensors at the forest floor and top of the tower. With a profile of wind speed many of the processes studied in this thesis could have been described in much more detail and with more certainty, as wind shear is the driver of turbulent mixing. With actively heated fiber optic cables it is possible to measure a continuous wind speed profile, and for future research this should be considered to be of the highest priority.

Beside wind speed, more spatially distributed measurements can aid in describing the formation of the inversions and help determine the source of the cold air in the subcanopy, which is something not possible to ascertain with the available data. With additional temperature measurements 'upstream' and 'downstream' of the main temperature profile, the scale, motion and extent of the inversions could be determined, and the influence of advection in the local energy balance can be studied. Such data could be acquired with a combination of horizontal stretches of fiber and additional vertical profiles. A combination of this additional wind and temperature data, and more advances in computation models of turbulence could lead a more generalized description of the findings in this thesis.

As all the forest measurements in this thesis were performed at the same site, it would be very important to perform similar measurements at different (intensively measured) forest sites, where the species and canopy structure are different. This can be of twofold use; this could show if the canopy inversions are common, and it could uncover other features or processes that have been missed up to now. For other land covers, such as crops or grassland, the DTS measured vertical profiles will have less added-value as these elements have a much lower height.

Data such as presented here, especially with DTS-measured wind speed profiles, can aid in improving canopy mixing-layer models, which currently do not work well under strongly stable or unstable conditions (Brunet, 2020). Especially the presence of inversions and gravity waves are problematic, and thus determining when these could form can improve the accuracy of these models. The data will also allow for validation of canopy models in large eddy simulation. The continuous profiles can ensure the entire vertical continuum is validated, rather than only a few discrete points along the height of the canopy.

However, a big hurdle for making DTS more common is not the cost of the equipment, but rather the non-standardized nature of the equipment. Even of a single manufacturer the characteristics of the same model DTS machine will differ per unit. This, combined with the complexity of setting up the fiber optic cables, makes every setup unique, and means that a DTS expert is required to be on site regularly for the measurements to be feasible and efficient. More standardization of the equipment and setups is therefore required to stimulate continued use of DTS in these kinds of studies. The soil probe was an attempt to make a DTS-based sensor that could be more 'plug and play'. The first step required is to show that this type of measurements can be performed. With more effort the method can become more mature and full use of its abilities can be made.

Bibliography

References

Abu-Hamdeh, N. H.: Thermal Properties of Soils as affected by Density and Water Content, Biosystems Engineering, 86, 97–102, doi:10.1016/S1537-5110(03)00112-0, URL https://linkinghub.elsevier.com/retrieve/pii/S1537511003001120, 2003.

Alekseychik, P., Mammarella, I., Launiainen, S., Rannik, Ü., and Vesala, T.: Evolution of the nocturnal decoupled layer in a pine forest canopy, Agricultural and Forest Meteorology, 174-175, 15–27, doi:10.1016/j.agrformet.2013.01.011, URL http://dx.doi.org/10.1016/j.agrformet.2013.01.011https://linkinghub.elsevier.com/retrieve/pii/S0168192313000257, 2013.

Allen, R. G., Pereira, L. S., Raes, D., and Smith, M.: FAO Irrigation and Drainage Paper No. 56, Irrigation and Drainage, 300, 300, doi:10.1016/j.eja.2010.12.001, URL http://www.kimberly.uidaho.edu/water/fao56/fao56.pdf, 1998.

Altman, D. G. and Bland, J. M.: Measurement in Medicine: The Analysis of Method Comparison Studies, Journal of the Royal Statistical Society. Series D (The Statistician), 32, 307–317, doi:10.2307/2987937, 1983.

Angus, D. E. and Watts, P. J.: Evapotranspiration - How good is the Bowen ratio method?, Agricultural Water Management, 8, 133–150, doi:10.1016/0378-3774(84)90050-7, 1984.

Aubinet, M., Feigenwinter, C., Heinesch, B., Laffineur, Q., Papale, D., Reichstein, M., Rinne, J., and van Gorsel, E.: Nighttime Flux Correction, in: Eddy Covariance: A Practical Guide to Measurement and DataAnalysis, edited by Aubinet, M., Vesala, T., and Papale, D., pp. 133–157, Springer, Dordrecht/Heidelberg/London/New York, 2012a.

Aubinet, M., Vesala, T., and Papale, D.: Eddy covariance : a practical guide to measurement and data analysis, URL http://public.eblib.com/choice/publicfullrecord.aspx?p=886081, 2012b.

Bakker, M., Caljé, R., Schaars, F., van der Made, K., and de Haas, S.: An active heat tracer experiment to determine groundwater velocities using fiber optic cables installed with direct push equipment, Water Resources Research, 51, 2760–2772, doi:10.1002/2014WR016632, URL https://onlinelibrary.wiley.com/doi/abs/10.1002/2014WR016632, 2015.

Baldocchi, D. D. and Meyers, T. P.: Turbulence structure in a deciduous forest, Boundary-Layer Meteorology, 43, 345–364, doi:10.1007/BF00121712, URL http://link.springer.com/10.1007/BF00121712, 1988.

Banta, R. M., Mahrt, L., Vickers, D., Sun, J., Balsley, B. B., Pichugina, Y. L., and Williams, E. J.: The Very Stable Boundary Layer on Nights with Weak Low-Level Jets, Journal of the Atmospheric Sciences, 64, 3068–3090, doi:10.1175/JAS4002.1, URL https://journals.ametsoc.org/doi/10.1175/JAS4002.1, 2007.

Bao, X. and Chen, L.: Recent progress in distributed fiber optic sensors, Sensors (Basel), 12, 8601–8639, doi:10.3390/s120708601, 2012.

Barr, A. G., King, K. M., Gillespie, T. J., Den Hartog, G., and Neumann, H. H.: A comparison of bowen ratio and eddy correlation sensible and latent heat flux measurements above deciduous forest, Boundary-Layer Meteorology, 71, 21–41, doi:10.1007/BF00709218, 1994.

Barr, A. G., Richardson, A. D., Hollinger, D. Y., Papale, D., Arain, M. A., Black, T. A., Bohrer, G., Dragoni, D., Fischer, M. L., Gu, L., Law, B. E., Margolis, H. A., Mccaughey, J. H., Munger, J. W., Oechel, W., and Schaeffer, K.: Use of change-point detection for friction-velocity threshold evaluation in eddy-covariance studies, Agricultural and Forest Meteorology, 171-172, 31–45, doi:10.1016/j.agrformet.2012.11.023, 2013.

Bense, V. F., Read, T., and Verhoef, A.: Using distributed temperature sensing to monitor field scale dynamics of ground surface temperature and related substrate heat flux, Agricultural and Forest Meteorology, 220, 207–215, doi:10.1016/j.agrformet.2016.01.138, URL http://www.sciencedirect.com/science/article/pii/S0168192316301496, 2016.

Blume, T., Krause, S., Meinikmann, K., and Lewandowski, J.: Upscaling lacustrine groundwater discharge rates by fiber-optic distributed temperature sensing, Water Resources Research, 49, 7929–7944, doi:10.1002/2012WR013215, 2013.

Bolognini, G. and Hartog, A.: Raman-based fibre sensors: Trends and applications, Optical Fiber Technology, 19, 678–688, doi:10.1016/j.yofte.2013.08.003, URL https://linkinghub.elsevier.com/retrieve/pii/S1068520013001090, 2013.

Bosveld, F. C.: The Cabauw In-situ Observational Program 2000- Present: Instruments, Calibrations and Setup, Tech. rep., Royal Netherlands Meteorological Institute, URL http://bibliotheek.knmi.nl/knmipubTR/TR384.pdf, 2020.

Bosveld, F. C., Holtslag, A. A., and Van Den Hurk, B. J.: Nighttime convection in the interior of a dense Douglas fir forest, Boundary-Layer Meteorology, 93, 171–195, doi:10.1023/A:1002039610790, 1999.

Bosveld, F. C., Baas, P., Beljaars, A. C., Holtslag, A. A., de Arellano, J. V. G., and van de Wiel, B. J.: Fifty Years of Atmospheric Boundary-Layer Research at Cabauw Serving Weather, Air Quality and Climate, Boundary-Layer Meteorology, 177, 583–612, doi:10.1007/s10546-020-00541-w, URL https://doi.org/10.1007/s10546-020-00541-w, 2020.

Bowen, I. S.: The ratio of heat losses by conduction and by evaporation from any water surface, Physical Review, 27, 779–787, doi:10.1103/PhysRev.27.779, 1926.

Brunet, Y.: Turbulent Flow in Plant Canopies: Historical Perspective and Overview, vol. 177, Springer Netherlands, doi:10.1007/s10546-020-00560-7, URL https://doi.org/10.1007/s10546-020-00560-7, 2020.

Burba, G.: Eddy Covariance Method for Scientific, Industrial, Agricultural, and Regulatory Applications, LI-COR Biosciences, Lincoln, USA, 2013.

Burba, G., Anderson, D., and Burba, G.: A brief practical guide to eddy covariance flux measurements : principles and workflow examples for scientific and industrial applications, LI-COR, Lincoln, Neb., 2010.

Cava, D. and Katul, G. G.: The Effects of Thermal Stratification on Clustering Properties of Canopy Turbulence, Boundary-Layer Meteorology, 130, 307–325, doi:10.1007/s10546-008-9342-6, URL http://link.springer.com/10.1007/s10546-008-9342-6, 2009.

Chi, J., Zhao, P., Klosterhalfen, A., Jocher, G., Kljun, N., Nilsson, M. B., and Peichl, M.: Agricultural and Forest Meteorology Forest floor fluxes drive differences in the carbon balance of contrasting boreal forest stands, Agricultural and Forest Meteorology, 306, 108 454, doi:10.1016/j.agrformet.2021.108454, URL https://doi.org/10.1016/j.agrformet.2021.108454, 2021.

Chua, Chee Kai; Leong, Kah Fai; Lim, C. S.: Rapid Prototyping: Principles and Applications, World Scientific, Singapore, 2003.

Cisneros Vaca, C., Ghimire, C. P., and van der Tol, C.: Spatial Patterns and Temporal Stability of Throughfall in a Mature Douglas-fir Forest, Water, 10, doi:10.3390/w10030317, URL http://www.mdpi.com/2073-4441/10/3/317, 2018a.

Cisneros Vaca, C., van der Tol, C., and Ghimire, C. P.: The influence of long-term changes in canopy structure on rainfall interception loss: a case study in Speulderbos, the Netherlands, Hydrology and Earth System Sciences, 22, 3701–3719, doi:10.5194/hess-22-3701-2018, URL https://www.hydrol-earth-syst-sci.net/22/3701/2018/, 2018b.

Coenders-Gerrits, M., Schilperoort, B., and Jiménez-Rodríguez, C.: Evaporative Processes on Vegetation: An Inside Look, in: Precipitation Partitioning by Vegetation, pp. 35–48, Springer International Publishing, Cham, doi:10.1007/978-3-030-29702-2_3, URL http://link.springer.com/10.1007/978-3-030-29702-2{_}3, 2020.

Culf, A. D., Foken, T., and Gash, J. H. C.: The Energy Balance Closure Problem, in: Vegetation, Water, Humans and the Climate, edited by Kabat, P., chap. B.2, pp. 159–166, Springer, Berlin, doi:10.1007/978-3-642-18948-7_13, 2004.

Dakin, J. P., Pratt, D. J., Bibby, G. W., and Rose, J. N.: Distributed Antistokes Ratio Thermometry, in: Optical Fiber Sensors, p. PDS3, OSA, Washington, D.C., doi:10.1364/OFS.1985.PDS3, URL https://www.osapublishing.org/abstract.cfm?uri=OFS-1985-PDS3, 1985.

De Jong, S. A. P., Slingerland, J. D., and Van De Giesen, N. C.: Fiber optic distributed temperature sensing for the determination of air temperature, Atmospheric Measurement Techniques, 8, 335–339, doi:10.5194/amt-8-335-2015, 2015.

Denmead, O. T. and Bradley, E. F.: Flux-Gradient Relationships in a Forest Canopy, in: The Forest-Atmosphere Interaction, edited by Hutchison, B. and Hicks, B., pp. 421–442, Springer Netherlands, Dordrecht, doi:10.1007/978-94-009-5305-5_27, URL http://www.springerlink.com/index/10.1007/978-94-009-5305-5{_}27, 1985.

des Tombe, B., Schilperoort, B., and Bakker, M.: Estimation of Temperature and Associated Uncertainty from Fiber-Optic Raman-Spectrum Distributed Temperature Sensing, Sensors, 20, 2235, doi:10.3390/s20082235, URL https://www.mdpi.com/1424-8220/20/8/2235, 2020.

des Tombe, B. F. and Schilperoort, B.: Python distributed temperature sensing calibration, doi:10.5281/zenodo.3531558, 2019.

des Tombe, B. F., Bakker, M., Schaars, F., and van der Made, K. J.: Estimating Travel Time in Bank Filtration Systems from a Numerical Model Based on DTS Measurements, Groundwater, 56, 288–299, doi:10.1111/gwat.12581, 2018.

des Tombe, B. F., Bakker, M., Smits, F., Schaars, F., and Made, K.: Estimation of the Variation in Specific Discharge Over Large Depth Using Distributed Temperature Sensing (DTS) Measurements of the Heat Pulse Response, Water Resources Research, 55, 811–826, doi:10.1029/2018WR024171, URL https://onlinelibrary.wiley.com/doi/abs/10.1029/2018WR024171, 2019.

Dong, J., Steele-Dunne, S. C., Ochsner, T. E., Hatch, C. E., Sayde, C., Selker, J., Tyler, S., Cosh, M. H., and van de Giesen, N.: Mapping high-resolution soil moisture and properties using distributed temperature sensing data and an adaptive particle batch smoother, Water Resources Research, 52, 7690–7710, doi:10.1002/2016WR019031, URL https://onlinelibrary.wiley.com/doi/10.1002/2016WR019031, 2016.

Douglas, G. C., Pliura, A., Dufour, J., Mertens, P., Jacques, D., Fernandez-Manjares, J., Buiteveld, J., Parnuta, G., Tudoroiu, M., Curnel, Y., Thomasset, M., Jensen, V., Knudsen, M. A., Foffová, E., Chandelier, A., and Steenackers, M.: Common Ash (Fraxinus excelsior L.), in: Forest tree breeding in Europe: Current state-of-the-art and perspectives, edited by Pâques, L. E., pp. 403–462, Springer Netherlands, Dordrecht, doi:10.1007/978-94-007-6146-9_9, URL http://link.springer.com/10.1007/978-94-007-6146-9{_}9, 2013.

Dupont, S. and Patton, E. G.: Momentum and scalar transport within a vegetation canopy following atmospheric stability and seasonal canopy changes: The CHATS experiment, Atmospheric Chemistry and Physics, 12, 5913–5935, doi:10.5194/acp-12-5913-2012, 2012.

Euser, T., Luxemburg, W. M. J., Everson, C. S., Mengistu, M. G., Clulow, A. D., and Bastiaanssen, W. G. M.: A new method to measure Bowen ratios using high-resolution vertical dry and wet bulb temperature profiles, Hydrology and Earth System Sciences, 18, 2021–2032, doi:10.5194/hess-18-2021-2014, 2014.

Farah, S., Anderson, D. G., and Langer, R.: Physical and mechanical properties of PLA, and their functions in widespread applications — A comprehensive review, Advanced Drug Delivery Reviews, 107, 367–392, doi:10.1016/j.addr.2016.06.012, 2016.

Finnigan, J.: Turbulence in Plant Canopies, Annual Review of Fluid Mechanics, 32, 519–571, doi:10.1146/annurev.fluid.32.1.519, URL https://www.annualreviews.org/doi/10.1146/annurev.fluid.32.1.519, 2000.

Fitzjarrald, D. R. and Moore, K. E.: Mechanisms of nocturnal exchange between the rain forest and the atmosphere, Journal of Geophysical Research, 95, 16 839, doi:10.1029/JD095iD10p16839, URL http://doi.wiley.com/10.1029/JD095iD10p16839, 1990.

Fluxnet: History of Fluxnet, URL https://fluxnet.org/about/history/, 2017.

Foken, T.: The energy balance closure problem: an overview, Ecological Applications, 18, 1351–1367, doi:10.1890/06-0922.1, URL http://doi.wiley.com/10.1890/06-0922.1, 2008.

Foken, T., Godecke, M., Mauder, M., Mahrt, L., Amiro, B., and Munger, J.: Post-field quality control, in: Handbook of micrometeorology: A guide for surface flux measurements, edited by Lee, X., pp. 81–108, Kluwer Academic, Dordrecht, 2004.

Fornberg, B.: Generation of finite difference formulas on arbitrarily spaced grids, Mathematics of Computation, 51, 699–699, doi:10.1090/S0025-5718-1988-0935077-0, URL http://www.ams.org/jourcgi/jour-getitem?pii=S0025-5718-1988-0935077-0, 1988.

Frazer, G. W., Canham, C., and Lertzman, K.: Gap Light Analyzer (GLA), Version 2.0: Imaging software to extract canopy structure and gap light transmission indices from true-colour fisheye photographs, users manual and program documentation, Simon Fraser University, Burnaby, British Columbia, and the Institute of Ecosystem Studies, Millbrook, New York, 1999.

Fuchs, M. and Tanner, C. B.: Error analysis of bowen ratios measured by differential psychrometry, Agricultural Meteorology, 7, 329–334, doi:10.1016/0002-1571(70)90027-0, 1970.

Gao, W., Shaw, R. H., and Paw U, K. T.: Observation of organized structure in turbulent flow within and above a forest canopy, Boundary-Layer Meteorology, 47, 349–377, doi:10.1007/BF00122339, URL http://link.springer.com/10.1007/BF00122339, 1989.

Georges, C. and Kaser, G.: Ventilated and unventilated air temperature measurements for glacier-climate studies on a tropical high mountain site, Journal of Geophysical Research: Atmospheres, 107, doi:10.1029/2002JD002503, URL https://onlinelibrary.wiley.com/doi/10.1029/2002JD002503, 2002.

Göckede, M., Thomas, C., Markkanen, T., Mauder, M., Ruppert, J., and Foken, T.: Sensitivity of Lagrangian Stochastic footprints to turbulence statistics, Tellus, Series B: Chemical and Physical Meteorology, 59, 577–586, doi:10.1111/j.1600-0889.2007.00275.x, 2007.

Goulden, M. L., Munger, J. W., Fan, S.-M., Daube, B. C., and Wofsy, S. C.: Measurements of carbon sequestration by long-term eddy covariance: methods and a critical evaluation of accuracy, Global Change Biology, 2, 169–182, doi:10.1111/j.1365-2486.1996.tb00070.x, URL http://doi.wiley.com/10.1111/j.1365-2486.1996.tb00070.x, 1996.

Harrison, R. G. and Wood, C. R.: Ventilation effects on humidity measurements in thermometer screens, Quarterly Journal of the Royal Meteorological Society, 138, 1114–1120, doi:10.1002/qj.985, 2012.

Hartog, A. H.: An Introduction to Distributed Optical Fibre Sensors, CRC Press, Boca Raton, Florida, doi:10.1201/9781315119014, URL https://www.taylorfrancis.com/books/9781482259582, 2017.

Hausfather, Z., Drake, H. F., Abbott, T., and Schmidt, G. A.: Evaluating the Performance of Past Climate Model Projections, Geophysical Research Letters, 47, doi:10.1029/2019GL085378, URL https://onlinelibrary.wiley.com/doi/abs/10.1029/2019GL085378, 2020.

Hausner, M. B., Suárez, F., Glander, K. E., van de Giesen, N., Selker, J. S., and Tyler, S. W.: Calibrating Single-Ended Fiber-Optic Raman Spectra Distributed Temperature Sensing Data, Sensors, 11, 10 859–10 879, doi:10.3390/s111110859, URL http://www.mdpi.com/1424-8220/11/11/10859, 2011.

Heusinkveld, B. G., Jacobs, A. F., Holtslag, A. A., and Berkowicz, S. M.: Surface energy balance closure in an arid region: Role of soil heat flux, Agricultural and Forest Meteorology, doi:10.1016/j.agrformet.2003.09.005, 2004.

Heusinkveld, V. W., Antoon van Hooft, J., Schilperoort, B., Baas, P., ten Veldhuis, M., and van de Wiel, B. J.: Towards a physics-based understanding of fruit frost protection using wind machines, Agricultural and Forest Meteorology, 282-283, 107 868, doi:10.1016/j.agrformet.2019.107868, URL https://linkinghub.elsevier.com/retrieve/pii/S0168192319304848, 2020.

Hilgersom, K., van Emmerik, T., Solcerova, A., Berghuijs, W., Selker, J., and van de Giesen, N.: Practical considerations for enhanced-resolution coil-wrapped distributed temperature sensing, Geoscientific Instrumentation, Methods and Data Systems, 5, 151–162, doi:10.5194/gi-5-151-2016, 2016.

Holtslag, A. A. M. and De Bruin, H. A. R.: Applied Modeling of the Nighttime Surface Energy Balance over Land, Journal of Applied Meteorology, 27, 689–704, doi:10.1175/1520-0450(1988)027<0689:AMOTNS>2.0.CO;2, URL http://journals.ametsoc.org/doi/10.1175/1520-0450(1988)027{%}3C0689:AMOTNS{%}3E2.0.CO;2, 1988.

Irmak, S., Kilic, A., and Chatterjee, S.: On the Equality Assumption of Latent and Sensible Heat Energy Transfer Coefficients of the Bowen Ratio Theory for Evapotranspiration Estimations: Another Look at the Potential Causes of Inequalities, Climate, 2, 181–205, doi:10.3390/cli2030181, 2014.

Izett, J. G., Schilperoort, B., Coenders-Gerrits, M., Baas, P., Bosveld, F. C., and van de Wiel, B. J. H.: Missed Fog?, Boundary-Layer Meteorology, 173, 289–309, doi:10.1007/s10546-019-00462-3, URL https://doi.org/10.1007/s10546-019-00462-3, 2019.

J. O. Payero, C. M. U. Neale, J. L. Wright, R. G. Allen, Payero, J. O., Neale, C. M. U., Wright, J. L., and Allen, R. G.: Guidelines for validating Bowen ratio data, Transactions of the ASAE, 46, 1051–1060, doi:10.13031/2013.13967, 2003.

Jansen, J., Stive, P. M., van de Giesen, N., Tyler, S., Steele-Dunne, S. C., and Williamson, L.: Estimating soil heat flux using Distributed Temperature Sensing, GRACE, Remote Sensing and Ground-based Methods in Multi-Scale Hydrology, pp. 140–144, 2011.

Jiménez-Rodríguez, C. D., Coenders-Gerrits, M., Schilperoort, B., González-Angarita, A., and Savenije, H.: Vapor plumes in a tropical wet forest: spotting the invisible evaporation, Hydrology and Earth System Sciences Discussions, 2020, 1–20, doi:10.5194/hess-2020-14, URL https://www.hydrol-earth-syst-sci-discuss.net/hess-2020-14/, 2020a.

Jiménez-Rodríguez, C. D., Coenders-Gerrits, M., Wenninger, J., Gonzalez-Angarita, A., and Savenije, H.: Contribution of understory evaporation in a tropical wet forest during the dry season, Hydrology and Earth System Sciences, 24, 2179–2206, doi:10.5194/hess-24-2179-2020, URL https://hess.copernicus.org/articles/24/2179/2020/, 2020b.

Jiménez-Rodríguez, C. D., Coenders-Gerrits, M., Wenninger, J., Gonzalez-Angarita, A., and Savenije, H.: Contribution of understory evaporation in a tropical wet forest during the dry season, Hydrology and Earth System Sciences, 24, 2179–2206, doi:10.5194/hess-24-2179-2020, URL https://hess.copernicus.org/articles/24/2179/2020/, 2020c.

Jocher, G., Ottosson Löfvenius, M., De Simon, G., Hörnlund, T., Linder, S., Lundmark, T., Marshall, J., Nilsson, M. B., Näsholm, T., Tarvainen, L., Öquist, M., and Peichl, M.: Apparent winter CO2 uptake by a boreal forest due to decoupling, Agricultural and Forest Meteorology, 232, 23–34, doi:10.1016/j.agrformet.2016.08.002, URL http://dx.doi.org/10.1016/j.agrformet.2016.08.002, 2017.

Jocher, G., Marshall, J., Nilsson, M. B., Linder, S., De Simon, G., Hörnlund, T., Lundmark, T., Näsholm, T., Ottosson Löfvenius, M., Tarvainen, L., Wallin, G., and Peichl, M.: Impact of Canopy Decoupling and Subcanopy Advection on the Annual Carbon Balance of a Boreal Scots Pine Forest as Derived From Eddy Covariance, Journal of Geophysical Research: Biogeosciences, 123, 303–325, doi:10.1002/2017JG003988, 2018.

Jocher, G., Fischer, M., Šigut, L., Pavelka, M., Sedlák, P., and Katul, G.: Assessing decoupling of above and below canopy air masses at a Norway spruce stand in complex terrain, Agricultural and Forest Meteorology, 294, 108 149, doi:10.1016/j.agrformet.2020.108149, URL https://linkinghub.elsevier.com/retrieve/pii/S0168192320302513, 2020.

Kaimal, J. C. and Finnigan, J. J.: Atmospheric boundary layer flows: their structure and measurement, Oxford University Press, New York, 1994.

Katul, G., Goltz, S. M., Hsieh, C. I., Cheng, Y., Mowry, F., and Sigmon, J.: Estimation of surface heat and momentum fluxes using the flux-variance method above uniform and non-uniform terrain, Boundary-Layer Meteorology, 74, 237–260, doi:10.1007/BF00712120, 1995.

Knap, W.: Basic and other measurements of radiation at station Cabauw (2017-06), doi:10.1594/PANGAEA.877434, URL https://doi.org/10.1594/PANGAEA.877434, 2017.

Koutsoyiannis, D.: Clausius-Clapeyron equation and saturation vapour pressure: simple theory reconciled with practice, European Journal of Physics, 33, 295–305, doi:10.1088/0143-0807/33/2/295, 2012.

Kundu, P. K., Cohen, I. M., and Dowling, D. R.: Turbulence, in: Fluid Mechanics, pp. 603–697, Elsevier, doi:10.1016/B978-0-12-405935-1.00012-5, URL https://linkinghub.elsevier.com/retrieve/pii/B9780124059351000125, 2016.

Lapo, K., Freundorfer, A., Pfister, L., Schneider, J., Selker, J., and Thomas, C.: Distributed observations of wind direction using microstructures attached to actively heated fiber-optic cables, Atmospheric Measurement Techniques, 13, 1563–1573, doi:10.5194/amt-13-1563-2020, URL https://www.atmos-meas-tech-discuss.net/amt-2019-188/https://www.atmos-meas-tech.net/13/1563/2020/, 2020.

Launiainen, S., Vesala, T., MöLder, M., Mammarella, I., Smolander, S., Rannik, Ü., Kolari, P., Hari, P., Lindroth, A., and G. Katul, G.: Vertical variability and effect of stability on turbulence characteristics down to the floor of a pine forest, Tellus B: Chemical and Physical Meteorology, 59, 919–936, doi:10.1111/j.1600-0889.2007.00313.x, URL https://www.tandfonline.com/doi/full/10.1111/j.1600-0889.2007.00313.x, 2007.

LI-COR Inc.: EddyPro® Version 6.2 [Computer Software], 2016.

Loeb, N. G., Wielicki, B. A., Doelling, D. R., Smith, G. L., Keyes, D. F., Kato, S., Manalo-Smith, N., and Wong, T.: Toward optimal closure of the Earth's top-of-atmosphere radiation budget, Journal of Climate, 22, 748–766, doi:10.1175/2008JCLI2637.1, 2009.

Lorenz, E. N.: Three approaches to atmospheric predictability, Bulletin of the American Meteorological Society, 50, 345–349, 1969.

Mahrt, L.: Weak-wind mesoscale meandering in the nocturnal boundary layer, Environmental Fluid Mechanics, 7, 331–347, doi:10.1007/s10652-007-9024-9, URL http://link.springer.com/10.1007/s10652-007-9024-9, 2007.

Mauder, M. and Foken, T.: Impact of post-field data processing on eddy covariance flux estimates and energy balance closure, Meteorologische Zeitschrift, 15, 597–609, doi:10.1127/0941-2948/2006/0167, URL http://www.schweizerbart.de/papers/metz/detail/15/55217/Impact{_}of{_}post{_}field{_}data{_}processing{_}on{_}eddy{_}covar?af=crossref, 2006.

McCaughey, J. H. and Saxton, W. L.: Energy balance storage terms in a mixed forest, Agricultural and Forest Meteorology, 44, 1–18, doi:10.1016/0168-1923(88)90029-9, 1988.

Michiles, A. A. and Gielow, R.: Above-ground thermal energy storage rates, trunk heat fluxes and surface energy balance in a central Amazonian rainforest, Agricultural and Forest Meteorology, 148, 917–930, doi:10.1016/j.agrformet.2008.01.001, 2008.

Monna, W. and Bosveld, F.: In higher spheres: 40 years of observations at the Cabauw Site, Royal Netherlands Meteorological Institute, De Bilt, 2013.

Nadkarni, N., Parker, G., Rinker, H., and Jarzen, D.: The Nature of Forest Canopies, in: Forest Canopies, edited by Lowman, M. and Rinker, H., chap. Chapter 1, pp. 3–23, Academic Press, San Diego, 2nd edn., URL https://www.elsevier.com/books/forest-canopies/lowman/978-0-12-457553-0, 2004.

Newsom, R. K. and Banta, R. M.: Shear-Flow Instability in the Stable Nocturnal Boundary Layer as Observed by Doppler Lidar during CASES-99, Journal of the Atmospheric Sciences, 60, 16–33, doi:10.1175/1520-0469(2003)060<0016:SFIITS>2.0.CO;2, URL http://journals.ametsoc.org/doi/10.1175/1520-0469(2003)060{%}3C0016:SFIITS{%}3E2.0.CO;2, 2003.

Ochsner, T. E., Horton, R., and Ren, T.: A New Perspective on Soil Thermal Properties, Soil Science Society of America Journal, 65, 1641–1647, doi:10.2136/sssaj2001.1641, URL http://doi.wiley.com/10.2136/sssaj2001.1641, 2001.

Oliphant, A. J., Grimmond, C. S. B., Zutter, H. N., Schmid, H. P., Su, H. B., Scott, S. L., Offerle, B., Randolph, J. C., and Ehman, J.: Heat storage and energy balance fluxes for a temperate deciduous forest, Agricultural and Forest Meteorology, 126, 185–201, doi:10.1016/j.agrformet.2004.07.003, 2004.

Pal Arya, S.: Introduction to Micrometeorology, Academic Press, San Diego, California, 1988.

Papale, D., Reichstein, M., Aubinet, M., Canfora, E., Bernhofer, C., Kutsch, W., Longdoz, B., Rambal, S., Valentini, R., Vesala, T., and Yakir, D.: Towards a standardized processing of Net Ecosystem Exchange measured with eddy covariance technique: Algorithms and uncertainty estimation, Biogeosciences, 3, 571–583, doi:10.5194/bg-3-571-2006, 2006.

Parker, G.: Structure and Microclimate of Forest Canopies, in: Forest Canopies, edited by Lowman, M. and Nadkarni, N., chap. Chapter 4, pp. 73–106, Academic Press, San Diego, 1st edn., 1995.

Patton, E. G., Horst, T. W., Sullivan, P. P., Lenschow, D. H., Oncley, S. P., Brown, W. O. J., Burns, S. P., Guenther, A. B., Held, A., Karl, T., Mayor, S. D., Rizzo, L. V., Spuler, S. M., Sun, J., Turnipseed, A. A., Allwine, E. J., Edburg, S. L., Lamb, B. K., Avissar, R., Calhoun, R. J., Kleissl, J., Massman, W. J., Paw U, K. T., and Weil, J. C.: The Canopy Horizontal Array Turbulence Study, Bulletin of the American Meteorological Society, 92, 593–611, doi:10.1175/2010BAMS2614.1, URL https://journals.ametsoc.org/bams/article/92/5/593/106957/The-Canopy-Horizontal-Array-Turbulence-Study, 2011.

Peltola, O., Lapo, K., Martinkauppi, I., O'Connor, E., Thomas, C. K., and Vesala, T.: Suitability of fiber-optic distributed temperature sensing to reveal mixing processes and higher-order moments at the forest-air interface, Atmospheric Measurement Techniques Discussions, 2020, 1–31, URL https://amt.copernicus.org/preprints/amt-2020-260/, 2020.

Petenko, I., Argentini, S., Casasanta, G., Kallistratova, M., Sozzi, R., and Viola, A.: Wavelike Structures in the Turbulent Layer During the Morning Development of Convection at Dome C, Antarctica, Boundary-Layer Meteorology, 161, 289–307, doi:10.1007/s10546-016-0173-6, 2016.

Petenko, I., Argentini, S., Casasanta, G., Genthon, C., and Kallistratova, M.: Stable Surface-Based Turbulent Layer During the Polar Winter at Dome C, Antarctica: Sodar and In Situ Observations, Boundary-Layer Meteorology, 171, 101–128, doi:10.1007/s10546-018-0419-6, URL https://doi.org/10.1007/s10546-018-0419-6, 2019.

Popinet, S.: A quadtree-adaptive multigrid solver for the Serre–Green–Naghdi equations, Journal of Computational Physics, 302, 336–358, doi:10.1016/j.jcp.2015.09.009, URL https://linkinghub.elsevier.com/retrieve/pii/S0021999115005902, 2015.

Prusa Research: Prusament PLA by Prusa Polymers, Tech. rep., Prusa Research, Prague, 2018.

Prusa Research: Prusament PETG by Prusa Polymers, Tech. rep., Prusa Research a.s., Prague, Czech Republic, 2020.

Raman, C. V.: A new radiation, Indian Journal of Physics, 2, 387–398, 1928.

Raupach, M. R.: Anomalies in flux-gradient relationships over forest, Boundary-Layer Meteorology, 16, 467–486, doi:10.1007/BF03163564, URL http://link.springer.com/10.1007/BF03163564, 1979.

Raupach, M. R., Finnigan, J. J., and Brunei, Y.: Coherent eddies and turbulence in vegetation canopies: The mixing-layer analogy, Boundary-Layer Meteorology, 78, 351–382, doi:10.1007/BF00120941, URL http://link.springer.com/10.1007/BF00120941, 1996.

Rigid.ink: PETG data shet, Tech. rep., rigid.ink, Wetherby, UK, URL http://devel.lulzbot.com/filament/Rigid{_}Ink/PETGDATASHEET.pdf, 2017.

Santer, B. D., Po-Chedley, S., Mears, C., Fyfe, J. C., Gillett, N., Fu, Q., Painter, J. F., Solomon, S., Steiner, A. K., Wentz, F. J., Zelinka, M. D., and Zou, C.-Z.: Using Climate Model Simulations to Constrain Observations, Journal of Climate, pp. 1–59, doi:10.1175/JCLI-D-20-0768.1, URL https://journals.ametsoc.org/view/journals/clim/aop/JCLI-D-20-0768.1/JCLI-D-20-0768.1.xml, 2021.

Sayde, C., Gregory, C., Gil-Rodriguez, M., Tufillaro, N., Tyler, S., van de Giesen, N., English, M., Cuenca, R., and Selker, J. S.: Feasibility of soil moisture monitoring with heated fiber optics, Water Resources Research, 46, doi:10.1029/2009WR007846, URL http://doi.wiley.com/10.1029/2009WR007846, 2010.

Sayde, C., Thomas, C. K., Wagner, J., and Selker, J.: High-resolution wind speed measurements using actively heated fiber optics, Geophysical Research Letters, 42, 10 064–10 073, doi:10.1002/2015GL066729, 2015.

Schilperoort, B., Coenders-Gerrits, M., Luxemburg, W., Rodríguez, C. J., Vaca, C. C., and Savenije, H.: Technical note: Using distributed temperature sensing for Bowen ratio evaporation measurements, Hydrology and Earth System Sciences, 22, 819–830, doi:10.5194/hess-22-819-2018, 2018.

Schilperoort, B., Rodríguez, C. J., and Coenders-Gerrits, M.: Animated DTS temperature profiles Speulderbos forest, doi:10.5281/ZENODO.3048116, URL https://zenodo.org/record/3048116, 2019.

Schilperoort, B., Coenders-Gerrits, M., Jiménez Rodriguez, C., van der Tol, C., van de Wiel, B., and Savenije, H.: Decoupling of a Douglas fir canopy: a look into the subcanopy with continuous vertical temperature profiles, Biogeosciences Discussions, 2020, 1–25, doi:10.5194/bg-2020-216, URL https://bg.copernicus.org/preprints/bg-2020-216/, 2020.

Schmid, M., Pautasso, M., and Holdenrieder, O.: Ecological consequences of Douglas fir (Pseudotsuga menziesii) cultivation in Europe, European Journal of Forest Research, 133, 13–29, doi:10.1007/s10342-013-0745-7, 2014.

Selker, F. and Selker, J.: Investigating Water Movement Within and Near Wells Using Active Point Heating and Fiber Optic Distributed Temperature Sensing, Sensors, 18, 1023, doi:10.3390/s18041023, URL http://www.mdpi.com/1424-8220/18/4/1023, 2018.

Selker, J. S., Thévenaz, L., Huwald, H., Mallet, A., Luxemburg, W., Van De Giesen, N., Stejskal, M., Zeman, J., Westhoff, M., and Parlange, M. B.: Distributed fiber-optic temperature sensing for hydrologic systems, Water Resources Research, 42, 1–8, doi:10.1029/2006WR005326, 2006.

Shehata, M., Heitman, J., Ishak, J., and Sayde, C.: High-Resolution Measurement of Soil Thermal Properties and Moisture Content Using a Novel Heated Fiber Optics Approach, Water Resources Research, 56, doi:10.1029/2019WR025204, URL https://onlinelibrary.wiley.com/doi/10.1029/2019WR025204, 2020.

Silixa Ltd: ULTIMA™ DTS, URL http://silixa.com/technology/ultima-dts/, 2017.

Sluijter, R.: De Bosatlas van het klimaat, Noordhoff Uitgevers, Groningen, 2011.

Smolen, J. J. and van der Spek, A.: Distributed Temperature Sensing A DTS Primer for Oil & Gas Production, Shell International Exploration and Production, The Hague, The Netherlands, p. 97, 2003.

Staebler, R. M. and Fitzjarrald, D. R.: Observing subcanopy CO2 advection, Agricultural and Forest Meteorology, 122, 139–156, doi:10.1016/j.agrformet.2003.09.011, 2004.

Stafford, B.: pysolar, doi:10.5281/ZENODO.1461066, URL https://zenodo.org/record/1461066, 2018.

Stannard, D. I.: A Theoretically Based Determination of Bowen-ratio Fetch Requirements, Boundary-Layer Meteorology, 83, 375–406, doi:10.1023/A:1000286829849, URL https://doi.org/10.1023/A:1000286829849http://link.springer.com/article/10.1023/A:1000286829849http://link.springer.com/10.1023/A:1000286829849, 1997.

Steele-Dunne, S. C., Rutten, M. M., Krzeminska, D. M., Hausner, M., Tyler, S. W., Selker, J., Bogaard, T. A., and Van De Giesen, N. C.: Feasibility of soil moisture estimation using passive distributed temperature sensing, Water Resources Research, 46, 1–12, doi:10.1029/2009WR008272, 2010.

Stricker, H. and Brutsaert, W.: Actual evapotranspiration over a summer period in the "Hupsel catchment", Journal of Hydrology, 39, 139–157, doi:10.1016/0022-1694(78)90119-1, 1978.

Striegl, A. M. and Loheide II, S. P.: Heated Distributed Temperature Sensing for Field Scale Soil Moisture Monitoring, Ground Water, 50, 340–347, doi:10.1111/j.1745-6584.2012.00928.x, URL https://onlinelibrary.wiley.com/doi/10.1111/j.1745-6584.2012.00928.x, 2012.

Stull, R.: Wet-Bulb Temperature from Relative Humidity and Air Temperature, Journal of Applied Meteorology and Climatology, 50, 2267–2269, doi:10.1175/JAMC-D-11-0143.1, URL https://journals.ametsoc.org/view/journals/apme/50/11/jamc-d-11-0143.1.xml, 2011.

Stull, R.: Practical Meteorology - An Algebra-based Survey of Atmospheric Science, Department of Earth, Ocean & Atmospheric Sciences, University of British Columbia, Vancouver, BC, doi:10.14288/1.0300441, 2015.

Stull, R. B.: An Introduction to Boundary Layer Meteorology, Kluwer Academic Publishers, Dordrecht, 1988.

Taylor, C.: Finite Difference Coefficients Calculator, URL https://web.media.mit.edu/{~}crtaylor/calculator.html, 2016.

Thomas, C. K., Kennedy, A. M., Selker, J. S., Moretti, A., Schroth, M. H., Smoot, A. R., Tufillaro, N. B., and Zeeman, M. J.: High-Resolution Fibre-Optic Temperature Sensing: A New Tool to Study the Two-Dimensional Structure of Atmospheric Surface-Layer Flow, Boundary-Layer Meteorology, 142, 177–192, doi:10.1007/s10546-011-9672-7, 2012.

Thomas, C. K., Martin, J. G., Law, B. E., and Davis, K.: Toward biologically meaningful net carbon exchange estimates for tall, dense canopies: Multi-level eddy covariance observations and canopy coupling regimes in a mature Douglas-fir forest in Oregon, Agricultural and Forest Meteorology, 173, 14–27, doi:10.1016/j.agrformet.2013.01.001, URL http://www.sciencedirect.com/science/article/pii/S0168192313000051, 2013.

Thomas, C. K., Serafimovich, A., Siebicke, L., Gerken, T., and Foken, T.: Coherent Structures and Flux Coupling, in: Energy and Matter Fluxes of a Spruce Forest Ecosystem, pp. 113–135, Springer International Publishing, doi:10.1007/978-3-319-49389-3_6, 2017.

Thorpe, A. J., Hoskins, B. J., and Innocentini, V.: The parcel method in a baroclinic atmosphere, doi:10.1175/1520-0469(1989)046<1274:TPMIAB>2.0.CO;2, 1989.

Trenberth, K. E., Fasullo, J. T., and Kiehl, J.: Earth's global energy budget, Bulletin of the American Meteorological Society, 90, 311–323, doi:10.1175/2008BAMS2634.1, 2009.

van de Giesen, N., Steele-Dunne, S. C., Jansen, J., Hoes, O., Hausner, M. B., Tyler, S., and Selker, J.: Double-Ended Calibration of Fiber-Optic Raman Spectra Distributed Temperature Sensing Data, Sensors, 12, 5471–5485, doi:10.3390/s120505471, URL http://www.mdpi.com/1424-8220/12/5/5471, 2012.

Van de Wiel, B. J. H., Moene, A. F., Hartogensis, O. K., De Bruin, H. A. R., and Holtslag, A. A. M.: Intermittent Turbulence in the Stable Boundary Layer over Land. Part III: A Classification for Observations during CASES-99, Journal of the Atmospheric Sciences, 60, 2509–2522, doi:10.1175/1520-0469(2003)060<2509:ITITSB>2.0.CO;2, URL http://journals.ametsoc.org/doi/10.1175/1520-0469(2003)060{%}3C2509:ITITSB{%}3E2.0.CO;2, 2003.

Van de Wiel, B. J. H., Moene, A. F., and Jonker, H. J. J.: The Cessation of Continuous Turbulence as Precursor of the Very Stable Nocturnal Boundary Layer, Journal of the Atmospheric Sciences, 69, 3097–3115, doi:10.1175/JAS-D-12-064.1, URL https://journals.ametsoc.org/doi/10.1175/JAS-D-12-064.1, 2012a.

Van de Wiel, B. J. H., Moene, A. F., Jonker, H. J. J., Baas, P., Basu, S., Donda, J. M. M., Sun, J., and Holtslag, A. A. M.: The Minimum Wind Speed for Sustainable Turbulence in the Nocturnal Boundary Layer, Journal of the Atmospheric Sciences, 69, 3116–3127, doi:10.1175/JAS-D-12-0107.1, URL https://journals.ametsoc.org/doi/10.1175/JAS-D-12-0107.1, 2012b.

van de Wiel, B. J. H., Vignon, E., Baas, P., van Hooijdonk, I. G. S., van der Linden, S. J. A., van Hooft, J., Bosveld, F. C., de Roode, S. R., Moene, A. F., and Genthon, C.: Regime Transitions in Near-Surface Temperature Inversions: A Conceptual Model, Journal of the Atmospheric Sciences, 74, 1057–1073, doi:10.1175/JAS-D-16-0180.1, URL https://doi.org/10.1175/JAS-D-16-0180.1, 2017.

van der Linden, S., Kruis, M. T., Hartogensis, O., Moene, A. F., Bosveld, F. C., and van de Wiel, B. J. H.: Heat Transfer through Grass: A Diffusive Approach, Boundary-Layer Meteorology (under review), 2021.

van der Linden, S. J., van de Wiel, B. J., Petenko, I., van Heerwaarden, C. C., Baas, P., and Jonker, H. J.: A businger mechanism for intermittent bursting in the stable boundary layer, Journal of the Atmospheric Sciences, 77, 3343–3360, doi:10.1175/JAS-D-19-0309.1, 2020.

van der Tol, C.: Validation of remote sensing of bare soil ground heat flux, Remote Sensing of Environment, 121, 275–286, doi:10.1016/j.rse.2012.02.009, 2012.

van Hooft, A. and Schilperoort, B.: Temperature-gradient sharpening in a canopy, URL http://www.basilisk.fr/sandbox/Antoonvh/canopy.c, 2021.

van Ramshorst, J. G. V., Coenders-Gerrits, M., Schilperoort, B., van de Wiel, B. J. H., Izett, J. G., Selker, J. S., Higgins, C. W., Savenije, H. H. G., and van de Giesen, N. C.: Wind speed measurements using distributed fiber optics: a windtunnel study, Atmospheric Measurement Techniques Discussions, pp. 1–21, doi:10.5194/amt-2019-63, 2019.

van Wijk, W. and de Vries, D.: Periodic temperature variations in a homogeneous soil, in: Physics of plant environment, pp. 102–143, North-Holland Publ. Co., Amsterdam, 1963.

Verhoef, A.: Remote estimation of thermal inertia and soil heat flux for bare soil, Agricultural and Forest Meteorology, 123, 221–236, doi:10.1016/j.agrformet.2003.11.005, URL https://linkinghub.elsevier.com/retrieve/pii/S016819230300279X, 2004.

Vuik, C., van Beek, P., Vermolen, F., and van Kan, J.: Numerical methods for ordinary differential equations., VSSD, Delft, 2007.

Westhoff, M. C., Savenije, H. H. G., Luxemburg, W. M. J. ., Stelling, G. S., van de Giesen, N. C., Selker, J. S., Pfister, L., and Uhlenbrook, S.: A distributed stream temperature model using high resolution temperature observations, Hydrology and Earth System Sciences, 11, 1469–1480, doi:10.5194/hess-11-1469-2007, 2007.

Wilson, K.: Energy balance closure at FLUXNET sites, Agricultural and Forest Meteorology, 113, 223–243, doi:10.1016/S0168-1923(02)00109-0, 2002.

Winter, S., Höfler, J., Michel, A. K., Böck, A., and Ankerst, D. P.: Association of tree and plot characteristics with microhabitat formation in European beech and Douglas-fir forests, European Journal of Forest Research, 134, 335–347, doi:10.1007/s10342-014-0855-x, 2015.

Wu, R., Martin, V., McKenzie, J., Broda, S., Bussière, B., Aubertin, M., and Kurylyk, B. L.: Laboratory-scale assessment of a capillary barrier using fibre optic distributed temperature sensing (FO-DTS), Canadian Geotechnical Journal, 57, 115–126, doi:10.1139/cgj-2018-0283, URL http://www.nrcresearchpress.com/doi/10.1139/cgj-2018-0283, 2020.

Wu, R., Lamontagne-Hallé, P., and McKenzie, J. M.: Uncertainties in Measuring Soil Moisture Content with Actively Heated Fiber-Optic Distributed Temperature Sensing, Sensors, 21, 3723, doi:10.3390/s21113723, URL https://www.mdpi.com/1424-8220/21/11/3723, 2021.

Xie, X., Lu, Y., Ren, T., and Horton, R.: Soil temperature estimation with the harmonic method is affected by thermal diffusivity parameterization, Geoderma, 353, 97–103, doi:10.1016/j.geoderma.2019.06.029, URL https://linkinghub.elsevier.com/retrieve/pii/S001670611930268X, 2019.

Zeeman, M. J., Selker, J. S., and Thomas, C. K.: Near-Surface Motion in the Nocturnal, Stable Boundary Layer Observed with Fibre-Optic Distributed Temperature Sensing, Boundary-Layer Meteorology, 154, 189–205, doi:10.1007/s10546-014-9972-9, URL http://dx.doi.org/10.1007/s10546-014-9972-9, 2015.

Acknowledgments

Allereerst Miriam, bedankt voor je belegeiding al die jaren en het vertrouwen dat je in mij en mijn vaardigheden hebt gehad. Ik heb erg genoten van de vrijheid die je mij gaf in het uitvoeren van het onderzoek en het verkennen van al de mogelijke paden die het onderzoek kon nemen. Huub, ook al kon je niet altijd inhoudelijk helpen stond je altijd klaar om razensnel feedback te geven. Bas van de Wiel, ondanks dat ik niet jouw promovendus was stond je altijd open voor diepgaande discussies en het controleren van mijn geschreven stukken. Jouw enthousiasme was altijd erg motiverend, en dankzij jouw hulp en kennis hebben de publicaties en mijn thesis een hoger niveau bereikt.

César, it was a joy to work together with you in the project. Your knowledge of fieldwork and the forests was invaluable, and the regular drives to and from the Veluwe were always enjoyable. You taught me a lot about forests, fieldwork, and life in general!

Boran, thank you for livening up the department and for always being up to join for the social events. Jerom, bedankt voor alle goede tijden op het kantoor, en voor het aandringen op de Mustang cabrio in de Rockies. Die reis was onvergetelijk! Anna, it was always great fun to spend time with you, be it in the office, NOLA, the Mekelpark, or at Locus. Thanks for the great memories! Rolf, thanks for showing me how to make the most of conferences (and the flight to them)! David Steffelbauer, thank you for the great time, both in Delft as well as Graz and the Austrian vineyards! Bas des Tombe, het was altijd een plezier om met jou samen te werken aan de Python package, en ook een hele goede leerervaring.

Lydia, Betty en Tamara, bedankt voor het regelen van alle logistiek en papierwerk, en natuurlijk de onmisbare snacks op de donderdagmiddag! Antoon, Jonathan, and Steven, it was great to cooperate and go on fieldwork with you, and enlightening to discuss ideas across our different departments. Thom Boogaard, bedankt voor het organiseren van de apparatuur en voor de regelmatige opruimacties om te zorgen dat het grote opslaghok begaanbaar blijft.

Olivier, Martin, Remko, Mark, Ruud, Dirk, Wim, Chelsea, Schuyler, Banafsheh, Anjana, and all other colleagues of WRM; thank you for the lunch chats, casual conversations and lively post-colloquium discussions. Armand, Mohammed, Patricia & Jane, bedankt voor het beheren van het lab en voor het draaiende houden van de veldwerkbus. Zonder de blauwe bus was het vele veldwerk niet mogelijk geweest. To all the shorter term visitors from abroad; João, Erika, Rosa, David, Livia, Hubert, and Henry, your presence made the 4^{th} floor a more interesting place to be!

Ties, Paul, Matt, Monica, Juanco, Mike, Jeroen, Antonella, Carina, Su, and everyone else of who tagged along, thank you for the great Thursday evenings, especially when braving the December cold outside with Glühwein. The covid years would have been a lot more difficult without you! Robert & Jessica, thank you for tolerating the bluegrass on our music nights, and for joining the great Czech 'rafting' adventure! Anna, Laurène, Jerom, and Gaby, thanks for the good times in 4.96 and for putting up with my tendency to chat a lot while doing work.

Johanna, while you were not there for most of the journey, it was great to share the end of it with you, and to have your continuing support.

Mam en pap, bedankt voor jullie steun al die jaren, zowel tijdens mijn promotie als de jaren er voor.

Curriculum Vitæ

Bart Schilperoort

11 April 1992	Born in Leidschendam, the Netherlands.
2003–2009	Gymnasium Adelbert College, Wassenaar
2009–2014	Bachelor of Science in Civil Engineering Technische Universiteit Delft
2016–2016	Master of Science in Civil Engineering Technische Universiteit Delft
2016–present	Doctoral Candidate Technische Universiteit Delft
September 2020 – September 2021	Post-doc researcher Technische Universiteit Delft

List of Publications

First author, peer reviewed

- **Bart Schilperoort**, Miriam Coenders-Gerrits, César Jiménez-Rodríguez, Antoon van Hooft, Bas van de Wiel, Hubert Savenije, *Detecting nighttime inversions in the interior of a Douglas fir canopy*, Agriculture and Forest Meteorology, *under review* (2021).
- **Bart Schilperoort**, Miriam Coenders-Gerrits, César Jiménez-Rodríguez, Christiaan van der Tol, Bas van de Wiel, Hubert Savenije, *Decoupling of a Douglas fir canopy: a look into the subcanopy with continuous vertical temperature profiles*, Biogeosciences **17**, 6426–6439 (2020).
- **Bart Schilperoort**, Miriam Coenders-Gerrits, Willem Luxemburg, César Jiménez-Rodríguez, César Cisneros Vaca, Hubert Savenije, *Technical note: Using distributed temperature sensing for Bowen ratio evaporation measurements*, Hydrology and Earth System Sciences **22**, 819–830 (2018).

Co-author, peer reviewed

- Eva Stache, **Bart Schilperoort**, Marc Ottelé, Henk Jonkers, *Comparative analysis in thermal behaviour of common urban building materials and vegetation and consequences for urban heat island effect*, Building and the Environment, 108489 (2021)
- César Jiménez-Rodríguez, Miriam Coenders-Gerrits, **Bart Schilperoort**, Adriana González-Angarita, Hubert Savenije, *Vapor plumes in a tropical wet forest: spotting the invisible evaporation* , Hydrol. Earth Syst. Sci. Discuss., **25**, 619–635 (2021).
- Robert Law, Poul Christoffersen, Bryn Hubbard, Samuel H. Doyle, Thomas R. Chudley, Charlotte M. Schoonman, Marion Bougamont, Bas des Tombe, **Bart Schilperoort**, Cedric Kechavarzi, Adam Booth, Tun Jan Young, *Thermodynamics of a fast-moving Greenlandic outlet glacier revealed by fiber-optic distributed temperature sensing*, Science Advances **7(20)** (2021)
- Justus G. V. van Ramshorst, Miriam Coenders-Gerrits, **Bart Schilperoort**, Bas J. H. van de Wiel, Jonathan G. Izett, John S. Selker, Chad W. Higgins, Hubert H. G. Savenije, Nick C. van de Giesen, *Revisiting wind speed measurements using actively heated fiber optics: a wind tunnel study*, Atmospheric Measurement Techniques **13**, 5423–5439 (2020).
- Bas des Tombe, **Bart Schilperoort**, Mark Bakker, *Estimation of Temperature and Associated Uncertainty from Fiber-Optic Raman-Spectrum Distributed Temperature Sensing*, Sensors **20(8)**, 2235 (2020).
- Vincent W.J. Heusinkveld, J. Antoon van Hooft, **Bart Schilperoort**, Peter Baas, Bas J.H. van de Wiel, *Towards a physics-based understanding of fruit frost protection using wind machines*, Agricultural and Forest Meteorology **282**, 107868 (2020).
- Jonathan G. Izett, **Bart Schilperoort**, Miriam Coenders-Gerrits, Peter Baas, Fred C. Bosveld, Bas J.H. van de Wiel, *Missed Fog? – On the Potential of Obtaining Observations at Increased Resolution During Shallow Fog Events*, Boundary-Layer Meteorology **173**, 289–309 (2019).

Book chapters

- Miriam Coenders-Gerrits, **Bart Schilperoort**, César Jiménez-Rodríguez, *Evaporative Processes on Vegetation: An Inside Look*, In: Van Stan, II J., Gutmann E., Friesen J. (eds), *Precipitation Partitioning by Vegetation*, Springer, Cham., 35–48 (2020).

- Miriam Coenders-Gerrits, **Bart Schilperoort**, César Jiménez-Rodríguez, *Key Questions on the Evaporation and Transport of Intercepted Precipitation*, In: Van Stan, II J., Gutmann E., Friesen J. (eds), *Precipitation Partitioning by Vegetation*, Springer, Cham., 269–280 (2020).

Software packages

- Bas des Tombe, **Bart Schilperoort**, *'dtscalibration' Python package for calibrating distributed temperature sensing measurements*, Zenodo (2020).

Measurement Data

- **Bart Schilperoort**, César Jiménez-Rodríguez, Christiaan van der Tol, Murat Ucer, Miriam Coenders-Gerrits, *Speulderbos turbulence and temperature profile measurements*, 4TU Research Data (2020)

- Jonathan Izett, **Bart Schilperoort**, Miriam Coenders-Gerrits, Bas J.A. van de Wiel, *High-Resolution DTS Temperature Measurements During Fog at Cabauw*,
4TU Research Data (2018)

- **Bart Schilperoort**, César Jiménez-Rodríguez, *Speulderbos flux, storage, and temperature profile measurements*, 4TU Research Data (2017)